Hellenic Mediterranean University

Polytechnic School

Department of Mechanical Engineering



DEVELOPMENT OF AN AIR COMPRESSION MECHANISM THROUGH HUMAN WALKING FOR INTEGRATION INTO A ROBOTIC MOVEMENT ASSISTANCE SYSTEM

Master Thesis

Student: Konstantinos Thefoanis Prodromidis TM20011

Supervisor: Assoc. Prof. Panagiotis Polygerinos

© 2025

Ελληνικό Μεσογειακό Πανεπιστήμιο

Πολυτεχνική Σχολή

Τμήμα Μηχανολόγων Μηχανικών



ΑΝΑΠΤΥΞΗ ΜΗΧΑΝΙΣΜΟΥ ΣΥΜΠΙΕΣΗΣ ΑΕΡΑ ΜΕΣΩ ΤΟΥ ΑΝΘΡΩΠΙΝΟΥ ΒΑΔΙΣΜΑΤΟΣ ΓΙΑ ΕΝΣΩΜΑΤΩΣΗ ΣΕ ΡΟΜΠΟΤΙΚΟ ΣΥΣΤΗΜΑ ΥΠΟΒΟΗΘΗΣΗΣ ΚΙΝΗΣΗΣ

Διπλωματική Εργασία

Φοιτητής: Κωνσταντίνος Θεοφάνης Προδρομίδης ΤΜ20011

Επιβλέπων: Αναπληρωτής Καθηγητής Παναγιώτης Πολυγερινός

© 2025

Ευχαριστίες

Σε αυτό το σημείο, θα ήθελα να εκφράσω τις βαθύτατες ευχαριστίες μου στον επιβλέποντά μου, Αναπληρωτή Καθηγητή Παναγιώτη Πολυγερινό, για την πολύτιμη καθοδήγηση, την αμέριστη υποστήριξη και την ουσιαστική του καθοδήγηση καθ' όλη τη διάρκεια της εκπόνησης της παρούσας εργασίας. Ιδιαίτερες ευχαριστίες οφείλω επίσης στον επιβλέπων ερευνητή Νικόλα Χαραλάμπους, για την καθοριστική του συμβολή τόσο στο θεωρητικό υπόβαθρο όσο και στην πρακτική υλοποίηση του έργου. Η τεχνογνωσία, η υπομονή και η ενθάρρυνσή τους υπήρξαν καθοριστικής σημασίας για την αντιμετώπιση των προκλήσεων και τη διαμόρφωση της τελικής κατεύθυνσης της εργασίας.

Θα ήθελα επίσης να ευχαριστήσω θερμά την ερευνητική εταιρεία BENDABL για την παραχώρηση του απαραίτητου εξοπλισμού, το δημιουργικό περιβάλλον και το χρόνο που μου προσέφεραν.

Επιπλέον, θέλω να εκφράσω την ειλικρινή μου ευγνωμοσύνη στην οικογένειά μου και στους οικείους μου, για την αμέριστη στήριξη, την υπομονή και την κατανόηση που επέδειξαν καθ' όλη τη διάρκεια των σπουδών μου.

Τέλος, θα ήθελα να αναγνωρίσω τη χρήση εργαλείων τεχνητής νοημοσύνης (generative AI), ως βοηθού κατά την προετοιμασία της παρούσας διπλωματικής εργασίας. Αυτά τα εργαλεία χρησιμοποιήθηκαν για εργασίες όπως η βελτίωση της αφηγηματικής δομής, η ενίσχυση της σαφήνειας του γραπτού λόγου και η δημιουργία εννοιολογικών σχημάτων για επεξηγηματικούς σκοπούς. Είναι σημαντικό να διευκρινιστεί ότι τα εργαλεία αυτά δεν χρησιμοποιήθηκαν για την εννοιολογική ανάπτυξη, τη φυσική κατασκευή, την πειραματική ανάλυση ή τον πυρήνα του μηχανολογικού σχεδιασμού του ίδιου του έργου. Όλες οι τεχνικές συνεισφορές, τα πειραματικά αποτελέσματα και τα συμπεράσματα που παρουσιάζονται σε αυτή την εργασία είναι εξ ολοκλήρου δικά μου.

Περίληψη

Με στόχο την ενίσχυση της αυτονομίας των φορετών πνευματικών μηχανοτρονικών συστημάτων, τα οποία συχνά περιορίζονται από ενσύρματες, ογκώδεις πηγές ισχύος, η παρούσα διπλωματική εργασία παρουσιάζει ένα αυτόνομο σύστημα που συλλέγει πνευματική ενέργεια απευθείας από το ανθρώπινο βάδισμα. Η εργασία περιγράφει λεπτομερώς τον σχεδιασμό, την κατασκευή και την αξιολόγηση μιας καινοτόμου, φορετής πηγής ενέργειας που αποσκοπεί στην υποβοήθηση της τροφοδότηση της επόμενης γενιάς αυτόνομων συστημάτων Soft Robotics.

Ο πυρήνας του συστήματος αποτελείται απο δύο κομμάτια, έναν συμπιεστή αντίθετων διαφραγμάτων, ο οποίος αποτελείται από έναν μαλακό, θερμοσυγκολλημένο υφασμάτινο θύλακα σε συνδυασμό με έναν εξωτερικό υβριδικό μηχανισμό ελατηρίου. Μια κεντρική ανακάλυψη αυτής της εργασίας είναι ο καθοριστικός ρόλος του **λόγου νερκού όγκου (clearance ratio)**—το ποσοστό του 'νεκρού όγκου' που παραμένει στον συμπιεστή μετά από μια πλήρη διαδρομή—ο οποίος περιορίζει θεμελιωδώς τη μέγιστη εφικτή πίεση. Η αρχιτεκτονική των δύο κομματίων, η οποία προέκυψε από μια επαναληπτική διαδικασία πρωτοτυποποίησης, σχεδιάστηκε ειδικά για να μεγιστοποιήσει την ογκομετρική απόδοση ελαχιστοποιώντας αυτή την παράμετρο. Οι συλλέκτες πνευματικής ενέργειας, τοποθετημένοι στα παπούτσια, είναι ενσωματωμένοι με μια ειδικά κατασκευασμένη, ηλεκτροπνευματική μονάδα ελέγχου.

Η πειραματική επικύρωση που πραγματοποιήθηκε σε πραγματικές συνθήκες με ανθρώπινο βηματισμό ταχύτητας 3 km/h απέδειξε τη λειτουργικότητα του συστήματος, επιτυγχάνοντας μέγιστη μετρούμενη πίεση 0.524 atm. Η απόδοση αυτή αποδόθηκε άμεσα σε έναν υψηλό, πειραματικά μετρημένο λόγο νεκρού όγκου 23.4%. Για την ποσοτικοποίηση του μελλοντικού δυναμικού της αρχιτεκτονικής, προσομοιώθηκε ένας θεωρητικά ιδανικός θύλακας με λόγο νεκρού όγκου 1% χρησιμοποιώντας ένα ειδικό αναλυτικό μοντέλο, προβλέποντας εφικτή πίεση 7.27 bar. Συνεπώς, η εργασία αυτή θεμελιώνει μια βιώσιμη αρχιτεκτονική για αυτόνομη πνευματική ισχύ και παρέχει έναν σαφή, βασισμένο στα δεδομένα, οδικό χάρτη για τη μελλοντική της βελτιστοποίηση, στοχεύοντας στον λόγο νεκρού όγκου.

Η παρούσα εργασία υποστηρίχθηκε από την Ευρωπαϊκή Ένωση μέσω του έργου SWAG, με αριθμό επιχορήγησης 101120408.

Λέξεις-κλειδιά: Μαλακή Ρομποτική, Ρομποτική Φορετών Συσκευών, Ενεργειακή Συγκομιδή, Πνευματικά Συστήματα, Opposing Diaphragm Compressor, Ανθρώπινο Βάδισμα

Acknowledgements

I would like to express my deepest gratitude to my supervisor, Assoc. Prof. Panagiotis Polygerinos, for his invaluable guidance and support throughout this research. I also owe my sincere thanks to my supervising researcher Nikolas Charalampous, for his pivotal contributions across both the theoretical and practical aspects of this work. Their combined expertise and encouragement were instrumental in navigating the challenges of this project and shaping its direction.

I would also like to extend my thanks to the entire BENDABL research company for providing access to essential equipment and for providing a collaborative and inspiring environment throughout this journey.

I am also deeply grateful to my family and friends for their endless patience, understanding, and encouragement, which provided a strong foundation for all my academic pursuits.

Finally, I would like to acknowledge the use of generative AI tools, as an assistant in the preparation of this thesis. These tools were employed for tasks such as refining the narrative structure, improving the clarity of English prose, and generating conceptual figures for illustrative purposes. It is important to state that these tools were not used for the conceptual development, the physical fabrication, the experimental analysis, or the core engineering design of the project itself. All technical contributions, experimental results, and conclusions presented in this thesis are entirely my own.

Abstract

To amplify the autonomy of wearable pneumatic mechatronic systems, which are often hindered by tethered, bulky power sources, this thesis presents a self-contained system that harvests pneumatic energy directly from human walking. The work details the design, fabrication, and evaluation of a novel, wearable power source aimed at enabling the next generation of untethered soft robotics.

The core of the system is a de-coupled opposing diaphragm compressor, consisting of a soft, heat-sealed textile pouch paired with an external hybrid spring mechanism. A key finding of this work is the critical role of the **clearance ratio**—the percentage of 'dead volume' that remains in the compressor after a full stroke—which fundamentally limits the maximum achievable pressure. The de-coupled architecture, which emerged from an iterative prototyping process, was specifically engineered to maximize volumetric efficiency by minimizing this parameter. The bilateral, shoe-mounted harvesters are integrated with a custom-built, belt-mounted electropneumatic control unit that manages and regulates the harvested air.

Experimental validation with a human subject walking at 3 km/h demonstrated the system's functionality, achieving a maximum measured gauge pressure of 0.524 atm. This performance was directly attributed to a high, experimentally measured clearance ratio of 23.4%. To quantify the architecture's future potential, a theoretically ideal pouch with a 1% clearance ratio was simulated using a custom analytical model, predicting an achievable pressure of 7.27 bar. This work therefore establishes a viable architecture for untethered pneumatic power and provides a clear, data-driven roadmap for its future optimization by targeting the clearance ratio.

The work was supported by the European Union through the SWAG Project under Grant 101120408.

Keywords: Soft Robotics, Wearable Robotics, Energy Harvesting, Pneumatic Systems, Opposing Diaphragm Compressor, Human Gait

Contents

Ευχαριστίες **iii**

Περίληψη **iv**

Acknowledgements **v**

Abstract **vi**

List of Figures **ix**

List of Tables **xv**

Abbreviations xvi

1 Introduction: The Challenge of Powering Wearable Soft Robotics **1**

1.1 The Promise and Problem of Wearable Robotics 1

1.2 Energy Harvesting as a Pathway to Autonomy 1

1.3 State-of-the-Art and Identified Research Gap 2

1.4 Structure of the Thesis 4

2 Biomechanical Foundations of Human Gait **5**

2.1 Gait Cycle Phases and Force Distribution 5

2.2 Plantar Loading and Footstrike Analysis 7

2.3 Data-Driven Force and Power Profiles 7

2.4 Quantitative Analysis of Biomechanical Metrics 8

2.5 Harvestable Energy Potential 10

3 Analytical Modeling of the Pneumatic System **11**

3.1 Introduction 11

3.2 Conceptual Framework: The Opposing Diaphragm Compressor Cycle 11

3.3 Mechanical and Geometric Design Principles 14

3.4 Derivation of the Dynamic Mass Flow Model 15

3.5 The Theoretical Characteristic Curve 16

4 An Empirical Journey to a Viable Compressor Design 18
4.1 The Initial Design Challenge: Reconciling Competing Goals 18
4.2 A Strategy of Iterative Prototyping and Learning 18
4.3 Iterative Prototype Development and Analysis 19
4.4 Synthesizing the Lessons Learned 25
4.5 Strategic Re-evaluation of Design Objectives 27
4.6 The Convergent Design: A Concept Born from Constraints 27

5 System Architecture, Design, and Fabrication 31
5.1 Overall System Architecture 31
5.2 The Mechanopneumatic Subsystem: Energy Harvester 32
5.3 The Electropneumatic Control Subsystem 37
5.4 Final Assembled Prototype 46

6 Experimental Validation and Performance Characterization 47
6.1 Experimental Setup and Protocols 47
6.2 Instrumentation and Sensor Calibration 47
6.3 Component-Level Characterization 49
6.4 Integrated System Performance Validation 52
6.5 Synthesis and Discussion 59
6.6 Data-Driven Performance Analysis and Summary 59

7 Conclusion and Future Work 62
7.1 Summary of Work and Key Findings 62
7.2 Answering the Guiding Research Questions 62
7.3 Limitations 63
7.4 Future Work 64

Bibliography 67

Appendix A: Source and Configuration 70
PlatformIO Configuration (platformio.ini) 70
Shared Header File (Shared.h) 71
Main Firmware (main.cpp) 71

Appendix B: Key CAD Designs 79
Iterative Prototype Designs (Chapter 4) 79
Final Convergent Design (Chapter 5) 85

List of Figures

1.1 Comparison of energy conversion pathways for powering pneumatic soft actuators. **The Indirect Electrical Pathway (left)** involves multiple conversion stages: mechanical energy from gait is first converted to electricity, stored chemically in a battery, then used to power a motor, which finally generates pneumatic power. **The Direct Pneumatic Pathway (right)**, pursued in this work, captures mechanical energy and converts it directly into stored pneumatic energy, minimizing conversion losses and system complexity. 2

2.1 Phases of the human gait cycle, illustrating the temporal distribution of stance and swing phases and their respective sub-phases. Image adapted from well-established biomechanical literature[11] 5

2.2 Mean normalized Vertical Ground Reaction Force (VGRF) curve with one standard deviation shaded, calculated from 16,090 trials. 8

2.3 Mean Anterior-Posterior (AP) Power curve with one standard deviation shaded. The negative power (braking) phase represents the primary window for energy harvesting. 8

3.1 A notional Pressure-Volume (P-V) diagram for an idealized single-acting compressor. The cycle consists of four processes: compression (A→B), isobaric delivery (B→C), expansion (C→D), and isobaric induction (D→A). The area enclosed by the curve represents the net work done on the gas per cycle. 12

3.2 Mapping of the thermodynamic compressor cycle onto the phases of human gait. The cycle is driven by the user's natural motion: **Initial Contact** initiates the Compression stroke. As the body's weight is fully accepted during **Opposite Toe Off**, the Delivery stroke expels high-pressure air. At **Toe Off**, the foot lifts, allowing the rebound mechanism to begin the Expansion and subsequent Intake strokes, which continue throughout the swing phase, preparing the pump for the next cycle. 14

3.3 A simplified free-body diagram illustrating the force balance required for compression. The user-applied foot force must be greater than the sum of the mechanical spring's restoring force and the force from the internal gas pressure. This highlights the two primary sources of resistance the user must overcome during the stance phase. 15
3.4 Qualitative representation of the theoretical mass flow characteristic curve, derived from the analytical model (Equation 3.5). This plot illustrates the core hypothesis of the system: the mass of air added per compression cycle is a linear function of the reservoir's back-pressure. Mass flow is highest when the reservoir is at atmospheric pressure and decreases linearly to zero at the theoretical "stall pressure." 17

4.1 The passive mechanofluidic system of the first prototype iteration. Key components shown are (A) the heat-sealed textile pouch with an internal sponge, (B) the pneumatic manifold assembly, and (C) the fully integrated device. 19
4.2 Conceptual cross-section of the fabrication for the passive pump (Iteration 1). An open-cell sponge (B) is sandwiched between two layers of TPU-coated fabric (A and C) and sealed by heated platens (D). This simple approach failed as the sponge's restoring force was too slow for a viable intake stroke. 20
4.3 CAD models illustrating the empirical design evolution of the internal TPU rebound springs (Iteration 2). Five distinct spring geometries (A-E) were developed to find a structure that could collapse to a minimal height while providing sufficient restorative force. 20
4.4 Physical prototype of the internal spring concept (Iteration 2). (a) The completed pouch shows the impractical, upward-facing push-fit fitting (A). (b) The internal view reveals the complexity: a non-stick paper mask (C) defines the cavity for the spring, while glued-in tube segments (B) were required to create a functional airway and prevent collapse during intake. These ad-hoc fixes highlighted the design's impracticality. 21
4.5 Illustration of the manufacturing challenges in the internal spring design (Iteration 2). The concept required sealing a 3D-printed TPU spring (B) between two layers of TPU-coated fabric (C), using non-stick paper (A) to define the unsealed chamber. The primary difficulty was that the assembly could not be sealed in a single press. Instead, it required a painstaking process of tracing the perimeter of the internal spring with the heat press (D) in multiple steps. This method was unreliable, often resulted in inconsistent seals, and could lead to an unintentionally large clearance volume (V_{cl}), defeating the purpose of the design. 22
4.6 Exploded view of the layered assembly for the structured pouch concept (Iteration 3), showing the TPU fabric layers (A, F), non-stick masks (B, E), 3D-printed TPU frame (C), and wooden jig (D). 23

4.7 Detailed views of the individual components of the structured pouch concept (Iteration 3). The design's complexity is evident in its numerous specialized features: (A) an exploded view of the layered assembly. (B) The non-stick mask defines both the main compression chamber and the push-fit fitting hole. (C) The wooden jig was designed with a split for easier removal after heat-sealing. (D) The 3D-printed frame featured a hexagonal recess for a captive nut to secure the fitting. (E) A cross-section of the frame reveals the integrated air channel designed to route air from the compression chamber to the outlet. (F) The frame's raised wall was intended to give the pouch its third dimension. This high level of complexity ultimately contributed to the design's failure due to sealing issues at the material interfaces. 24
4.8 Cross-section of the structured pouch concept (Iteration 3) during fabrication. The design aimed to create a monolithic bond (F) between the TPU-coated fabric (B) and a 3D-printed TPU frame (E). The design failed due to the inherent micro-porosity of the FDM-printed frame (E), which prevented a reliable high-pressure seal. . . . 25
4.9 Evolution of the pouch fabrication method to solve the pneumatic fitting orientation problem. (a) The initial concept utilized two separate fabric pieces. (b) This method resulted in a vertical fitting unsuitable for bearing load. (c) The revised method uses a single, symmetrical, laser-cut fabric pattern. (d) When folded, this one-piece design naturally reorients the fitting into a robust and low-profile horizontal position. 29
4.10 Fabrication schematic of the final, convergent pouch design. A single piece of TPU-coated fabric (A) is folded (C), and a parchment paper mask (B) is placed inside before being sealed by the heat press (D). This simple approach eliminates all previously identified failure modes and maximizes potential volumetric efficiency. 30

5.1 High-level architecture of the integrated pressure harvesting system, illustrating the relationship between the mechanopneumatic and electronic control subsystems and the flow of force, air, and data. 31
5.2 Different views of the final fabricated textile pouch. (A) The initial untrimmed shape was based on the projected heel contact area. (B) This was then manually trimmed for an optimal fit inside a standard shoe. (C) The side view and (D) front view highlight the integrated mounting flaps, which were created by fusing additional fabric strips into loops to create robust anchor points for the rebound mechanism. 33
5.3 Exploded view of the hybrid rebound mechanism. The assembly consists of: (A) two high-force metal torsion springs; (B) a 3D-printed TPU housing; (C) two M3 bolts for clamping; and (D, E) two M5 bolts and corresponding nuts that serve as axles for the springs. 34

5.4 The fully assembled mechanopneumatic compressor unit. (A) The front view shows the textile pouch integrated with the rebound mechanism. (B) The bottom view reveals the torsion springs providing the restorative force. (C) The side view shows the profile of the complete unit. (D) The assembly is shown placed within the heel of a shoe to illustrate its scale and intended fit. (E) This detail highlights the ”sandwich clamp” method, where the M3 bolts securely anchor the pouch’s fabric mounting flaps. 35
5.5 The custom 3D-printed case for the 500ml PET bottle reservoir, featuring integrated belt loops for wearability and the university logo. 36
5.6 Pinout mapping for the Arduino Nano, detailing the specific function of each pin utilized in the control system. 38
5.7 The two types of pressure sensors utilized in the control system. 39
5.8 Flowchart illustrating the Leader/Follower control logic. Both controllers run an independent ”Read-Decide-Act” loop for their pneumatics. The Leader periodically requests data from the Follower via an I2C interrupt to update the central display. . 40
5.9 The salvaged SMC ITV0010 manifold, which integrates the two 24V solenoid valves and the pump pressure sensor into a single block. A custom 3D-printed cap was added to enclose exposed components. 41
5.10 High-level pneumatic schematic of the control system for a single foot. The Arduino Nano functions as the control box, reading analog signals from the Tank and Pump pressure sensors and actuating the two 2/2 solenoid valves to manage airflow. 42
5.11 The complete electrical schematic for the bilateral control system. The diagram shows the Leader/Follower architecture, with two Arduino Nanos, independent power converters, and MOSFET valve drivers, all communicating via an I2C bus with a signal extender. 43
5.12 The initial V1 perfboard prototype for the Slave (Left Foot) controller, showing the Arduino Nano and two MOSFET modules. 43
5.13 CAD model showing the integration of the V1 perfboard and the valve manifold into the first-generation control box design. 44
5.14 The final, more compact V2 perfboard for the Leader (Right Foot) controller, integrating the Arduino Nano, DC-DC step-up converters, and MOSFETs. 44
5.15 The fully assembled Leader (Right Foot) control box, housing all electronic and pneumatic management components. 45
5.16 The user interface display, showing real-time performance metrics including individual pump pressures, tank pressure, runtime, step count, and steps per minute (SPM). 45

5.17 The fully integrated, bilateral pressure harvesting system, showing the shoe-mounted mechanopneumatic units and the belt-mounted electropneumatic control and storage unit. 46

6.1 Comprehensive calibration curves for all four pressure sensors used in the bilateral system. The plot shows the raw ADC output as a function of the applied pressure in psi for the positive pressure range (≥ 0 psi). Each data series is fitted with a linear regression model, calculated from the full dataset including negative pressures, with the resulting equations and statistical parameters displayed in the top-left inset. The shaded regions represent the standard deviation (σ) for each linear model, indicating the band that contains approximately 68% of the data points. The magnified detail view highlights the close agreement between the raw data points and the linear fits. The specific linear models derived are: **Left Foot Pump:** $y = 6.0562x + 188.20$ ($R^2 = 0.9991$) **Right Foot Pump:** $y = 9.8774x + 171.03$ ($R^2 = 0.9994$) **Right Foot Tank:** $y = 5.6447x + 184.03$ ($R^2 = 0.9994$) **Left Foot Tank:** $y = 9.9562x + 167.71$ ($R^2 = 0.9991$) The inverse of each of these unique equations was implemented in the control software and scaled to convert raw ADC values directly into pressure readings in standard atmospheres (atm). 48

6.2 Experimentally measured force-displacement profile of the hybrid rebound mechanism. The data, obtained from a Universal Testing Machine, plots the resistive load (N) as a function of compression distance (mm). The response is observed to be largely linear with a slight, progressive stiffening at higher displacements. The effective linear stiffness (k_{eff}) is derived from the slope of the central operating region to provide a representative metric for the mechanism's stiffness, which is a critical parameter for both the system's dynamic performance and the energy input required from the user. 50

6.3 Experimental setup for the volumetric analysis via fluid displacement. (a) The scale measures the mass of water expelled in a single stroke (4.77 g), representing the swept volume. (b) The scale measures the total mass of water after the remaining contents are also expelled (6.23 g), representing the maximum pouch volume. . . . 51

6.4 The pressure harvesting system worn by a human subject during the treadmill walking test. 53

6.5 The experimental setup for the analytical model validation. (a) The modified 10 mL syringe is connected to the electropneumatic control box. The labels indicate the two components of the clearance volume (V_{cl}) that were modeled: the internal volume of the syringe tip and the volume of the connecting tube. (b) A close-up of the syringe, showing a mechanical hard stop to ensure a consistent 10 mL swept volume for each pump stroke, thereby increasing experimental repeatability. 54

6.6 Determination of the syringe's internal clearance volume. The complex geometry of the syringe tip was modeled in CAD to accurately calculate the residual air volume when the plunger is fully depressed. 55
6.7 Direct comparison of the analytical model's prediction against the experimental results for the 100-stroke syringe test. (a) The simulation predicted a final gauge pressure of 1.46 bar. (b) The experimental test recorded a peak gauge pressure of approximately 1.42 atm (1.44 bar). The strong correlation in both the final pressure values (1.4% difference) which validates the predictive accuracy of the event-based analytical model. 56
6.8 Direct comparison of the analytical model's prediction against the real-world experimental results for a 600-step test. While the general charging behavior is similar, a significant discrepancy in the final achieved pressure is evident. 58

7.1 Simulated performance of a theoretically ideal pouch with a 100:1 compression ratio (1% clearance). The model predicts that the system can achieve 7.27 bar in 600 steps, a value that approaches the static pressure limit of the final pouch geometry. 65

1 Technical drawing of the pouch assembly pattern for the Iteration 2 prototype. . . . 79
2 Technical drawing of the internal spring concept, variant 1. 80
3 Technical drawing of the internal spring concept, variant 2. 80
4 Technical drawing of the internal spring concept, variant 3. 81
5 Technical drawing of the pouch pattern for the Iteration 3 prototype. 82
6 Technical drawing of the TPU Fabric for Iteration 3. 83
7 Technical drawing of the wooden jig used for fabrication in Iteration 3. 83
8 Technical drawing of the 3D-printed TPU structural frame for Iteration 3. 84
9 Technical drawing of the one-piece folded pattern for the final compressor pouch. . 85
10 Technical drawing of the 3D-printed TPU housing for the de-coupled hybrid spring mechanism. 86
11 Technical drawing of the complete electropneumatic control box assembly. 87
12 Technical drawing of the 3D-printed case for the PET bottle reservoir. 87
13 Technical drawing of the enclosure for the OLED display module. 88

List of Tables

1.1 Initial project Key Performance Indicators (KPIs). 4

2.1 Descriptive statistics of key biomechanical metrics across all valid trials (N = 16,090). 9

4.1 Summary of Critical Lessons from the Prototyping Gauntlet. 26

6.1 Comparison of Theoretical (Estimated) and Measured (Fluid Displacement) Volumetric Parameters. 52

6.2 Final comparison of project goals and experimental results. 59

Abbreviations

ADC Analog-to-Digital Converter

AP Anterior-Posterior

CAD Computer-Aided Design

FDM Fused Deposition Modeling

I2C Inter-Integrated Circuit

KPI Key Performance Indicator

MOSFET Metal-Oxide-Semiconductor Field-Effect Transistor

OLED Organic Light-Emitting Diode

P-V Pressure-Volume

PCB Printed Circuit Board

SLPM Standard Liters Per Minute

TPU Thermoplastic Polyurethane

UTM Universal Testing Machine

VGRF Vertical Ground Reaction Force

1. Introduction: The Challenge of Powering Wearable Soft Robotics

1.1 The Promise and Problem of Wearable Robotics

Soft robotics is a transformative field that leverages compliant, deformable materials to build systems capable of safe, adaptive interaction with humans and unstructured environments [1]. This paradigm shift away from traditional rigid robotics has unlocked a wide spectrum of applications, most notably the development of *wearable robotic devices*—soft exosuits, assistive sleeves, and smart garments designed to augment human movement, restore mobility, or provide physical support [2]–[4].

However, the practical deployment of these promising technologies outside of laboratory environments is constrained by a single, fundamental challenge: **energy autonomy**. Because many soft actuators are powered by **pressurized air** to achieve their life-like, compliant motion, they depend on continuous pressure sources, which typically means being tethered to bulky benchtop compressors or carrying heavy, finite-capacity air tanks. This reliance on external power severely limits user mobility, creating a critical bottleneck that hinders the translation of wearable soft robotics from research to real-world impact.

1.2 Energy Harvesting as a Pathway to Autonomy

Energy harvesting from human motion presents a compelling solution to this challenge [5]. While electricity is arguably a more versatile energy carrier, the specific context of powering pneumatic soft robots makes a **direct mechanical-to-pneumatic** conversion pathway uniquely advantageous. This approach offers benefits beyond just conversion efficiency, including:

- **System Simplicity and Robustness:** A direct pneumatic source eliminates the need for a separate electric motor, a miniature pump, and the associated motor control electronics. This reduction in components decreases the overall system weight, complexity, and potential points of failure [6].
- **Silent Operation:** The passive nature of the compression avoids the characteristic acoustic noise generated by miniature electric compressors, a critical factor for user acceptance and unobtrusiveness in wearable devices.

- **Direct Compatibility:** The system's output is already in the form of pressurized air, the native energy modality for the target soft robotic actuators, creating a more elegant and seamlessly integrated system.

As illustrated in Figure 1.1, this direct pathway avoids the compounding efficiency losses inherent in multi-stage electrical conversion pathways (e.g., mechanical → electrical → chemical → pneumatic) [7], [8], which further strengthens the argument for its selection in this application.

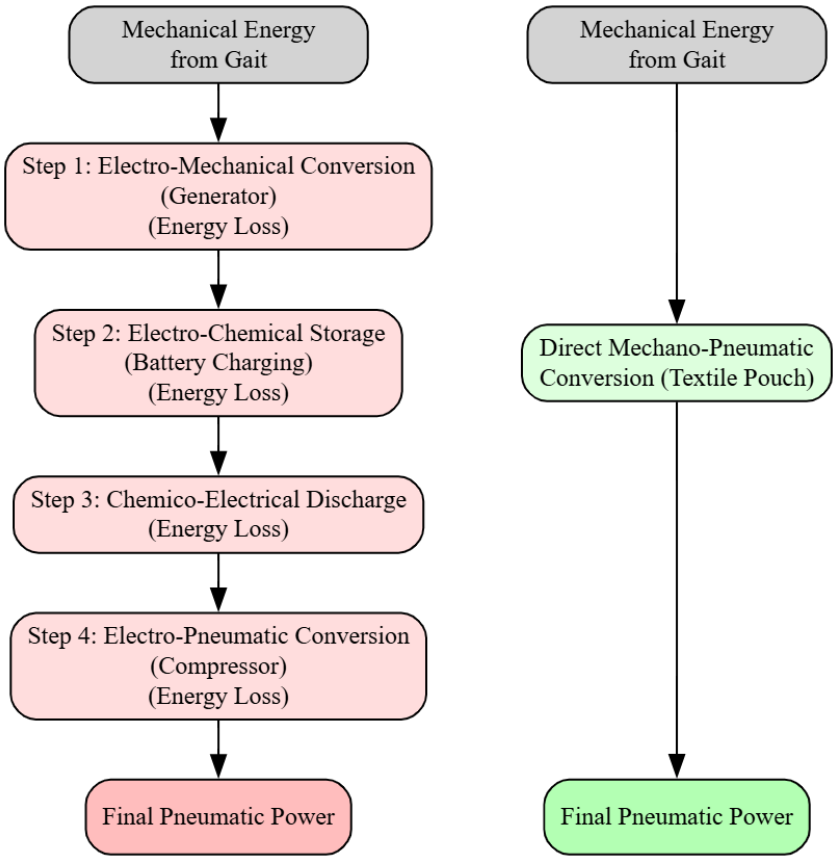


Figure 1.1: Comparison of energy conversion pathways for powering pneumatic soft actuators. **The Indirect Electrical Pathway (left)** involves multiple conversion stages: mechanical energy from gait is first converted to electricity, stored chemically in a battery, then used to power a motor, which finally generates pneumatic power. **The Direct Pneumatic Pathway (right)**, pursued in this work, captures mechanical energy and converts it directly into stored pneumatic energy, minimizing conversion losses and system complexity.

1.3 State-of-the-Art and Identified Research Gap

The concept of harvesting energy from human locomotion is well-established [5]. For the specific goal of powering pneumatic soft actuators, the most relevant benchmark was presented by Shveda et al. [9], who developed a system based on a soft bladder with an internal foam

structure for rebound. Their work demonstrated the feasibility of the approach and provided a high-fidelity numerical model to predict performance.

However, a significant research gap remains. The use of internal rebound mechanisms, like foams, can reduce the volumetric compression ratio, limiting the achievable output pressure. This thesis addresses this specific gap by investigating a novel, **de-coupled hardware architecture** designed to solve the rebound challenge without compromising volumetric efficiency. The core contribution is the systematic, empirical process of identifying the limitations of integrated designs (Chapter 4) and developing a new architecture—an empty textile pouch paired with an external hybrid spring—to overcome them (Chapter 5). To support this hardware-centric approach, a transparent, event-based analytical model is developed (Chapter 3), providing a clear, first-principles benchmark for the system's performance.

Thesis Objectives and Guiding Questions

The development of this system was guided by a primary objective, which was broken down into a series of guiding research questions that this thesis seeks to answer:

Primary Objective: To design, fabricate, and evaluate a wearable, gait-powered system capable of generating and regulating high-pressure air for soft robotic applications.

Guiding Questions:

1. What are the theoretical limits and practical trade-offs governing the design of a low-profile, textile-based pneumatic compressor?
2. What fabrication techniques and design architectures can overcome the challenges of creating a durable, high-pressure seal in a soft, flexible device?
3. Can an external, hybrid spring mechanism provide the necessary rebound force for rapid intake without compromising the compressor's volumetric efficiency?
4. Can a complete, bilateral system be integrated with a custom electropneumatic controller to deliver a stable, regulated pressure output?
5. What is the real-world performance of the final system in terms of pressure generation, flow rate, and power, and how does it compare to theoretical models?

Key Performance Indicators (KPIs)

To provide a clear, quantitative benchmark for success, a set of ambitious Key Performance Indicators (KPIs) was established at the outset of the project, grounded in the demonstrated performance of state-of-the-art systems.

The primary benchmark for this work is the wearable pneumatic harvester developed by Shveda et al. [9]. Their system demonstrated the ability to achieve a maximum pressure in the range of 1.0 to 1.2 bar during walking tests. Based on this, the target for the maximum gauge pressure for this thesis was set at **1.2 bar**.

To establish a credible KPI for the air supply rate, a detailed analysis of the survey by Wehner et al. [10] was conducted. This work established that a state-of-the-art untethered system requires an average flow rate of approximately 7.2 SLPM. The goal of this thesis, however, is not to entirely replace a primary power source, but rather to develop a supplementary harvesting system capable of offloading approximately **10%** of the energy burden. For a bilateral (two-foot) system, this implies a per-sole requirement of 3.6 SLPM to meet the benchmark. A 10% contribution from the harvesting system therefore leads to a refined target air supply rate of approximately **0.36 SLPM** per sole.

The initial KPIs for the system, summarized in Table 1.1, were therefore chosen to validate this supplementary harvesting concept.

Table 1.1: Initial project Key Performance Indicators (KPIs).

Metric	**Initial Target**
Maximum Gauge Pressure	$\geq$ 1.2 bar [9]
Maximum Insole Thickness	$\leq$ 10 mm
Air Supply Rate (per sole)	$\approx$ 0.36 SLPM [10]
Bilateral Operation	Required

1.4 Structure of the Thesis

This thesis is structured to guide the reader through the complete engineering process, from theoretical foundations to experimental validation. **Chapter 2** reviews the biomechanical principles of human gait that enable energy harvesting. **Chapter 3** develops the analytical and thermodynamic models that govern the system's performance and establishes key theoretical benchmarks. **Chapter 4** documents the critical, iterative design journey, detailing the prototype failures that led to a re-evaluation of the initial design goals. **Chapter 5** presents the detailed design and fabrication of the final, convergent prototype, including both its mechanopneumatic and electronic subsystems. **Chapter 6** details the experimental validation of the system, presenting quantitative data on its real-world performance. Finally, **Chapter 7** summarizes the key findings, answers the guiding research questions, and provides recommendations for future research.

2. Biomechanical Foundations of Human Gait

Before commencing any analytical modeling or device development related to human locomotion, it is essential to understand the fundamental principles underlying gait. This chapter is therefore dedicated to highlighting the biomechanical basis of human walking.

Human gait is a complex, rhythmic, and cyclical locomotor pattern resulting from the coordinated integration of neuromuscular control, skeletal biomechanics, and ground reaction forces. According to biomechanical literature, a gait cycle is defined as the sequence of movements occurring between two consecutive initial contacts of the same foot[11], [12].

2.1 Gait Cycle Phases and Force Distribution

The progression of the human gait cycle, as illustrated in Figure 2.1, is traditionally divided into two major phases: the **stance phase**, during which the foot is in contact with the ground, and the **swing phase**, during which the foot is airborne.

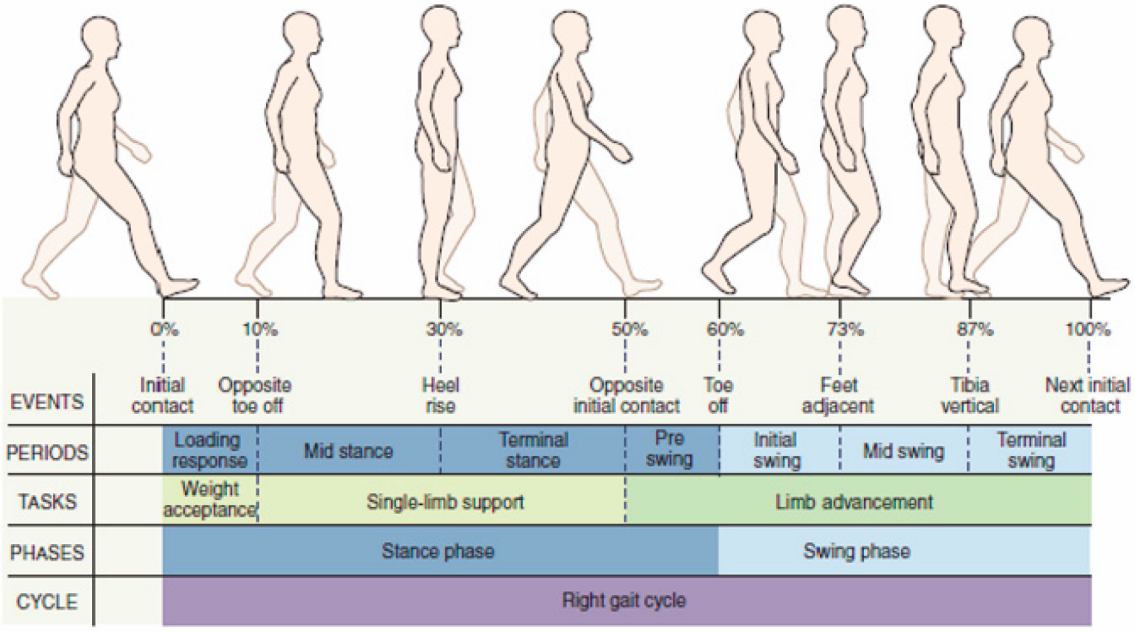


Figure 2.1: Phases of the human gait cycle, illustrating the temporal distribution of stance and swing phases and their respective sub-phases. Image adapted from well-established biomechanical literature[11] .

Stance Phase

The stance phase comprises approximately 60% of the gait cycle and begins with the initial contact of the foot with the ground. It ends when the same foot lifts off the ground to initiate the swing phase [13]. This phase is responsible for supporting body weight, absorbing shock, and propelling the body forward. As detailed in Figure 2.1, it can be further subdivided into five distinct sub-phases:

1. **Initial Contact:** Also referred to as heel strike. The foot first makes contact with the ground, typically at the heel, and ground reaction forces begin to rise rapidly.
2. **Loading Response:** Body weight is transferred onto the stance limb. The quadriceps contract eccentrically to control knee flexion, absorbing impact forces.
3. **Mid-Stance:** The body's center of mass passes over the stationary foot. The plantarflexors control forward progression of the tibia.
4. **Terminal Stance:** The heel rises and the body is propelled forward. Peak ankle plantarflexor moments occur during this sub-phase.
5. **Pre-Swing:** Also known as push-off. The toes are the last to leave the ground, and propulsion is completed via stored elastic energy in the Achilles tendon.

Kinetically, the stance phase is characterized by high vertical ground reaction forces, typically peaking around 1.2 times body weight. Crucially, its kinetic profile reveals a clear functional division. The initial half is dominated by **energy absorption** as the body actively brakes against its forward momentum. In contrast, the latter half is characterized by **energy generation** to propel the body forward. This dichotomy between an energy-dissipating 'braking' phase and an energy-generating 'propulsive' phase is fundamental. Any external device must respect this division to work synergistically, rather than antagonistically, with the user.

Swing Phase

The swing phase makes up the remaining 40% of the gait cycle and begins with toe-off, ending with the next initial contact of the same foot. During this phase, the limb is not in contact with the ground and is instead advanced forward in preparation for the next step. The swing phase is subdivided into:

1. **Initial Swing:** The thigh begins to advance and the knee flexes to aid in foot clearance. Hip flexors and dorsiflexors activate.
2. **Mid-Swing:** The limb continues to swing forward and the foot clears the ground. Ankle dorsiflexion maintains neutral foot position.

3. **Terminal Swing:** The knee extends in preparation for contact, and hamstrings decelerate the limb to prevent hyperextension.

Although the swing phase is less mechanically demanding in terms of external forces, it requires precise neuromuscular coordination to ensure sufficient foot clearance and limb positioning. The muscles primarily operate to maintain posture, control limb inertia, and prepare for subsequent weight acceptance.

2.2 Plantar Loading and Footstrike Analysis

While the entire foot is involved in gait, the distribution of force is not uniform. The analysis begins with **footstrike**, the initial contact that dictates subsequent biomechanical events. In typical healthy gait, this occurs at the **heel**[14]. This heel-strike pattern is functionally significant, positioning the limb to absorb shock and utilize the 'heel rocker' mechanism to smoothly transition the body's center of mass forward. Our analysis of the Gutenberg Gait Database confirms this pattern across over 16,000 trials. Therefore, the heel serves as the primary interface for the initial transfer of both vertical (support) and anterior-posterior (braking) forces, making it a location of primary interest for any device aiming to interact with these forces.

2.3 Data-Driven Force and Power Profiles

To quantify the kinetic profiles of a healthy population, we conducted a comprehensive analysis of the Gutenberg Gait Database [15]. Our analysis of 16,090 valid gait trials provides a quantitative foundation for our work, moving beyond textbook models to a statistical representation of a large population.

Vertical Ground Reaction Force Profile

The mean Vertical Ground Reaction Force (VGRF) across all trials exhibits the classic bimodal ('M-shaped') curve, as shown in Figure 2.2. It peaks first during weight acceptance and again during propulsion, confirming the dual functions of shock absorption and forward thrust.

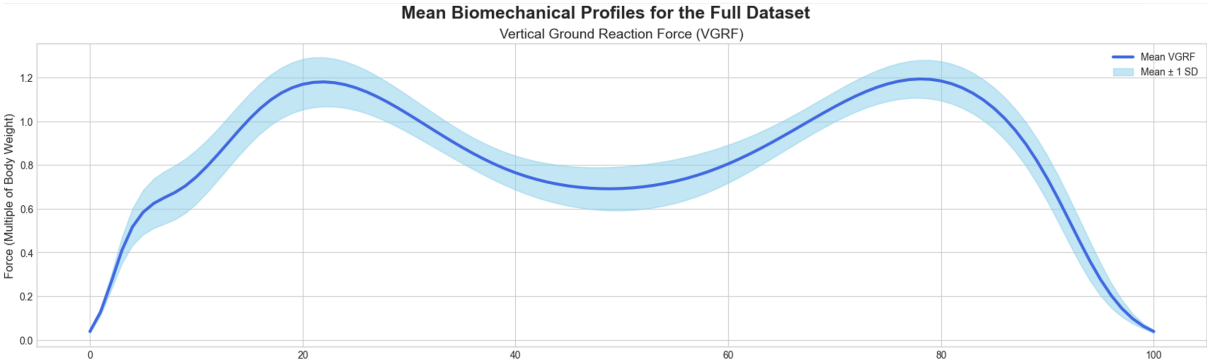


Figure 2.2: Mean normalized Vertical Ground Reaction Force (VGRF) curve with one standard deviation shaded, calculated from 16,090 trials.

Anterior-Posterior Power Profile

More critical to energy exchange is the Anterior-Posterior (AP) power profile. Our analysis revealed that the first 48% of the stance phase is, on average, a **braking phase**, characterized by a period of **negative mechanical power**, as shown in Figure 2.3. This represents the window where the body is actively dissipating energy. The latter 52% of stance is a **propulsive phase**, characterized by positive power and energy generation.

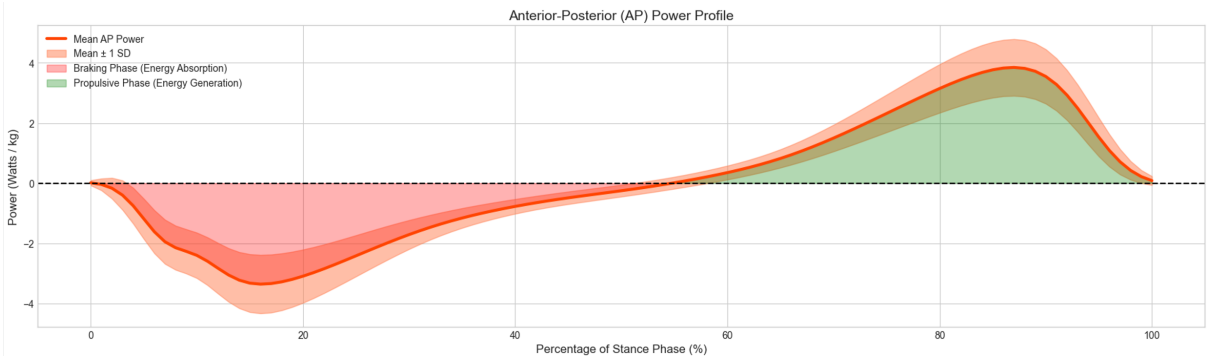


Figure 2.3: Mean Anterior-Posterior (AP) Power curve with one standard deviation shaded. The negative power (braking) phase represents the primary window for energy harvesting.

2.4 Quantitative Analysis of Biomechanical Metrics

To distill the force and power curves into single, interpretable values, several key scalar metrics were derived for each of the 16,090 trials. The following section details the mathematical foundation for each metric, providing the basis for the summary results in Table 2.1.

Vertical Impulse

The vertical impulse (I_v) represents the total supportive effort of the limb over the stance phase. It is calculated as the definite integral of the VGRF curve with respect to time.

$$I_v = \int_{t_{start}}^{t_{end}} \text{VGRF}(t)\, dt \tag{2.1}$$

Peak Loading Rate

The peak vertical loading rate (VLR) quantifies the abruptness of weight acceptance. It is defined as the maximum positive slope of the VGRF curve during the initial 50% of the stance phase.

$$\text{VLR}_{\text{peak}} = \max\left(\frac{d(\text{VGRF})}{dt}\right) \quad \text{for } t \in [0, 0.5 \times t_{\text{stance}}] \tag{2.2}$$

Anterior-Posterior Power and Work

The instantaneous AP power (P_{ap}) is the product of the AP force (F_{ap}) and the walking velocity (v_{walk}).

$$P_{ap}(t) = F_{ap}(t) \cdot v_{walk} \tag{2.3}$$

The total energy transferred is found by integrating this power curve. **Braking Work (W_{braking})** is the integral of the negative portion of the power curve and represents the harvestable energy. **Propulsive Work ($W_{\text{propulsive}}$)** is the integral of the positive portion.

$$W_{\text{braking}} = \int_{t_{start}}^{t_{end}} |P_{ap}(t)|\, dt \quad \text{where } P_{ap}(t) < 0 \tag{2.4}$$

$$W_{\text{propulsive}} = \int_{t_{start}}^{t_{end}} P_{ap}(t)\, dt \quad \text{where } P_{ap}(t) > 0 \tag{2.5}$$

These integrals were solved numerically using Simpson's rule. The resulting descriptive statistics for the entire dataset are presented in Table 2.1.

Table 2.1: Descriptive statistics of key biomechanical metrics across all valid trials (N = 16,090).

Metric	Mean	Std. Dev.	Min	Max
Vertical Impulse (BW·s)	0.335	0.012	0.243	0.431
Peak Loading Rate (BW/point)	0.141	0.023	0.068	0.240
Braking Work (J/kg)	0.338	0.086	0.050	0.704
Propulsive Work (J/kg)	0.344	0.085	0.056	0.640

2.5 Harvestable Energy Potential

The existence of a significant negative power phase in the gait cycle represents a clear opportunity for energy harvesting. The work done during this braking phase—which our analysis quantifies as an average of **0.338 J/kg** per step (Table 2.1)—is typically dissipated as heat within the musculoskeletal system. This represents a reliable source of 'wasted' energy that can be captured[16].

The optimal strategy for an energy harvesting device is to engage during this negative work period. By doing so, the device assists the body in its natural braking function. The heel-strike event provides the ideal trigger, as it marks the simultaneous onset of high vertical forces (for mechanical actuation) and the beginning of the braking power phase (for energy capture). This synergistic alignment forms the central hypothesis for the design of our textile-based **opposing diaphragm compressor**.

3. Analytical Modeling of the Pneumatic System

3.1 Introduction

This chapter establishes the core theoretical framework for the proposed energy harvesting system. The development of a predictive model is essential for understanding system performance, guiding design choices, and establishing a benchmark for experimental validation.

The current state-of-the-art for modeling a similar textile-based pneumatic harvester was presented by Shveda et al. [9]. As detailed in their supplementary materials, their approach is a high-fidelity, **time-stepping numerical simulation**. It solves a dynamic force-balance equation at small time intervals (dt), incorporating experimentally-fitted polynomials for the pouch's volume-compression relationship and a Neo-Hookean model for the internal foam's restoring force. This method is powerful for simulating the detailed, dynamic behavior of their specific device.

In contrast, the model developed in this thesis is an **event-based analytical model**. The primary goal of this approach is not to simulate the instantaneous dynamics, but rather to derive a clear, closed-form equation that predicts the net mass of air delivered to the reservoir per complete gait cycle. By focusing on the state of the system at the beginning and end of each cycle, we can develop a more transparent, first-principles model. This allows for the generation of a theoretical "characteristic curve" that directly relates mass flow to reservoir back-pressure, providing a fundamental and intuitive tool for understanding the system's primary performance trade-offs. This analytical curve will serve as the central hypothesis for the experimental validation conducted in Chapter 6.

3.2 Conceptual Framework: The Opposing Diaphragm Compressor Cycle

The energy harvesting device developed in this thesis is a novel implementation of an **diaphragm compressor**. Traditional diaphragm compressors are positive-displacement machines that use a flexible membrane to alter the volume of a chamber, providing oil-free, hermetic compression that is ideal for handling pure or hazardous gases [17]. They are typically actuated mechanically or hydraulically and constructed from metal and high-performance elastomers.

The compressor in this work is non-traditional in two key ways. First, its diaphragm is not a single membrane but is formed from two flexible, TPU-coated textile layers that move in opposition, classifying it more specifically as an **opposing diaphragm compressor**. Second, its actuation is not provided by a motor, but is driven directly by the biomechanical forces of human gait.

Despite these significant differences in material and actuation, the underlying thermodynamic process of gas compression remains identical. Therefore, the operation of this wearable pump is best understood by analyzing its complete thermodynamic cycle on an idealized Pressure-Volume (P-V) diagram, as shown in Figure 3.1.

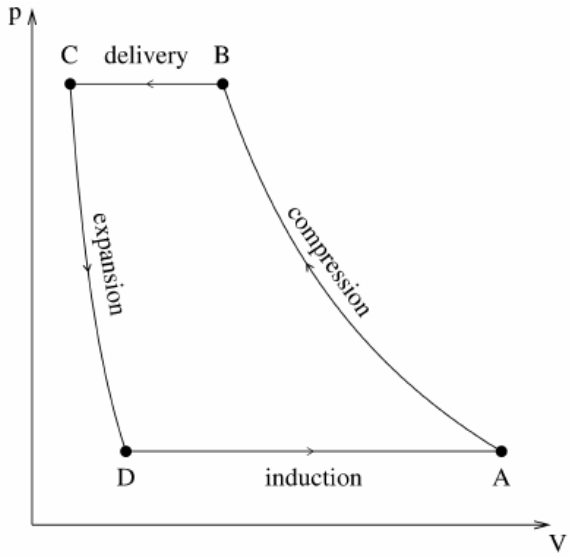


Figure 3.1: A notional Pressure-Volume (P-V) diagram for an idealized single-acting compressor. The cycle consists of four processes: compression (A→B), isobaric delivery (B→C), expansion (C→D), and isobaric induction (D→A). The area enclosed by the curve represents the net work done on the gas per cycle.

The complete cycle, which describes the state of the gas within the compressor, can be subdivided into four distinct thermodynamic processes:

1. **Compression (Process A → B):** The cycle is initiated as the user's foot strikes the device. With both valves closed, the volume of the chamber is decreased from its maximum (V_A) to V_B. The work done on the gas causes its pressure to rise from atmospheric pressure ($P_A = P_{atm}$) to the delivery pressure (P_B).

2. **Delivery (Process B → C):** As the user's weight is fully applied, the output valve opens. As the compressor's volume continues to decrease from V_B to its minimum or "clearance" volume (V_C), the high-pressure gas is expelled into the reservoir at a constant delivery pressure.

3. **Expansion (Process C $\rightarrow$ D):** As the user's foot lifts off during the swing phase, both valves close. The rebound mechanism immediately begins to drive the pouch open, increasing the chamber volume. This causes the small amount of high-pressure air trapped in the clearance volume (V_C) to re-expand, and the internal pressure drops rapidly from the delivery pressure.

4. **Induction (Process D $\rightarrow$ A):** The rebound mechanism continues to pull the pouch open. Once the internal pressure drops slightly below atmospheric pressure, the intake valve opens. The remainder of the rebound stroke then draws a fresh charge of ambient air into the chamber at a constant atmospheric pressure (P_{atm}) until the pouch reaches its maximum volume (V_A). The system is now reset and ready for the next compression stroke.

As established in the biomechanical analysis of Chapter 2, the stance phase of gait is characterized by high ground reaction forces and a period of negative work where the body dissipates energy. This provides the ideal mechanical input to drive the thermodynamic cycle. The high forces are sufficient to perform the Compression and Delivery strokes, while the subsequent lifting of the foot during the swing phase allows for the Expansion and Intake strokes. Figure 3.2 provides a direct mapping of these thermodynamic processes onto the key events of the human gait cycle.



Figure 3.2: Mapping of the thermodynamic compressor cycle onto the phases of human gait. The cycle is driven by the user's natural motion: **Initial Contact** initiates the Compression stroke. As the body's weight is fully accepted during **Opposite Toe Off**, the Delivery stroke expels high-pressure air. At **Toe Off**, the foot lifts, allowing the rebound mechanism to begin the Expansion and subsequent Intake strokes, which continue throughout the swing phase, preparing the pump for the next cycle.

3.3 Mechanical and Geometric Design Principles

System Force Balance

To compress the air within the pouch, the vertical force exerted by the user's foot (F_{foot}) must overcome the internal resistive forces of the system. As shown in the simplified free-body diagram in Figure 3.3, these resistive forces are the sum of the force exerted by the rebound spring (F_{spring}) and the force from the gas pressure inside the pouch ($F_{pressure}$). Therefore, for air to be delivered to the reservoir, the condition $F_{foot} > F_{spring} + F_{pressure}$ must be met.

This force balance has a direct implication for the system's operation. The spring force, F_{spring}, is a function of the mechanism's compression. The gas pressure force, $F_{pressure}$, is proportional to the pressure in the storage tank. As the tank pressure rises with each step, $F_{pressure}$ increases, and therefore the total resistive force that must be overcome by the user also increases.



Figure 3.3: A simplified free-body diagram illustrating the force balance required for compression. The user-applied foot force must be greater than the sum of the mechanical spring's restoring force and the force from the internal gas pressure. This highlights the two primary sources of resistance the user must overcome during the stance phase.

Static Analysis for Pouch Cross-Sectional Area

While the full system is dynamic, a simplified static model is required to define the theoretical design boundaries. It is a well-understood engineering principle that real-world dynamic systems rarely achieve the ideal performance predicted by static models due to inefficiencies such as friction and dynamic losses. Therefore, to ensure the final design has a reasonable chance of achieving the official **1.2 bar KPI** under dynamic walking conditions, a higher static pressure target must be used for the initial design calculation.

Applying a moderate safety factor, a static design target of **2 atm** (202,650 Pa) was chosen. Using the fundamental relationship $P = F/A$, we can calculate the maximum allowable cross-sectional area (A_{max}) that could theoretically achieve this target with the 700 N of available foot force from Chapter 2:

$$A_{max} = \frac{F_{foot}}{P_{design_target}} = \frac{700\,\text{N}}{202,650\,\text{Pa}} \approx 0.00345\,\text{m}^2 = 34.5\,\text{cm}^2 \tag{3.1}$$

This calculation establishes a critical theoretical upper limit for the pouch's footprint. To be confident in achieving the 1.2 bar dynamic KPI, the final pouch area should not exceed approximately 34.5 cm^2. However, as discussed in the following chapter, this theoretical boundary is further constrained by the practical realities of fitting the entire mechanopneumatic system into a standard shoe.

3.4 Derivation of the Dynamic Mass Flow Model

To predict the system's charging behavior over time, a quantitative model for the mass of air added to the tank per cycle (Δm_{tank}) is derived from the principle of conservation of mass. A

key assumption is that the process is **isothermal**, a simplification justified by the slow cycle time and which will be experimentally validated in Chapter 6.

Step 1: Define the Total Mass of the System

At any given moment after a compression cycle, the system is at an equilibrium pressure P_{tank}. The total mass of air (m_{total}) is the sum of the mass in the clearance volume of the pouch (m_{cl}), the tube (m_{tube}), and the tank (m_{tank}). Using the Ideal Gas Law ($m = PV/RT$):

$$m_{total}(t) = \frac{P_{tank}}{RT}(V_{cl} + V_{tube} + V_{tank}) \tag{3.2}$$

Step 2: Define the Mass of Air Intake

After one full cycle, a new mass of fresh air (m_{intake}) is drawn into the pouch. The volume of this fresh air is the maximum pouch volume (V_{pump}) minus the volume that the trapped clearance gas re-expands into ($V_{re-expansion}$). For an isothermal process, $P_{tank}V_{cl} = P_{atm}V_{re-expansion}$, so $V_{re-expansion} = V_{cl}(P_{tank}/P_{atm})$. The mass of fresh air taken in is therefore:

$$m_{intake} = \frac{P_{atm}}{RT}(V_{pump} - V_{re-expansion}) = \frac{V_{pump}P_{atm} - V_{cl}P_{tank}}{RT} \tag{3.3}$$

Step 3: Apply Conservation of Mass to Find the New State

The total mass in the system after the next cycle, m'_{total}, is the sum of the initial mass and the intake mass. Solving for the change in system pressure, ΔP_{system}, yields:

$$\Delta P_{system} = \frac{V_{pump}P_{atm} - V_{cl}P_{tank}}{V_{cl} + V_{tube} + V_{tank}} \tag{3.4}$$

The change in mass *in the tank only* is $\Delta m_{tank} = \Delta P_{system} \cdot (V_{tank}/RT)$. Substituting and defining the clearance ratio as $c = V_{cl}/V_{pump}$, we arrive at the final governing equation:

$$\Delta m_{tank} = (P_{atm} - c \cdot P_{tank}) \cdot \frac{V_{pump} \cdot V_{tank}}{RT \cdot (V_{cl} + V_{tube} + V_{tank})} \tag{3.5}$$

3.5 The Theoretical Characteristic Curve

Equation 3.5 represents the central theoretical hypothesis of this work. It predicts a linear relationship between the back-pressure in the reservoir and the mass of air delivered per cycle. This relationship is visualized qualitatively in Figure 3.4. This theoretical curve serves as the fundamental guide for the system's design and the primary benchmark for the experimental validation conducted in Chapter 6.

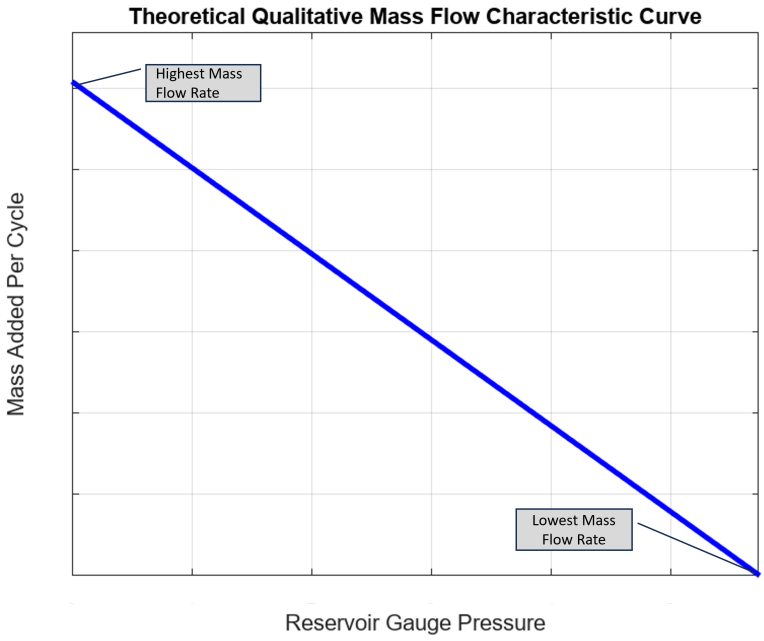


Figure 3.4: Qualitative representation of the theoretical mass flow characteristic curve, derived from the analytical model (Equation 3.5). This plot illustrates the core hypothesis of the system: the mass of air added per compression cycle is a linear function of the reservoir's back-pressure. Mass flow is highest when the reservoir is at atmospheric pressure and decreases linearly to zero at the theoretical "stall pressure."

4. An Empirical Journey to a Viable Compressor Design

The theoretical analysis in the preceding chapters established the fundamental principles of the pressure harvesting system. However, it also highlighted a fundamental conflict between the primary design objectives of high pressure, low profile, and high flow rate. It became evident that a purely analytical approach would be insufficient to navigate these competing requirements.

This chapter details the empirical and iterative design strategy that was consequently adopted. The process involved the systematic fabrication and testing of physical prototypes, not with the expectation of immediate success, but to utilize each iteration as a diagnostic tool. This process of empirical investigation, driven by practical failures and the constraints they revealed, systematically guided the project from its initial broad concepts to a single, functional, and manufacturable final design.

4.1 The Initial Design Challenge: Reconciling Competing Goals

As established in Chapter 3, the design objectives are governed by competing physical principles. Achieving high pressure ($P = F/A$) with a fixed footstrike force (F) mandates a small compressor area (A). Conversely, achieving a high flow rate, which is dependent on volume displaced per unit time ($\Delta V/t$), benefits from a large area and a large compression stroke (h). The initial 10 mm wearability target imposed a severe restriction on this stroke height, placing the three core objectives in direct opposition.

4.2 A Strategy of Iterative Prototyping and Learning

Faced with these analytical conflicts, an empirical, iterative design strategy was adopted. The methodology was to employ a process of iterative fabrication and empirical testing to uncover the dominant, real-world performance bottlenecks that are often invisible in theoretical models. Each iteration was designed to test a specific hypothesis and, whether through success or failure, provide critical data to inform the subsequent design cycle.

4.3 Iterative Prototype Development and Analysis

The development process progressed through three major design iterations, each of which revealed fundamental limitations that progressively narrowed the field of viable solutions.

Iteration 1: The Passive Mechanofluidic Pump

The first prototype explored the simplest possible configuration: a purely passive system intended to validate the basic concept of a textile compressor.

Design and Fabrication This initial concept, shown in Figure 4.1, consisted of a heat-sealed, TPU-coated nylon pouch containing an open-cell sponge to provide a passive rebound force. The fabrication process, illustrated in the schematic in Figure 4.2, was straightforward, relying on commercially available check valves to direct airflow.

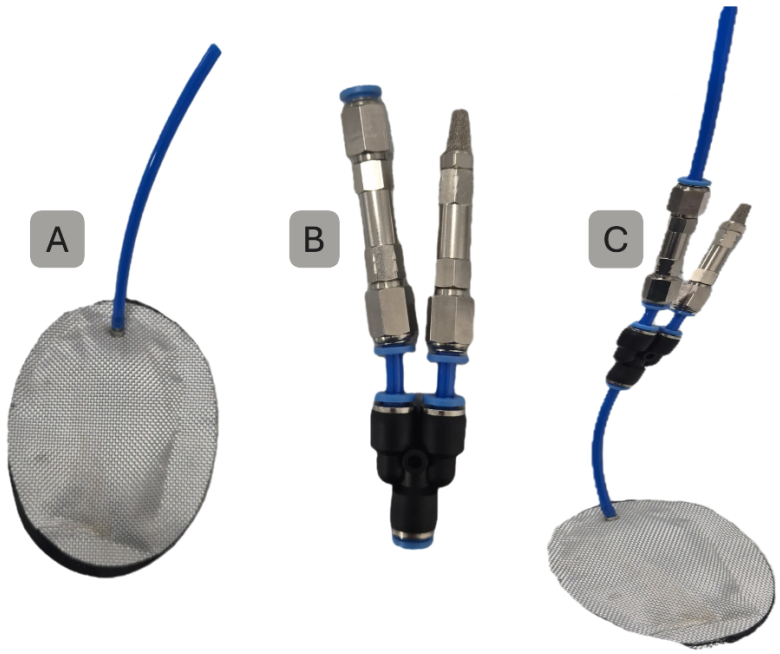


Figure 4.1: The passive mechanofluidic system of the first prototype iteration. Key components shown are (A) the heat-sealed textile pouch with an internal sponge, (B) the pneumatic manifold assembly, and (C) the fully integrated device.

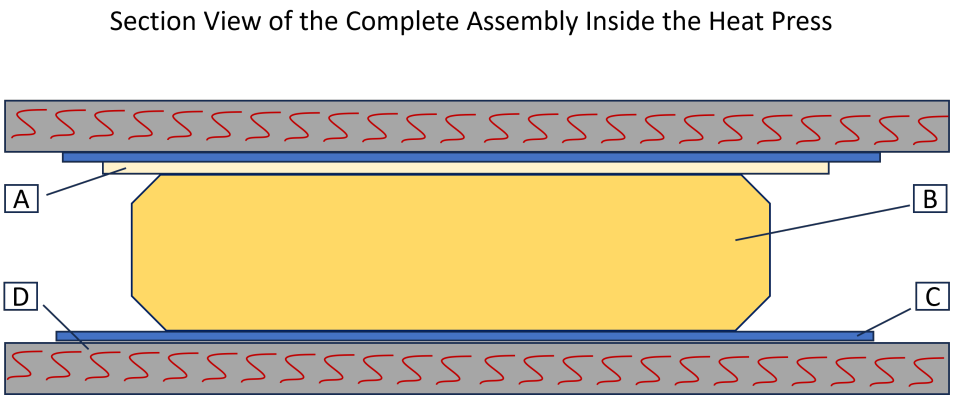


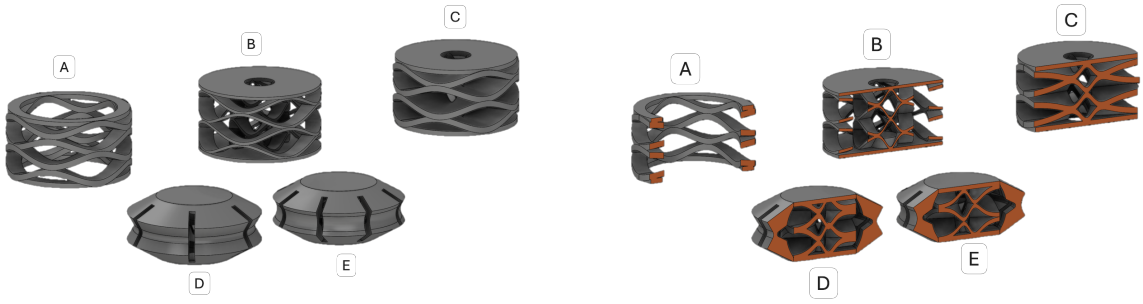
Figure 4.2: Conceptual cross-section of the fabrication for the passive pump (Iteration 1). An open-cell sponge (B) is sandwiched between two layers of TPU-coated fabric (A and C) and sealed by heated platens (D). This simple approach failed as the sponge's restoring force was too slow for a viable intake stroke.

Outcome and Analysis The prototype failed to generate any measurable pressure. This failure highlighted two critical bottlenecks: the low-force, low-speed rebound of the sponge was insufficient to overcome the cracking pressure of the check valves, and it was too slow to allow the pouch to fully re-inflate during a normal gait cycle.

Key Learning: This experiment uncovered the first fundamental design constraint: **a fast, active rebound mechanism is non-negotiable.**

Iteration 2: The Quest for a Volumetrically Efficient Internal Spring

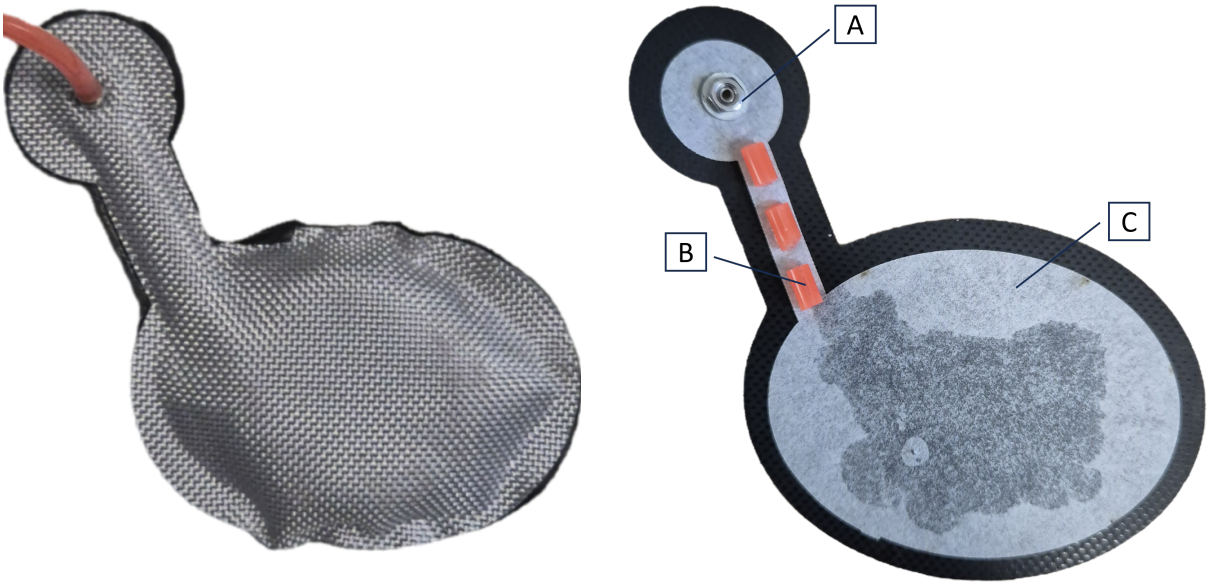
The subsequent iterations focused on developing an active rebound mechanism integrated inside the pouch. This phase involved an intensive, empirical 3D modeling effort (Figure 4.3) to design a spring structure that could be 3D-printed from TPU and sealed within the pouch.



(a) Isometric view of spring iterations. (b) Cross-section view of iterations.

Figure 4.3: CAD models illustrating the empirical design evolution of the internal TPU rebound springs (Iteration 2). Five distinct spring geometries (A-E) were developed to find a structure that could collapse to a minimal height while providing sufficient restorative force.

Design and Fabrication The physical realization of this concept, shown in Figure 4.4, revealed further practical challenges. The pneumatic fitting had to be placed on the top surface of the pouch, creating an uncomfortable protrusion. More critically, the narrow airway leading from the fitting to the main chamber would collapse under negative pressure during intake, acting as an unintentional check valve and preventing the pouch from filling. This required a workaround where small, super-glued tube segments were used to stiffen the airway.



(a) Completed Iteration 2 prototype. (b) Internal view before sealing.

Figure 4.4: Physical prototype of the internal spring concept (Iteration 2). (a) The completed pouch shows the impractical, upward-facing push-fit fitting (A). (b) The internal view reveals the complexity: a non-stick paper mask (C) defines the cavity for the spring, while glued-in tube segments (B) were required to create a functional airway and prevent collapse during intake. These ad-hoc fixes highlighted the design's impracticality.

Outcome and Analysis While conceptually promising, this approach was defeated by a cascade of manufacturing and material science constraints, illustrated in Figure 4.5. The need to pre-compress the internal spring during heat-sealing created a direct conflict with the pressure required to form a reliable seal, leading to inconsistent results and a high risk of thermally damaging the spring.

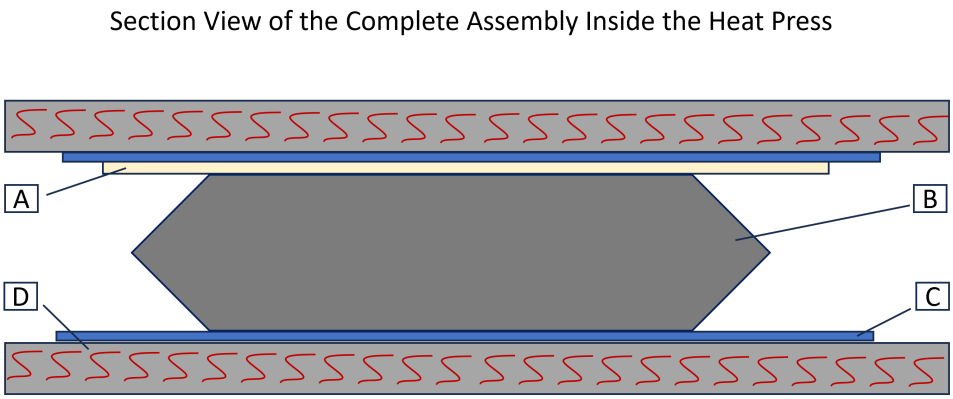


Figure 4.5: Illustration of the manufacturing challenges in the internal spring design (Iteration 2). The concept required sealing a 3D-printed TPU spring (B) between two layers of TPU-coated fabric (C), using non-stick paper (A) to define the unsealed chamber. The primary difficulty was that the assembly could not be sealed in a single press. Instead, it required a painstaking process of tracing the perimeter of the internal spring with the heat press (D) in multiple steps. This method was unreliable, often resulted in inconsistent seals, and could lead to an unintentionally large clearance volume (V_{cl}), defeating the purpose of the design.

Key Learning: This iterative cycle revealed that **the integration of a functional component inside the pouch creates prohibitive manufacturing challenges.**

Iteration 3: The Structured Pouch and the Sealing Failure Point

To circumvent the internal spring problem, a third approach was tested: creating a permanent 3D pouch structure by bonding the fabric to a 3D-printed frame. The complex, layered assembly is shown in Figures 4.6 and 4.7.

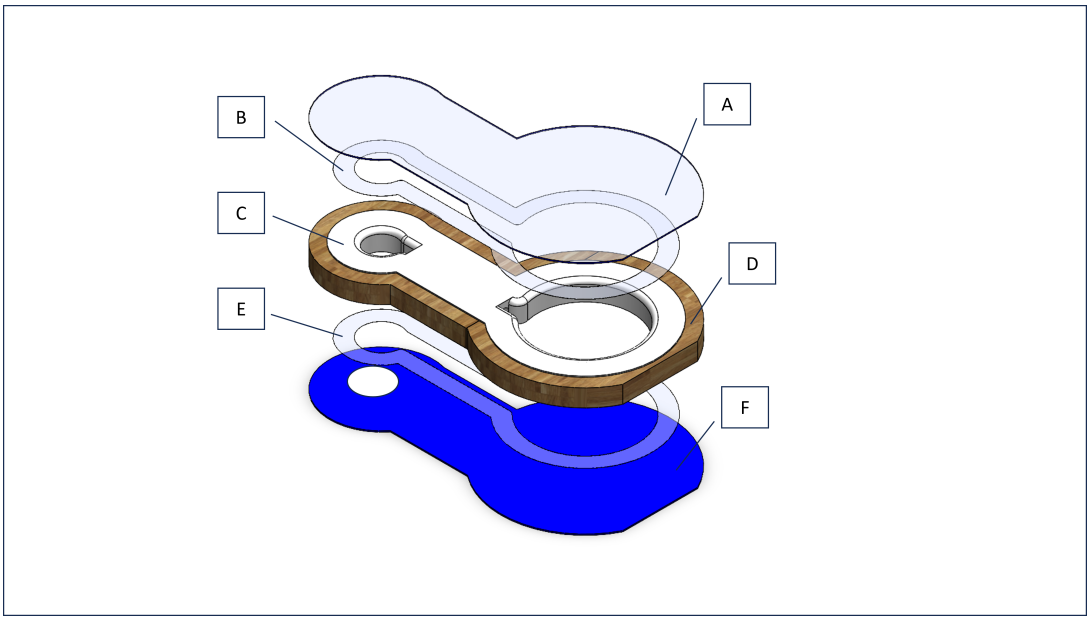


Figure 4.6: Exploded view of the layered assembly for the structured pouch concept (Iteration 3), showing the TPU fabric layers (A, F), non-stick masks (B, E), 3D-printed TPU frame (C), and wooden jig (D).

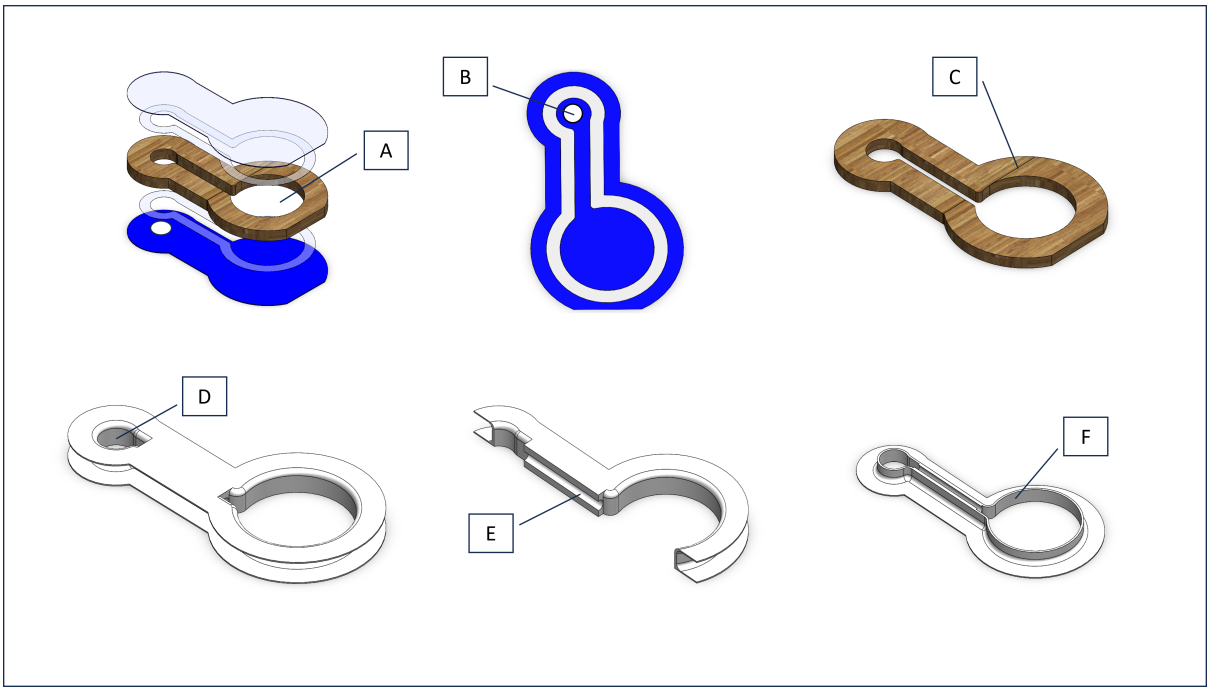


Figure 4.7: Detailed views of the individual components of the structured pouch concept (Iteration 3). The design's complexity is evident in its numerous specialized features: (A) an exploded view of the layered assembly. (B) The non-stick mask defines both the main compression chamber and the push-fit fitting hole. (C) The wooden jig was designed with a split for easier removal after heat-sealing. (D) The 3D-printed frame featured a hexagonal recess for a captive nut to secure the fitting. (E) A cross-section of the frame reveals the integrated air channel designed to route air from the compression chamber to the outlet. (F) The frame's raised wall was intended to give the pouch its third dimension. This high level of complexity ultimately contributed to the design's failure due to sealing issues at the material interfaces.

Outcome and Analysis This approach also failed, but for a new reason rooted in the manufacturing process itself (Figure 4.8). The prototype failed every leak test due to the inherent **micro-porosity** of the FDM-printed frame. Under pressure, microscopic voids in the print became a network of channels for air to escape.

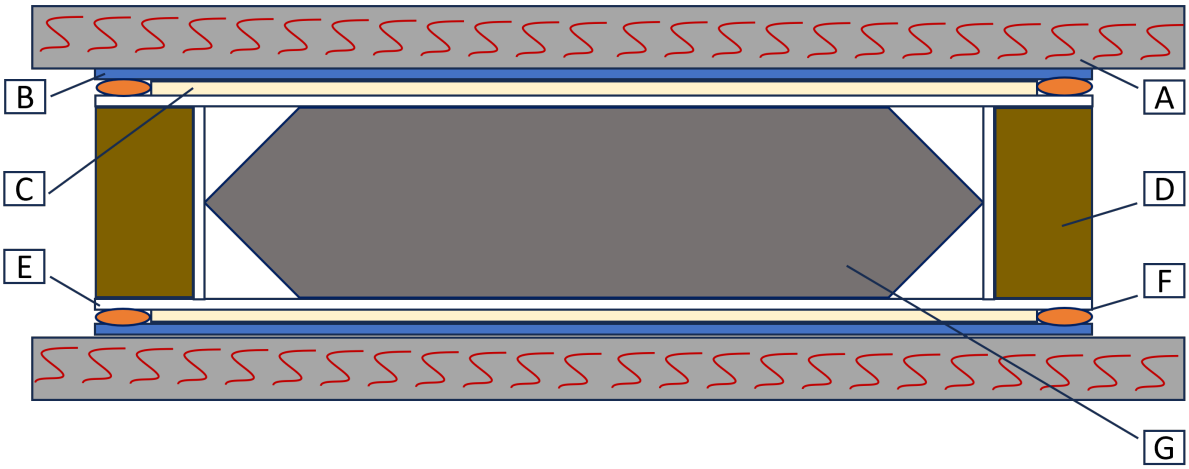


Figure 4.8: Cross-section of the structured pouch concept (Iteration 3) during fabrication. The design aimed to create a monolithic bond (F) between the TPU-coated fabric (B) and a 3D-printed TPU frame (E). The design failed due to the inherent micro-porosity of the FDM-printed frame (E), which prevented a reliable high-pressure seal.

Key Learning This design demonstrated that **integrating different material forms, even of the same base polymer, presents a critical sealing challenge.** Without industrial techniques like overmolding, creating a reliable high-pressure vessel by bonding a thin film to a bulk FDM part was determined to be unfeasible within the scope of this investigation.

4.4 Synthesizing the Lessons Learned

The cumulative knowledge gained from the prototyping cycle is summarized in Table 4.1. The process systematically eliminated design concepts based not on theory, but on demonstrated, practical failure modes. It became evident that any design wherein the spring and chamber were physically integrated was non-viable.

Table 4.1: Summary of Critical Lessons from the Prototyping Gauntlet.

Prototype	Key Failure Mode	Critical Lesson / Constraint Uncovered
1. Passive Sponge	Insufficient rebound force and speed.	An active, fast rebound mechanism is essential for operation at normal gait speeds.
2. Internal Spring	Geometric complexity, assembly difficulty (pre-compression), and thermal damage to the spring.	Placing components inside the compression chamber creates intractable manufacturing and material conflicts.
3. Structured Frame	Material porosity of the FDM frame led to leakage.	Standard FDM parts are unsuitable for creating a sealed pressure vessel without significant post-processing.

4.5 Strategic Re-evaluation of Design Objectives

The evidence gathered through the iterative prototyping process made it clear that the initial, ambitious KPIs established in Chapter 1 were mutually exclusive under the existing fabrication constraints. The goals of high pressure, high flow rate, and a minimal 10 mm profile could not be achieved simultaneously.

This led to a formal strategic pivot. A decision was made to prioritize the single most important metric for a functional proof-of-concept: **pressure generation**. The other ambitious targets were formally relaxed. This new hierarchy, dictated by the practical lessons learned, was as follows:

Priority 1 (Primary Mandate - Maintained) Achieve a gauge pressure of approximately **1.2 bar**. This was reaffirmed as the primary measure of functional success.

Priority 2 (Air Supply Rate Mandate - Maintained) Achieve an air supply rate of approximately **0.36 SLPM**, consistent with the goal of offloading 10% of the energy burden from a primary system.

Priority 3 (Wearability Constraint - Relaxed) The strict 10 mm thickness target was abandoned in favor of a more practical constraint: the height could be increased as necessary, provided the final design remained integrable and wearable in a shoe.

Priority 4 (Secondary Metrics) Power output would be accepted as a resultant property of the final design, to be measured and characterized.

This strategic re-evaluation was critical, as it focused the remainder of the design effort on creating a system that could successfully validate the core concept of the de-coupled architecture, even if it did not meet all of the original, ambitious performance numbers.

4.6 The Convergent Design: A Concept Born from Constraints

The revised hierarchy led directly to the final design concept: a simple, empty pouch for compression, paired with a completely separate, external rebound spring. This architecture was selected because it was the only one that effectively addressed every single constraint discovered during prototyping.

A critical design trade-off emerged at this stage. While the de-coupled design freed up space *inside* the pouch (by removing the spring), the external rebound mechanism now occupied valuable volume *within the shoe*, competing for space with the pouch itself. This real-world

spatial constraint necessitated a smaller pouch than the theoretical maximum of 58.3 cm^2 calculated in Chapter 3. A practical design choice was made to use a circular compression chamber with a diameter of **35 mm**, resulting in a cross-sectional area of **9.62 cm^2**.

A static analysis of this final, compact design reveals its high theoretical potential. With an available force of 700 N, the maximum static pressure is:

$$P_{static} = \frac{F_{foot}}{A_{final}} = \frac{700\,\text{N}}{0.000962\,\text{m}^2} \approx 727,650\,\text{Pa} \approx 7.2\,\text{bar} \tag{4.1}$$

This result is profound. It demonstrates that the final, compact pouch design is theoretically capable of generating pressures far exceeding the 1.2 bar KPI. This proves that the design's geometry is not the limiting factor, and that any failure to meet the performance target must be attributed to other real-world inefficiencies, such as the clearance ratio.

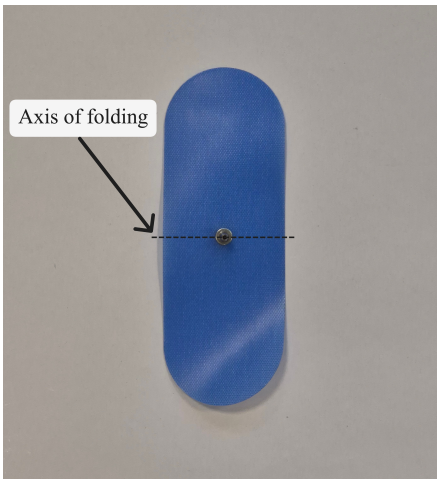
This final concept, including the innovative one-piece folded fabrication method (Figure 4.9), was the logical conclusion of the iterative development process. The detailed build of the prototype based on this design is the subject of the next chapter.



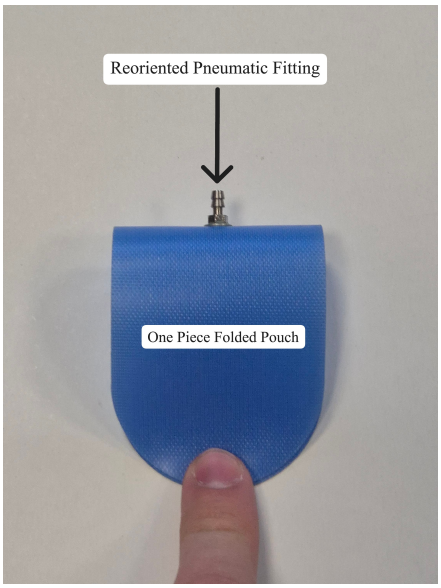
(a) Initial two-piece design concept.



(b) Resulting impractical vertical fitting.



(c) Revised single-piece pattern.



(d) Final folded pouch with horizontal fitting.

Figure 4.9: Evolution of the pouch fabrication method to solve the pneumatic fitting orientation problem. (a) The initial concept utilized two separate fabric pieces. (b) This method resulted in a vertical fitting unsuitable for bearing load. (c) The revised method uses a single, symmetrical, laser-cut fabric pattern. (d) When folded, this one-piece design naturally reorients the fitting into a robust and low-profile horizontal position.

The simple and effective fabrication process for the final pouch is illustrated in the schematic in Figure 4.10.

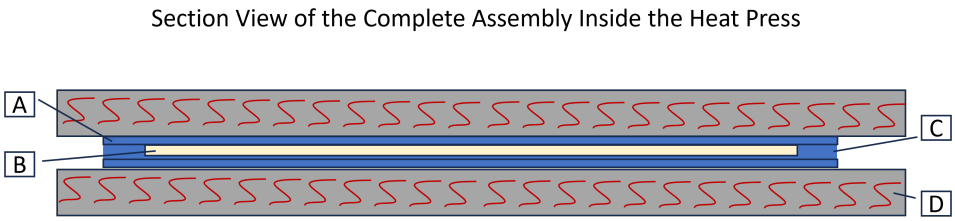


Figure 4.10: Fabrication schematic of the final, convergent pouch design. A single piece of TPU-coated fabric (A) is folded (C), and a parchment paper mask (B) is placed inside before being sealed by the heat press (D). This simple approach eliminates all previously identified failure modes and maximizes potential volumetric efficiency.

This final, refined concept was the logical conclusion of the iterative development process, addressing all identified failure modes:

- It provides an **active rebound** via an external mechanism (satisfies Lesson 1).
- The compression chamber is **completely unobstructed** (satisfies Lesson 2).
- The pouch is a **single, continuous sealed textile** with a practical fitting orientation (satisfies Lesson 3 and the final fabrication challenge).

The detailed design and fabrication of the full prototype based on this convergent design is the subject of the next chapter.

5. System Architecture, Design, and Fabrication

Following the iterative design process detailed in Chapter 4, a final convergent design was selected that prioritized pressure generation and manufacturability. This chapter presents the complete design and fabrication of that prototype. The system is realized as two distinct but tightly integrated subsystems: 1) a **Mechanopneumatic Subsystem** responsible for harvesting biomechanical energy and compressing air, and 2) an **Electropneumatic Control Subsystem** that manages and regulates the harvested pneumatic energy.

5.1 Overall System Architecture

The system is designed as a modular, self-contained, wearable power harvesting system intended for bilateral deployment on both feet. As shown in the architectural diagram (Figure 5.1), mechanical energy from the user's gait is the primary input. This force drives the Mechanopneumatic Subsystem. The state of this subsystem is monitored by the Electropneumatic Control Subsystem, which uses sensor data to make decisions about air regulation and storage, and provides feedback to the user or a downstream robotic application.

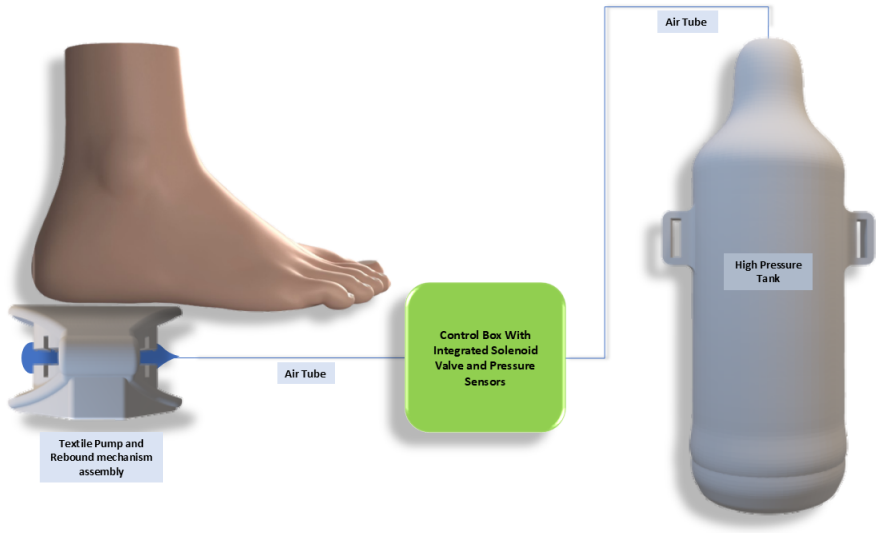


Figure 5.1: High-level architecture of the integrated pressure harvesting system, illustrating the relationship between the mechanopneumatic and electronic control subsystems and the flow of force, air, and data.

5.2 The Mechanopneumatic Subsystem: Energy Harvester

This subsystem is the mechanical core of the device. It consists of the textile compressor and the external hybrid rebound mechanism, which were designed to function as a single, integrated unit.

Opposing Diaphragm Compressor

The core of the mechanopneumatic subsystem is an **opposing diaphragm compressor**, custom-fabricated from a soft, heat-sealed textile pouch [17]. The final design, based on the convergent concept established in Chapter 4, is engineered to maximize volumetric efficiency and durability.

Material Selection A high-performance composite textile was selected for the pouch fabrication based on availability and preliminary testing. Specifically, an 840 denier (840D) nylon fabric with a thermoplastic polyurethane (TPU) coating on both sides was chosen. Coarse mechanical testing indicated that this material could withstand internal pressures exceeding the 2 atm target without tearing or delamination. Its high tensile strength and abrasion resistance ensure durability under the repetitive loading of gait, while its excellent thermal weldability is critical for creating a robust, monolithic, and leak-proof seal.

Geometric Design Based on the design decisions made in Chapter 4, the final pouch was designed with a circular compression chamber of 35 mm diameter, resulting in a cross-sectional area of **9.62 cm**^{2}. The final geometry, shown in Figure 5.2, includes integrated mounting flaps, or ”ears,” which serve as the anchor points for the external rebound mechanism, and a small internal tube segment affixed along the inner fold to prevent the airway from collapsing during the intake stroke. Excess material was carefully trimmed with hand scissors to ensure a clean, ergonomic fit within the confines of a standard shoe.

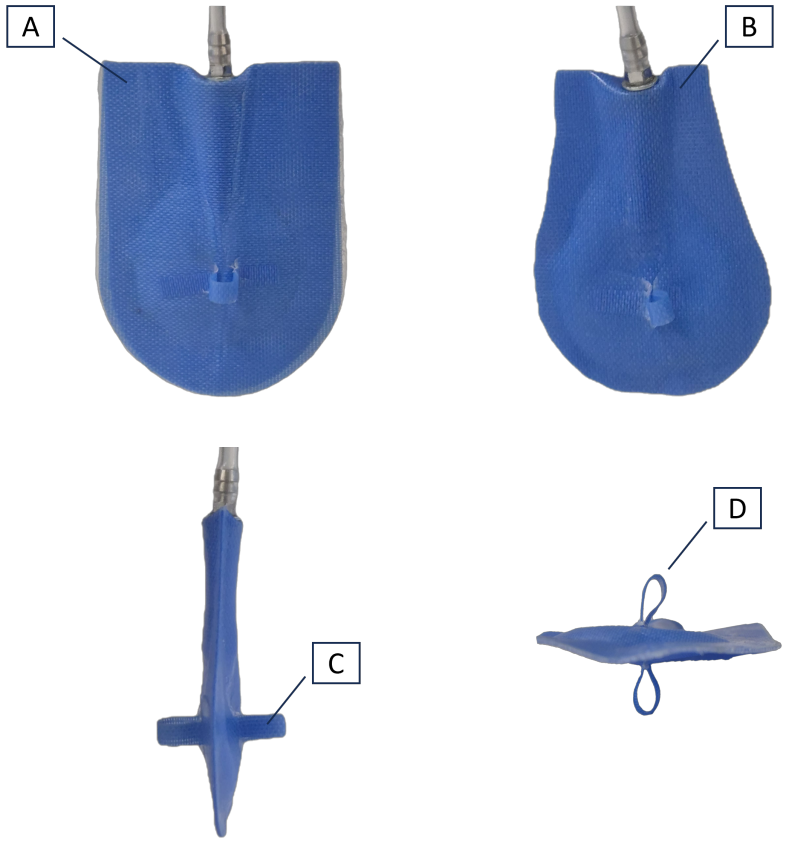


Figure 5.2: Different views of the final fabricated textile pouch. (A) The initial untrimmed shape was based on the projected heel contact area. (B) This was then manually trimmed for an optimal fit inside a standard shoe. (C) The side view and (D) front view highlight the integrated mounting flaps, which were created by fusing additional fabric strips into loops to create robust anchor points for the rebound mechanism.

Fabrication Process The pouch was fabricated using the one-piece folded method developed in the previous chapter to ensure a robust, low-profile fitting orientation. The process is as follows:

1. A single, symmetrical pouch pattern is precisely cut from the TPU-coated fabric using a laser cutter.

2. To form the internal chamber, a sheet of non stick baking paper, cut to the shape of the desired cavity, is affixed to one inner side of the folded fabric. This parchment acts as a bond-resistant mask, preventing the inner surfaces from bonding during the sealing process.

3. The entire assembly is placed in an impulse heat sealer, where controlled temperature and pressure are applied to fuse the perimeter into a strong, monolithic, and airtight seam.

4. Each completed pouch is then pressure tested to over 2 bar to ensure the integrity of the seal before being integrated with the rebound mechanism.

Hybrid Rebound Mechanism

The iterative prototyping in Chapter 4 demonstrated that a powerful, active rebound was non-negotiable. This led to the development of a robust hybrid system combining a compliant 3D-printed structure with high-force metal springs. The components of the assembly are shown in the exploded view in Figure 5.3, while the fully assembled unit is shown in Figure 5.4.

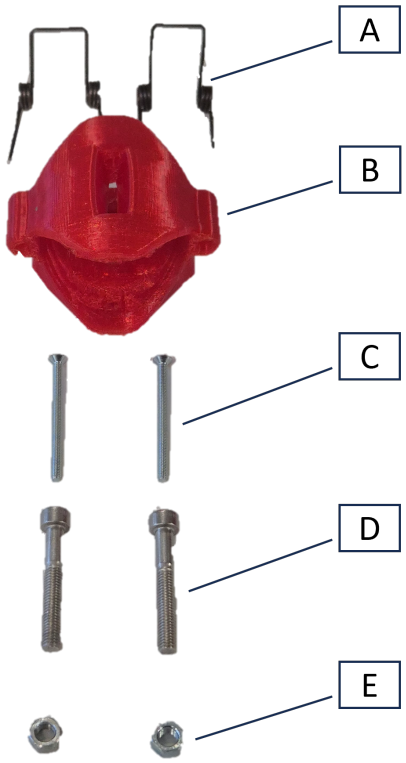


Figure 5.3: Exploded view of the hybrid rebound mechanism. The assembly consists of: (A) two high-force metal torsion springs; (B) a 3D-printed TPU housing; (C) two M3 bolts for clamping; and (D, E) two M5 bolts and corresponding nuts that serve as axles for the springs.

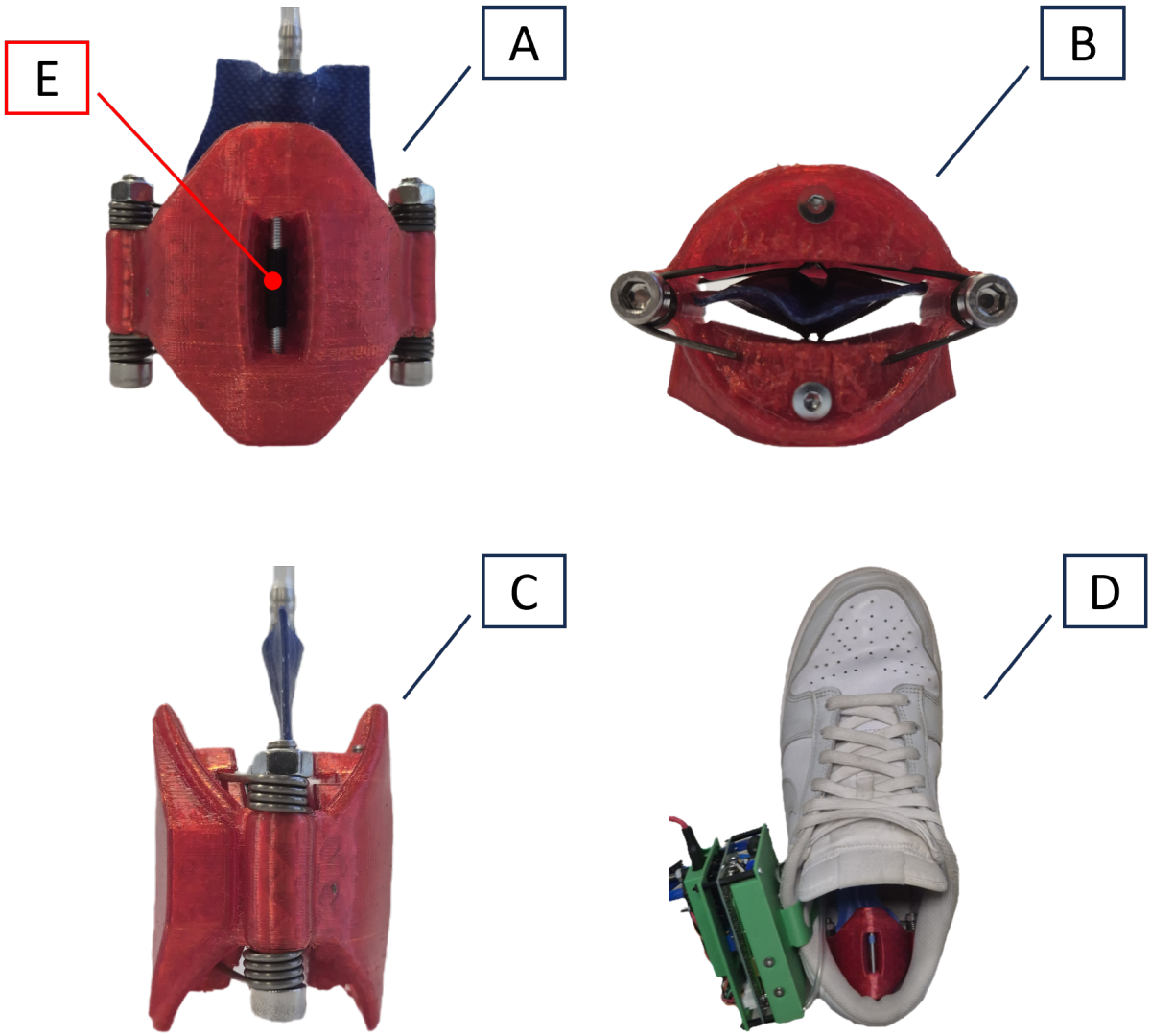


Figure 5.4: The fully assembled mechanopneumatic compressor unit. (A) The front view shows the textile pouch integrated with the rebound mechanism. (B) The bottom view reveals the torsion springs providing the restorative force. (C) The side view shows the profile of the complete unit. (D) The assembly is shown placed within the heel of a shoe to illustrate its scale and intended fit. (E) This detail highlights the ”sandwich clamp” method, where the M3 bolts securely anchor the pouch’s fabric mounting flaps.

Material and Design Rationale The core of the mechanism is a compliant housing fabricated from **95A durometer TPU** using Fused Deposition Modeling (FDM). This material was selected after empirical testing showed it offered a superior combination of elasticity and shape memory compared to more rigid materials like PLA or PETG. The housing was designed to be augmented with two metal **torsion springs**, which were selected empirically based on their ability to provide enough torque to fully re-expand the pouch during the brief swing phase of gait. The fastener selection was critical: **M5 bolts** were chosen as axles for their diameter, which prevents excessive play, while smaller **M3 bolts** provided a strong but low-profile clamping

force for the fabric flaps.

Integration and Operation The M5 bolts serve as axles for the torsion springs, whose arms are recessed into tight-tolerance pockets within the TPU housing to prevent them from ever touching or puncturing the fabric pouch. The pouch's mounting flaps are sandwiched between the top and bottom sections of the TPU housing, and the assembly is clamped together by the two M3 bolts. This "sandwich clamp" design distributes the clamping force over a wide area, ensuring a secure and durable load transfer from the housing to the fabric. During the stance phase, the footstrike overcomes the spring force to compress the pouch. During the swing phase, the stored elastic energy in the springs pulls the housing apart, ensuring a fast and complete intake of ambient air.

High-Pressure Reservoir

A common 500ml PET beverage bottle was utilized as a low-cost, readily available pressure vessel. To provide structural support and a means of mounting the reservoir to the user's belt, a custom case was designed in CAD and 3D-printed (Figure 5.5). All pneumatic connections are made with standard 4mm polyurethane tubing and push-to-connect fittings.



Figure 5.5: The custom 3D-printed case for the 500ml PET bottle reservoir, featuring integrated belt loops for wearability and the university logo.

5.3 The Electropneumatic Control Subsystem

This subsystem provides the intelligence to manage the harvested pneumatic energy. A purely passive system relying on mechanical check valves was deemed suboptimal for a downstream robotic application. By implementing an active electronic controller, the system gains precision, efficiency, and the flexibility to be tuned for different applications.

System Architecture and Hardware Selection

The system is designed around a **Leader/Follower** architecture to manage the bilateral harvesters efficiently. The ”Right Foot Control Box” acts as the Leader, containing an Arduino Nano that performs its own control tasks, communicates with the user, and requests data from the ”Left Foot Control Box” (the Follower) over an **I2C bus**. An I2C extender is used as a separate module to ensure signal integrity over the longer cable.

The hardware was selected based on a combination of performance requirements and the availability of lab equipment:

Microcontrollers: Two **Arduino Nanos** were chosen for their compact form factor and well-supported I2C libraries. The pin assignments are detailed in Figure 5.6.

Pressure Sensors: The system leverages two types of high-quality sensors. The main tank pressure is monitored by a trusted **NXP MPX5700AP** (Figure 5.7a). The pump line sensors were salvaged from damaged **SMC ITV0010** digital regulators (Figure 5.7b). Each sensor was individually calibrated, and its unique linear conversion formula was implemented in the code to ensure accuracy.

Solenoid Valves: The high-quality **24V solenoid valves** were also salvaged from the SMC regulators.

Power Source: A standard **USB power bank** (5V, 2.1A) serves as the primary power source. Two compact **DC-DC step-up converters** on each board efficiently generate the required 9V (for the Arduino Vin) and 24V (for the solenoids).

MOSFETs: **N-channel MOSFETs** are used as electronic switches, allowing the Arduino’s 5V logic to safely control the 24V valves.

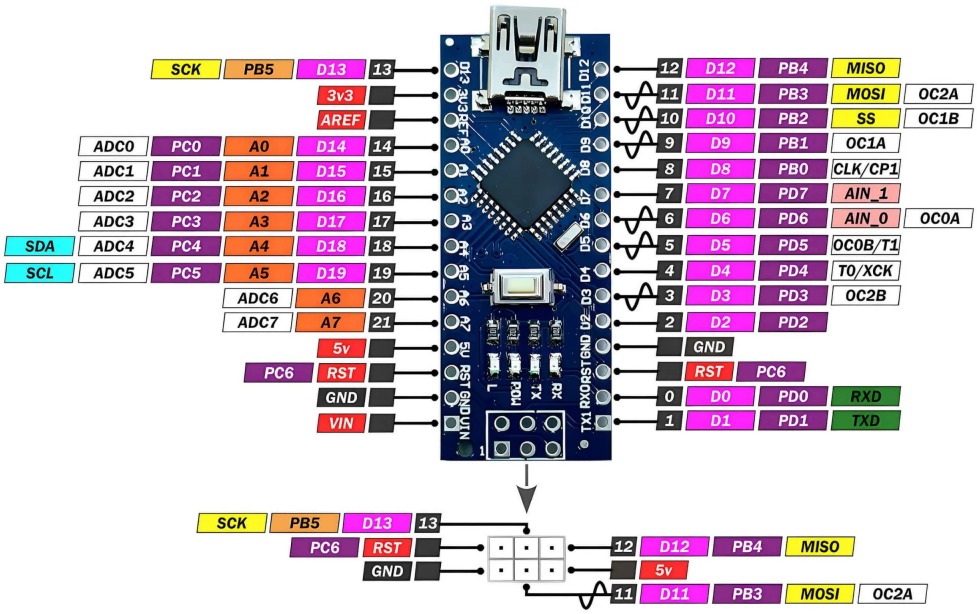
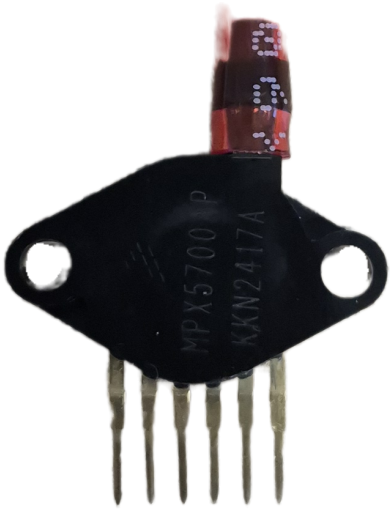
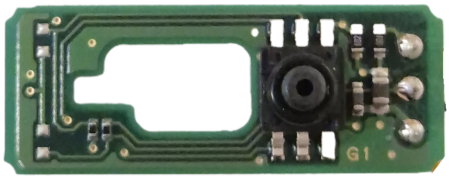


Figure 5.6: Pinout mapping for the Arduino Nano, detailing the specific function of each pin utilized in the control system.

- **Power Management:** The board is powered by 9V via the **VIN** and **GND** pins. The regulated **5V** pin is used to provide a stable power source to the pressure sensors.
- **Analog Inputs:** The analog pins serve as the primary sensor interface. **A0** reads the analog signal from the main Tank Pressure Sensor, while **A1** reads the signal from the Pump Pressure Sensor.
- **Digital Outputs:** Digital pins **D3** and **D4** are configured as outputs to send 5V signals to the MOSFET modules, which in turn actuate the 24V intake and output solenoid valves, respectively.
- **Communication:** **A4 (SDA)** and **A5 (SCL)** are used for I2C communication, facilitating the Leader/Follower architecture between the two control boxes. Pins **D0 (RX)** and **D1 (TX)** are utilized for serial communication with a computer for real-time data logging and debugging.
- **Unused Pins:** All other digital and analog pins (D2, D5-D13, A2-A3, A6-A7) are not connected (NC) in this application.



(a) The NXP MPX5700AP sensor used for monitoring the main tank pressure.



(b) The PCB-level pressure sensor salvaged from an SMC ITV0010 unit, used for pump line monitoring.

Figure 5.7: The two types of pressure sensors utilized in the control system.

Pneumatic Integration and Control Logic

The core of the control logic on each Arduino is a **state machine** that functions as a **digital pressure regulator**, as visualized in the flowchart in Figure 5.8. Each controller independently manages its own pneumatics by reading its local sensors and actuating its valves. The Leader controller has the additional task of periodically requesting data from the Follower to update the shared display.

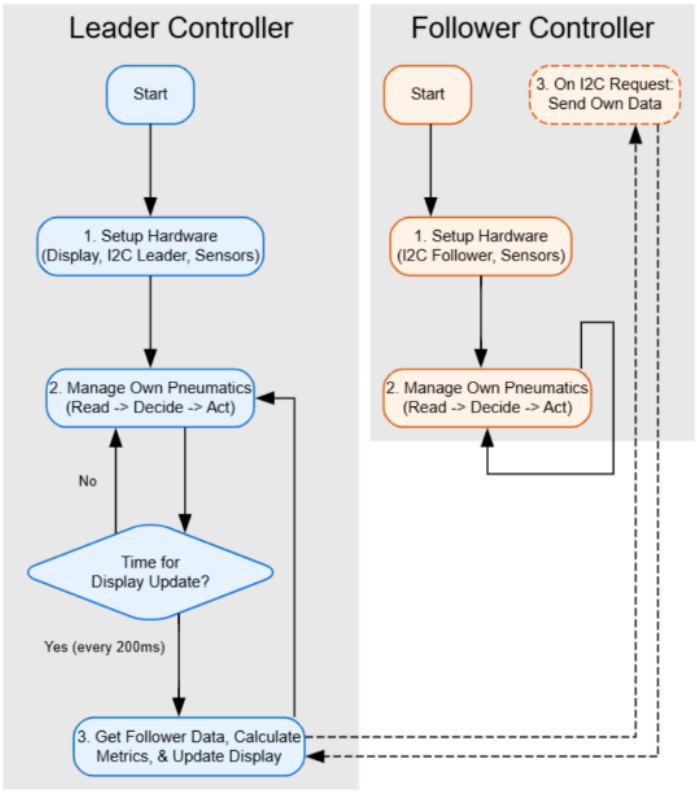


Figure 5.8: Flowchart illustrating the Leader/Follower control logic. Both controllers run an independent ”Read-Decide-Act” loop for their pneumatics. The Leader periodically requests data from the Follower via an I2C interrupt to update the central display.

The pneumatic hardware was organized around the salvaged **SMC ITV0010 manifold** (Figure 5.9). This component provides a compact, integrated block containing the two 2/2 solenoid valves, the proprietary SMC pump pressure sensor, and the complex internal routing shown in the pneumatic schematic (Figure 5.10). A custom 3D-printed cap was designed to enclose exposed parts of the salvaged unit. The manifold has three external ports: the **PUMP** port connects to the compressor and internally feeds the pump sensor; the **ATM** port is used for air intake; and the **TANK** port delivers harvested air to the reservoir. The main NXP tank pressure sensor is integrated via a T-fitting in the line leading from this TANK port.

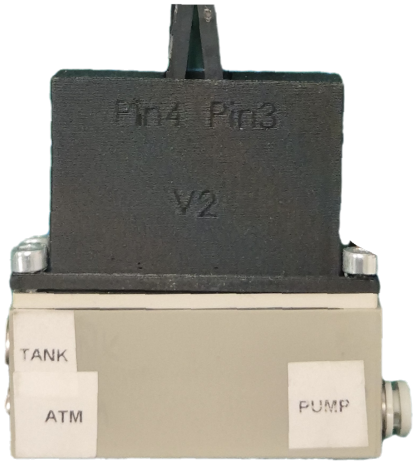


Figure 5.9: The salvaged SMC ITV0010 manifold, which integrates the two 24V solenoid valves and the pump pressure sensor into a single block. A custom 3D-printed cap was added to enclose exposed components.

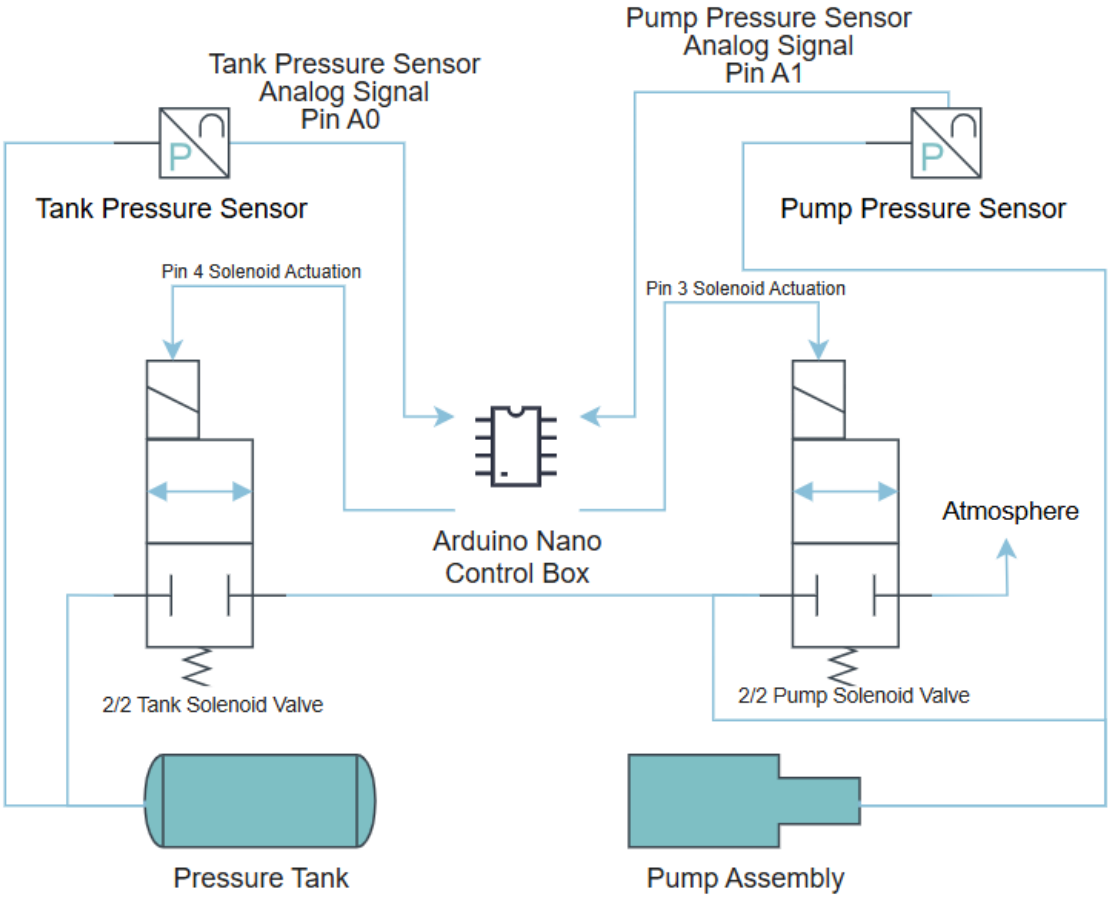


Figure 5.10: High-level pneumatic schematic of the control system for a single foot. The Arduino Nano functions as the control box, reading analog signals from the Tank and Pump pressure sensors and actuating the two 2/2 solenoid valves to manage airflow.

Electrical Design and Physical Implementation

The complete electrical design is detailed in the schematic in Figure 5.11. The physical circuit was prototyped through two major iterations, evolving from an initial V1 perfboard (Figure 5.12) and enclosure (Figure 5.13) to a more compact and organized V2 board (Figure 5.14) used in the final assembly.

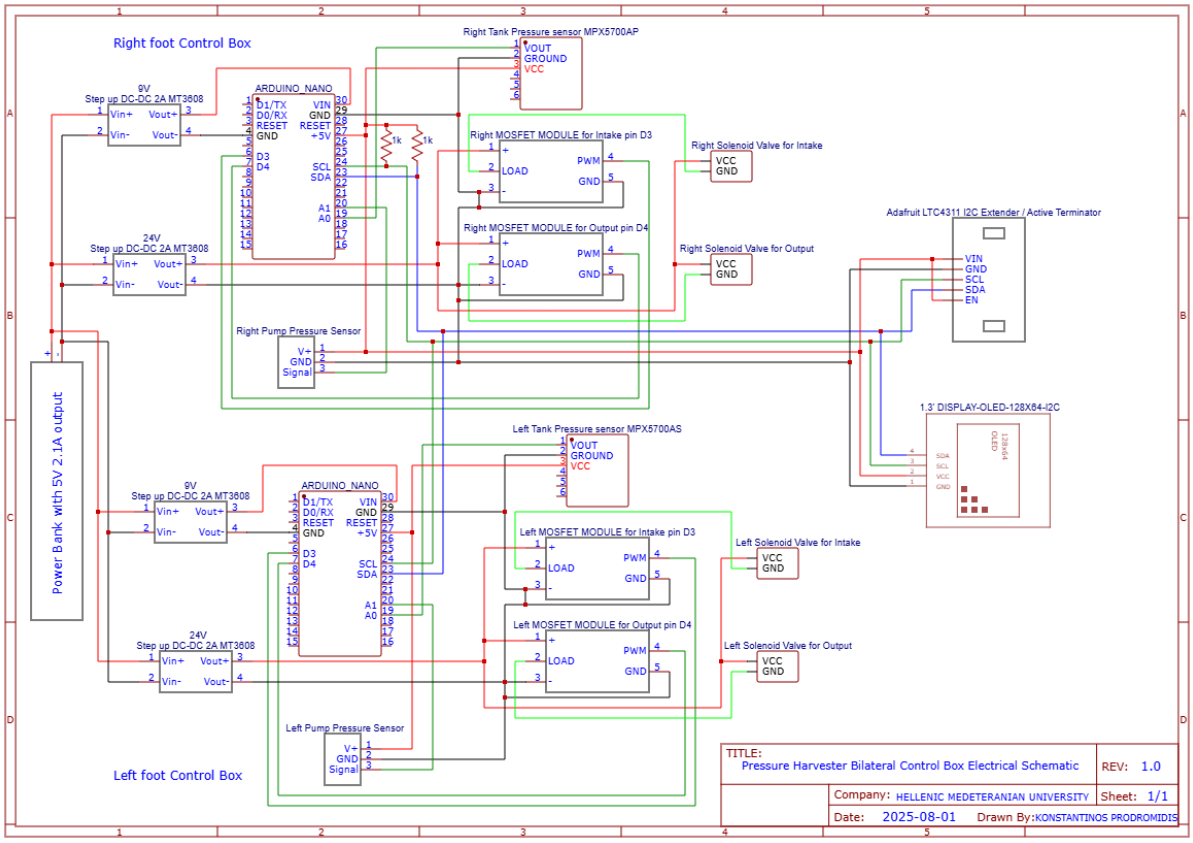


Figure 5.11: The complete electrical schematic for the bilateral control system. The diagram shows the Leader/Follower architecture, with two Arduino Nanos, independent power converters, and MOSFET valve drivers, all communicating via an I2C bus with a signal extender.

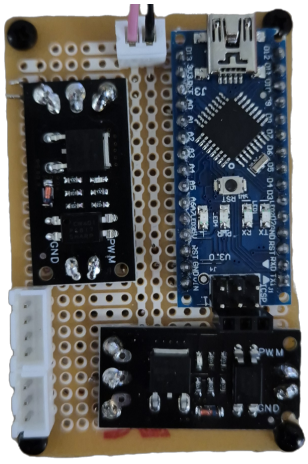


Figure 5.12: The initial V1 perfboard prototype for the Slave (Left Foot) controller, showing the Arduino Nano and two MOSFET modules.

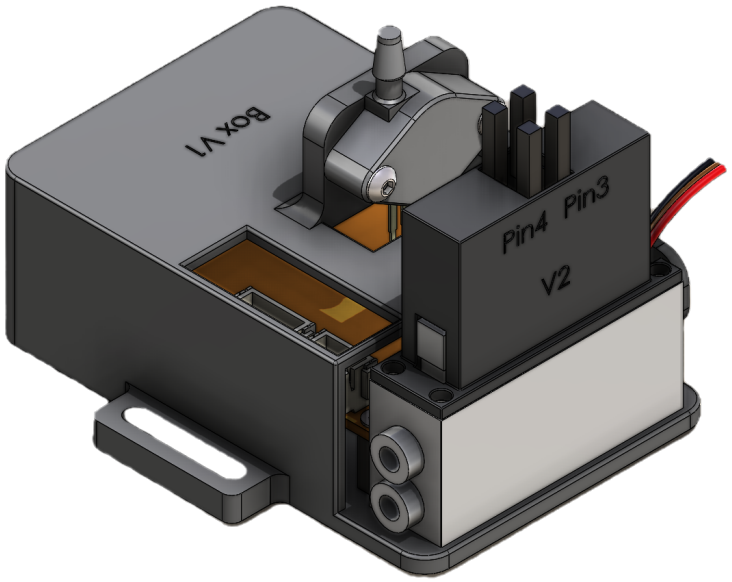


Figure 5.13: CAD model showing the integration of the V1 perfboard and the valve manifold into the first-generation control box design.

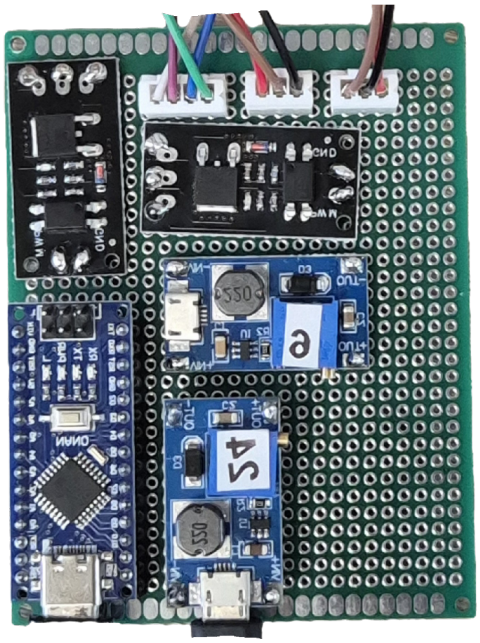


Figure 5.14: The final, more compact V2 perfboard for the Leader (Right Foot) controller, integrating the Arduino Nano, DC-DC step-up converters, and MOSFETs.

Enclosure and User Interface

The entire electronic subsystem is housed in a custom enclosure (Figure 5.15). As the enclosure serves only as a protective shell, it was rapidly prototyped using **PLA**. The user interacts with the system via a **1.3-inch I2C OLED display**, which provides critical real-time feedback on system performance (Figure 5.16).

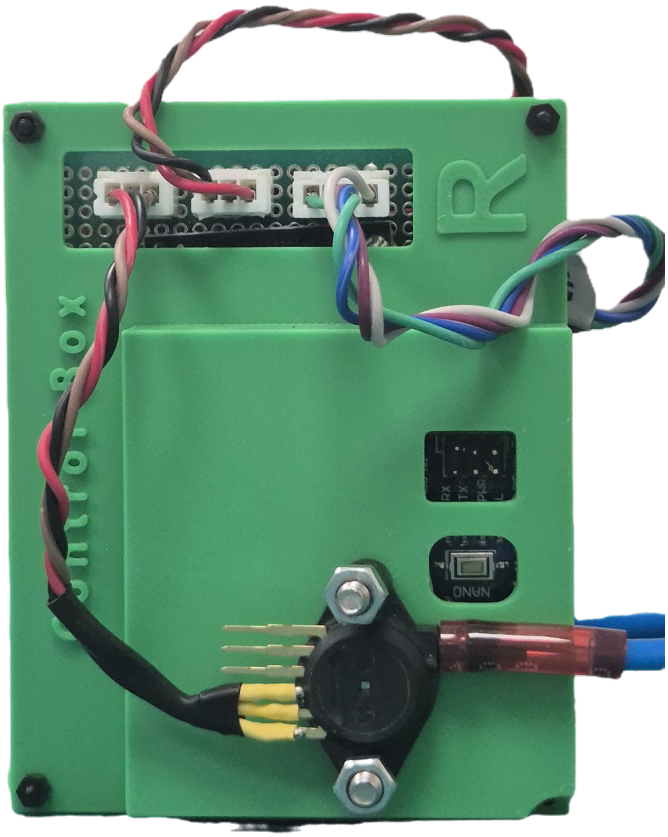


Figure 5.15: The fully assembled Leader (Right Foot) control box, housing all electronic and pneumatic management components.

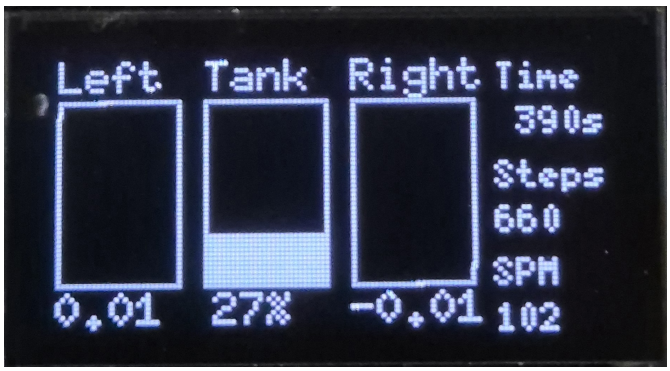


Figure 5.16: The user interface display, showing real-time performance metrics including individual pump pressures, tank pressure, runtime, step count, and steps per minute (SPM).

5.4 Final Assembled Prototype

The Mechanopneumatic and Electropneumatic subsystems are integrated into a complete, bilateral wearable system. Two identical mechanopneumatic units are embedded into shoe insoles and connected via pneumatic tubing to the single, belt-mounted control box and reservoir, as shown in Figure 5.17. This final prototype represents the culmination of the design and fabrication process, ready for experimental validation.

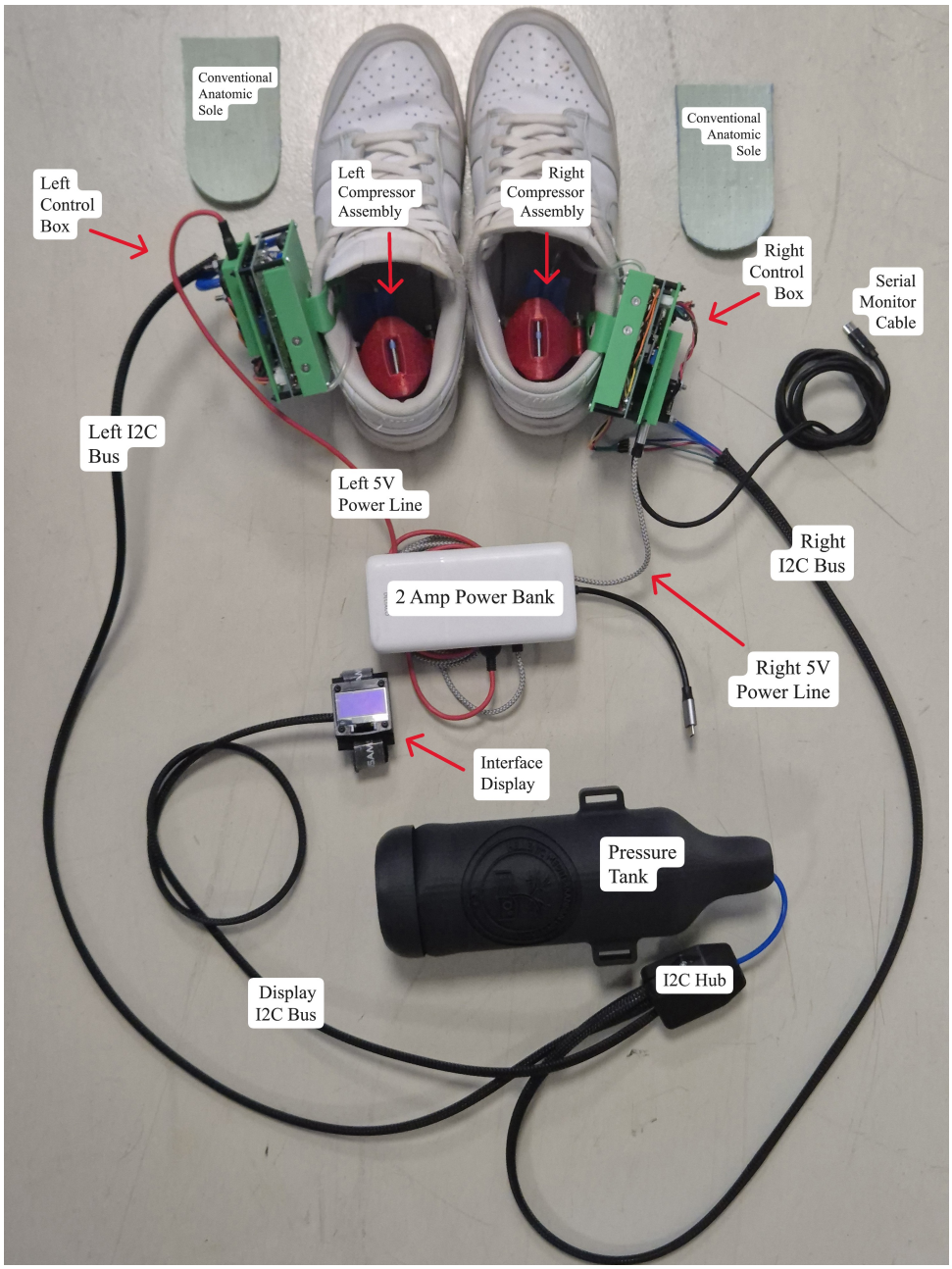


Figure 5.17: The fully integrated, bilateral pressure harvesting system, showing the shoe-mounted mechanopneumatic units and the belt-mounted electropneumatic control and storage unit.

6. Experimental Validation and Performance Characterization

With the prototype designed and fabricated, the next critical step is to rigorously quantify its real-world performance. This chapter details the experimental setups, protocols, and results of a series of tests designed to validate the system's capabilities. The tests progress from characterizing individual components to evaluating the fully integrated system under realistic operating conditions. The chapter culminates in a direct comparison of the experimental results against the theoretical predictions and revised performance targets.

6.1 Experimental Setup and Protocols

To ensure repeatable and accurate measurements, protocol of standard accessible equipment was introduced. Key instrumentation included:

- A Universal Testing Machine (UTM) for static mechanical characterization.
- A treadmill with adjustable speed to provide consistent stepping frequency.
- The onboard calibrated NXP MPX5700AP and Propriatery ITV0010 pressure sensors, cross-validated with a calibrated digital pressure gauge.
- A K-type thermocouple connected to a YATO YT-73083 digital multimeter.
- The serial monitor of the Arduino Nano Leader with a baud rate of 9600 bps.
- Standard 12 ml syringes with mild modifications. Custom hard stop at 10 ml to reduce human error.

6.2 Instrumentation and Sensor Calibration

Prior to system testing, a rigorous calibration procedure was performed on all pressure sensors to ensure data integrity and accuracy. As the final system utilizes two independent control boxes, each contains two distinct pressure sensors: one NXP sensor for the main tank (**MPX5700AP** for the right foot, **MPX5700ASX** for the left foot) and one proprietary sensor integrated into the repurposed **SMC ITV0010** valve block. A total of four sensors were therefore calibrated simultaneously.

Calibration Procedure All four sensors were connected to a single, common pressure line fed by a lab-developed pressure regulator, which provided a stable and adjustable source of known pressures. To eliminate potential voltage offsets and ensure a stable measurement baseline, both control boxes were powered by the same model of USB power bank used in the final wearable configuration. The pressure was applied across a range of 0 to 30 psi, and the raw analog-to-digital converter (ADC) values from all four sensors were logged via the Arduino's serial monitor.

Results and Analysis The collected data and the resulting linear models for all four sensors are presented in the comprehensive calibration plot in Figure 6.1.

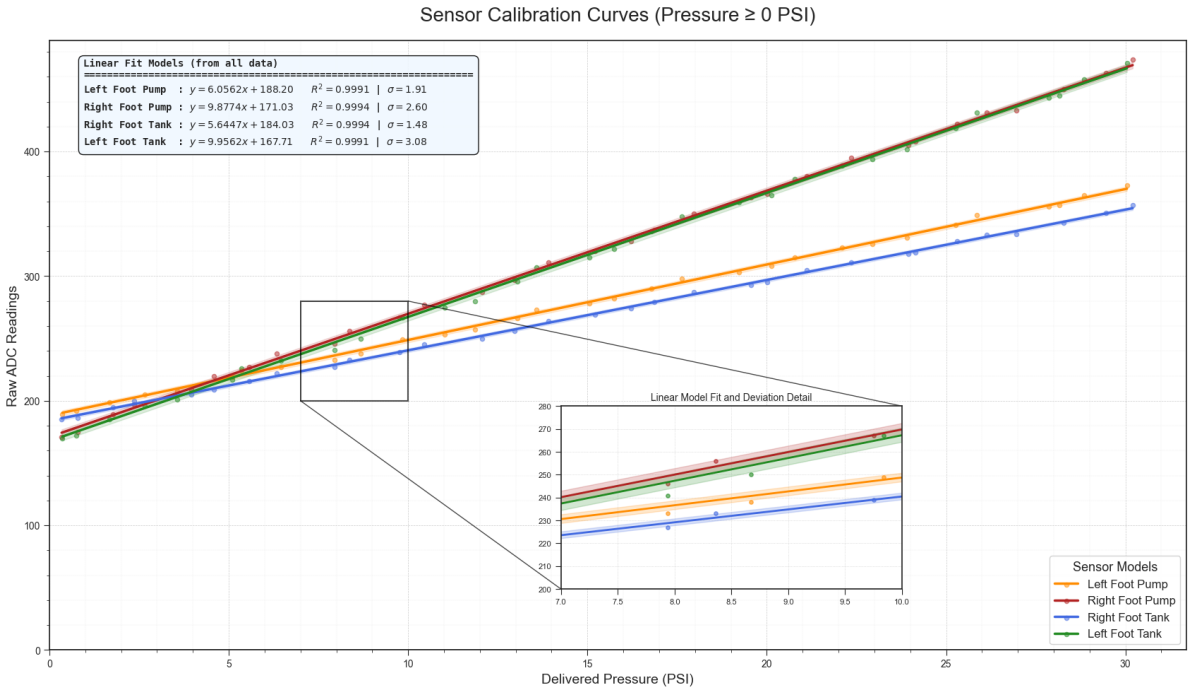


Figure 6.1: Comprehensive calibration curves for all four pressure sensors used in the bilateral system. The plot shows the raw ADC output as a function of the applied pressure in psi for the positive pressure range (≥ 0 psi). Each data series is fitted with a linear regression model, calculated from the full dataset including negative pressures, with the resulting equations and statistical parameters displayed in the top-left inset. The shaded regions represent the standard deviation (σ) for each linear model, indicating the band that contains approximately 68% of the data points. The magnified detail view highlights the close agreement between the raw data points and the linear fits. The specific linear models derived are:
Left Foot Pump: $y = 6.0562x + 188.20$ ($R^2 = 0.9991$)
Right Foot Pump: $y = 9.8774x + 171.03$ ($R^2 = 0.9994$)
Right Foot Tank: $y = 5.6447x + 184.03$ ($R^2 = 0.9994$)
Left Foot Tank: $y = 9.9562x + 167.71$ ($R^2 = 0.9991$)
The inverse of each of these unique equations was implemented in the control software and scaled to convert raw ADC values directly into pressure readings in standard atmospheres (atm).

The results confirm that all four sensors exhibit an exceptionally strong linear response to pressure, with all coefficients of determination (R^2) exceeding 0.997. This high degree of linearity provides the necessary confidence for the use of these sensors in all subsequent experiments. The inverse of each sensor's unique linear equation, as detailed in Figure 6.1, was then implemented in the Arduino control software to convert the raw ADC values directly into precise pressure readings in standard atmospheres (atm).

6.3 Component-Level Characterization

Before evaluating the integrated system, a series of tests were conducted on the core mechanopneumatic component to identify its key physical parameters. The goal of this section is to experimentally measure the real-world values for spring stiffness (k_{eff}), maximum volume (V_{max}), and clearance ratio (c), which were either estimated or treated as inputs in the theoretical model in Chapter 3.

Hybrid Spring Stiffness Analysis

To characterize the mechanical properties of the final hybrid rebound mechanism, the fully assembled mechanopneumatic compressor unit was mounted in a Universal Testing Machine (UTM). The unit was compressed at a controlled rate, and the resulting force and displacement were recorded to generate a force-displacement profile.

Results and Discussion The experimental force-displacement curve for the mechanism is shown in Figure 6.2. The data reveals that the relationship between force and displacement is largely linear, with a slight, progressive stiffening observed at higher compression values. This behavior is likely attributable to the combined kinematic effects of the TPU housing's geometry and the metal torsion springs. The test recorded a peak force of approximately **165 N** at a maximum displacement of **14.3 mm**.

To provide a useful metric for comparison against the theoretical model, an *effective linear stiffness* (k_{eff}) was calculated. A linear regression was applied to the central operating region of the curve (from 4 mm to 10 mm displacement), as this best represents the mechanism's behavior during a typical compression cycle. The slope of this linear fit indicates that the mechanism has an effective stiffness of approximately **10 N/mm**, which corresponds to:

$$k_{eff} \approx 10,000\,\text{N/m} \tag{6.1}$$

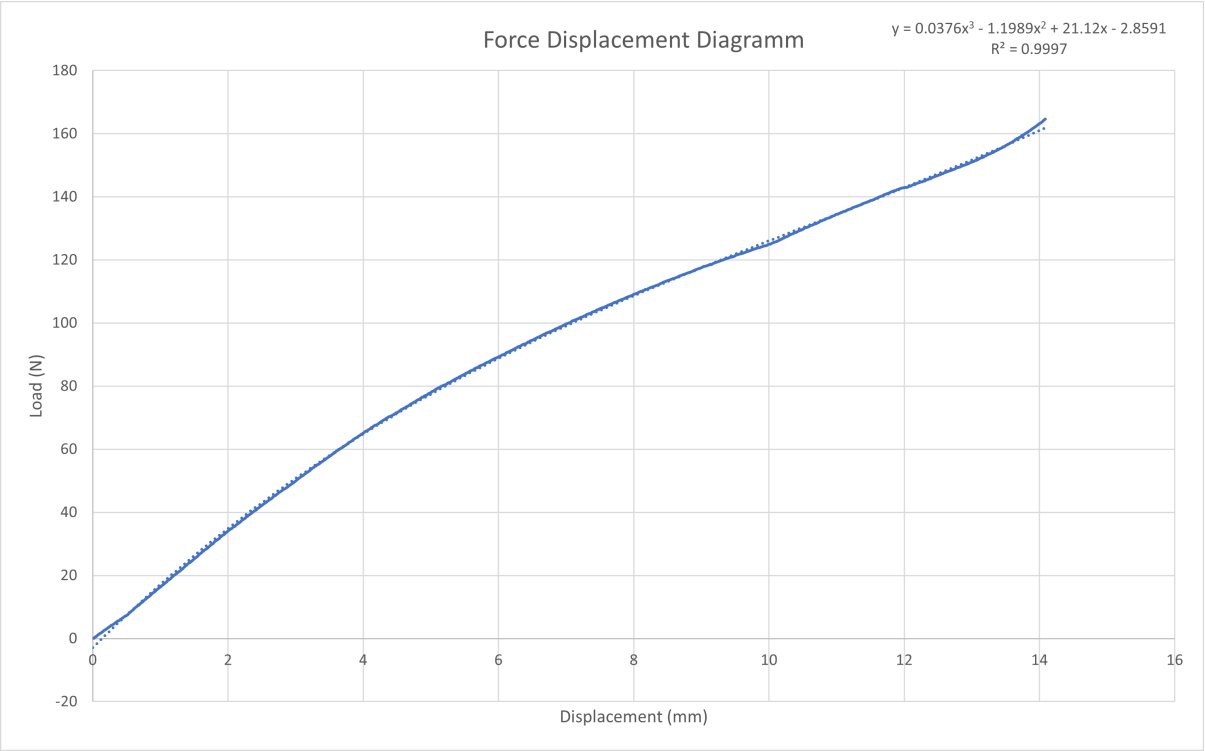


Figure 6.2: Experimentally measured force-displacement profile of the hybrid rebound mechanism. The data, obtained from a Universal Testing Machine, plots the resistive load (N) as a function of compression distance (mm). The response is observed to be largely linear with a slight, progressive stiffening at higher displacements. The effective linear stiffness (k_{eff}) is derived from the slope of the central operating region to provide a representative metric for the mechanism's stiffness, which is a critical parameter for both the system's dynamic performance and the energy input required from the user.

Comparison with Theoretical Target The experimentally measured effective stiffness of approximately 10,000 N/m is more than three orders of magnitude greater than the theoretical minimum requirement of 5 N/m calculated in Chapter 3. This result is strongly consistent with the qualitative findings of the iterative design process in Chapter 4, which concluded that a mechanism far more robust than the theoretical minimum was required to overcome real-world factors like material friction and to ensure a rapid, reliable intake stroke. The high measured stiffness confirms that the final hybrid design successfully provides the powerful rebound force identified as a critical system requirement.

Volumetric Analysis via Fluid Displacement

To determine the true physical volumes of the soft, deformable components—parameters which are difficult to derive accurately from CAD models alone—a fluid displacement test was performed. This experiment provides accurate measurements of the maximum pouch volume

(V_{max}), the effective swept volume per compression (V_{sweep}), and most critically, the real-world clearance volume (V_{cl}).

Experimental Procedure The volumetric analysis was conducted using water and a precision digital scale, where 1g of water is equivalent to 1mL of volume. The procedure was as follows:

1. The entire mechanopneumatic assembly was fully submerged in a water basin and actuated multiple times to purge all internal air.
2. A syringe was used to ensure the assembly was completely filled with water.
3. **Swept Volume Measurement:** A container on a tared precision scale was used to collect the water expelled from the pump during a single, full compression stroke. The mass of this expelled water was recorded as the swept volume, V_{sweep}.
4. **Total Volume Measurement:** Without refilling, the pump was then turned upside down over the same container and actuated repeatedly to force all remaining water out. The new total mass of water was recorded, representing the maximum pouch volume, V_{max}.



(a) Swept volume measurement (V_{sweep}). (b) Total volume measurement (V_{max}).

Figure 6.3: Experimental setup for the volumetric analysis via fluid displacement. (a) The scale measures the mass of water expelled in a single stroke (4.77 g), representing the swept volume. (b) The scale measures the total mass of water after the remaining contents are also expelled (6.23 g), representing the maximum pouch volume.

Results and Discussion The results of the fluid displacement test are shown in Figure 6.3. The mass of the water displaced in the initial stroke (V_{sweep}) was measured to be **4.77 g**, corre-

sponding to a swept volume of **4.77 ml**. The total mass of water collected after also expelling the remaining contents (V_{max}) was **6.23 g**, corresponding to a maximum volume of **6.23 mL**.

From these two direct measurements, the critical clearance volume (V_{cl}) can be calculated by subtraction:

$$V_{cl} = V_{max} - V_{sweep} = 6.23\,\text{mL} - 4.77\,\text{mL} = 1.46\,\text{mL} \tag{6.2}$$

This allows for the calculation of the pump's true clearance ratio (c):

$$c = \frac{V_{cl}}{V_{max}} = \frac{1.46\,\text{mL}}{6.23\,\text{mL}} \approx 0.234 \quad (23.4\%) \tag{6.3}$$

The measured parameters are summarized in Table 6.1. The experimentally measured clearance ratio of 23.4% is significantly higher than the initial 15% estimate used in the Chapter 3 simulation. This higher-than-expected dead volume is a critical finding and is predicted to be a primary reason for the deviation between the theoretical model's predictions and the final measured performance of the system.

Table 6.1: Comparison of Theoretical (Estimated) and Measured (Fluid Displacement) Volumetric Parameters.

Parameter	**Theoretical Estimate**	**Measured Value**
Max Pouch Volume (V_{max})	∼3.77 mL	**6.23 mL**
Clearance Ratio (c)	15.0%	**23.4%**
Derived Values:		
Clearance Volume (V_{cl})	∼0.57 mL	**1.46 mL**
Swept Volume (V_{sweep})	∼3.20 mL	**4.77 mL**

6.4 Integrated System Performance Validation

The fully assembled prototype was subjected to a series of tests with a 70 kg human subject to characterize its performance under realistic, dynamic conditions.

Thermodynamic Process Analysis: Validating the Isothermal Assumption

Experimental Setup and Procedure To accurately measure the temperature of the air displaced by the pump, a short section of copper tube was inserted into the pneumatic line. A K-type thermocouple was securely taped to the copper tube, and its leads were connected to a YATO YT-73083 digital multimeter. A human subject wore the system (Figure 6.4) and walked on a treadmill, first until the reservoir reached its stall pressure of ∼0.5 atm, and then for an additional 10 minutes (∼600 steps) at varying speeds (3-4 km/h) to ensure thermal equilibrium. The ambient room temperature was 24°C.

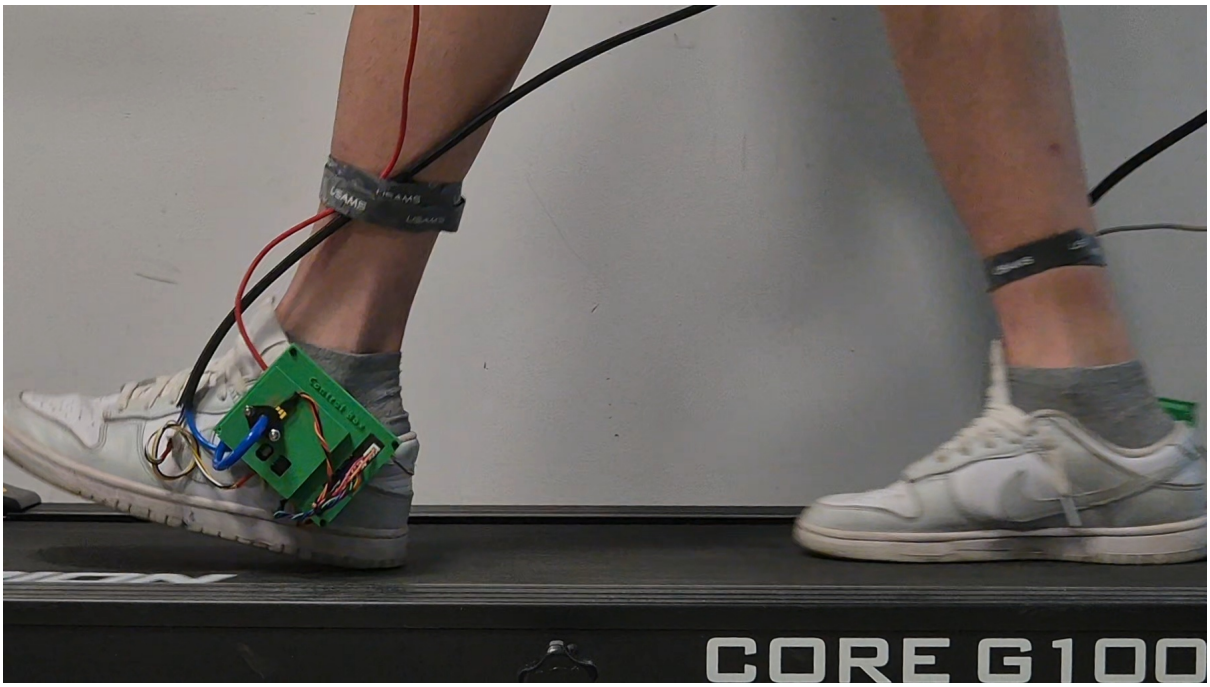


Figure 6.4: The pressure harvesting system worn by a human subject during the treadmill walking test.

Results and Conclusion During continuous operation, the temperature reading rose instantaneously from the ambient 24°C to 25°C and remained stable. This minimal, steady-state temperature increase of only 1°C corresponds to the resolution limit of the measurement instrument, indicating the actual temperature change is on this small order of magnitude. This demonstrates that heat generated during compression is rapidly dissipated. Therefore, the experimental evidence confirms that the thermodynamic process can be reasonably and accurately approximated as **isothermal**, validating the analytical approach used in Chapter 3.

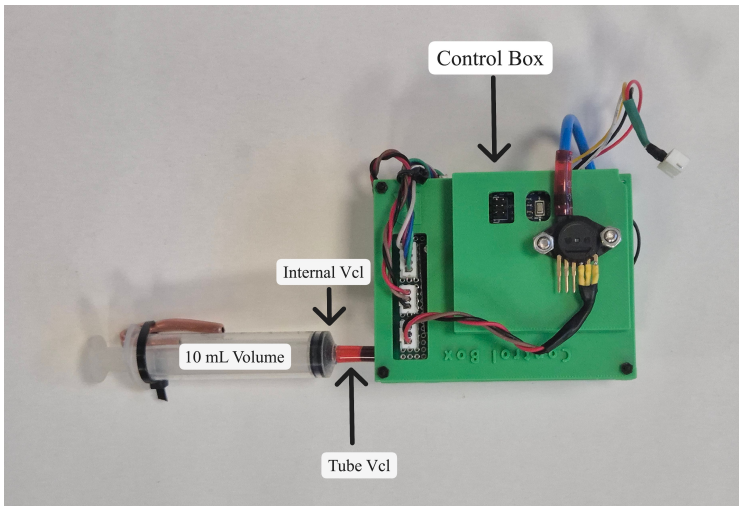
Validation of the Event-Based Analytical Model

A central performance evaluation was a direct, quantitative validation of the predictive accuracy of the event-based analytical model developed in Chapter 3. To achieve this, a controlled experiment was designed to eliminate the inherent variability of human walking. A modified 12 mL syringe, equipped with a mechanical hard stop to provide a highly consistent swept volume of exactly 10 mL, was used in place of the foot-worn textile pump. This allowed for a direct, one-to-one comparison between the model's theoretical predictions and a repeatable, real-world experiment.

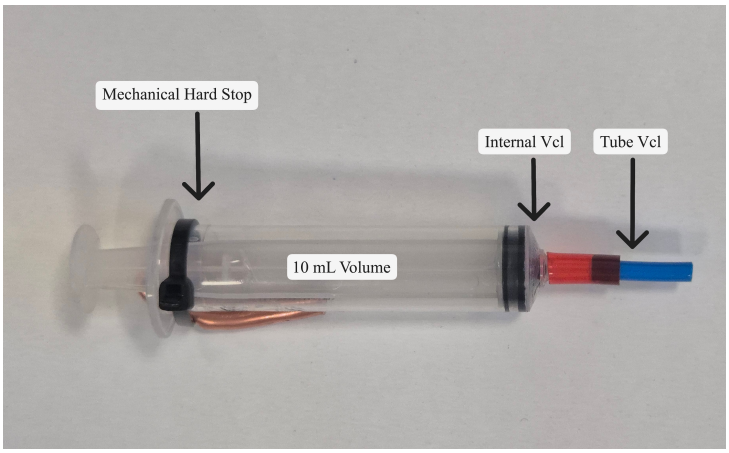
Modeling the Clearance Volume for the Validation Setup A critical step for an accurate simulation was the precise modeling of the total clearance volume (V_{cl}) of the experimental

setup. This volume was treated as the sum of two distinct components: the volume of the connecting tube and the internal residual volume of the syringe itself.

First, the volume of the pneumatic tube connecting the syringe's output to the control valve block was calculated based on its measured length and inner diameter. Second, due to the complex internal geometry of the syringe tip, its residual (clearance) volume was determined using a CAD model. The sum of these two volumes provided the total V_{cl} value used as a key input for the analytical model.



(a) Overall experimental setup.



(b) Detail of the modified syringe.

Figure 6.5: The experimental setup for the analytical model validation. (a) The modified 10 mL syringe is connected to the electropneumatic control box. The labels indicate the two components of the clearance volume (V_{cl}) that were modeled: the internal volume of the syringe tip and the volume of the connecting tube. (b) A close-up of the syringe, showing a mechanical hard stop to ensure a consistent 10 mL swept volume for each pump stroke, thereby increasing experimental repeatability.

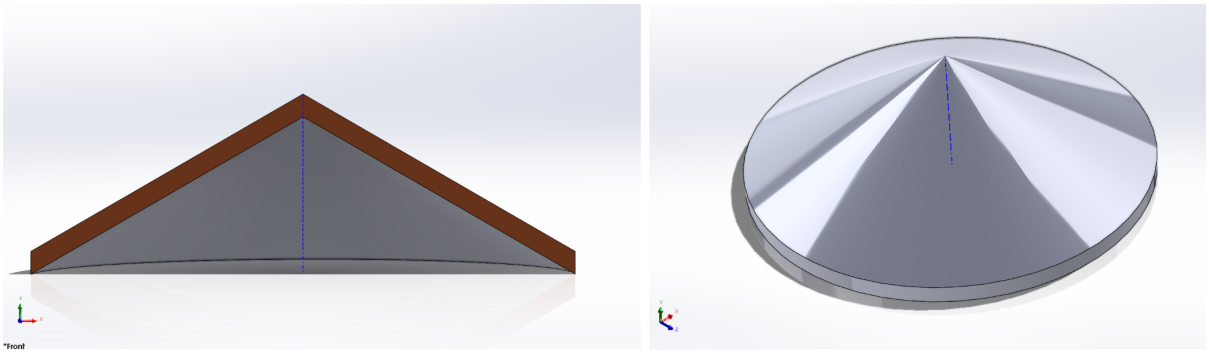
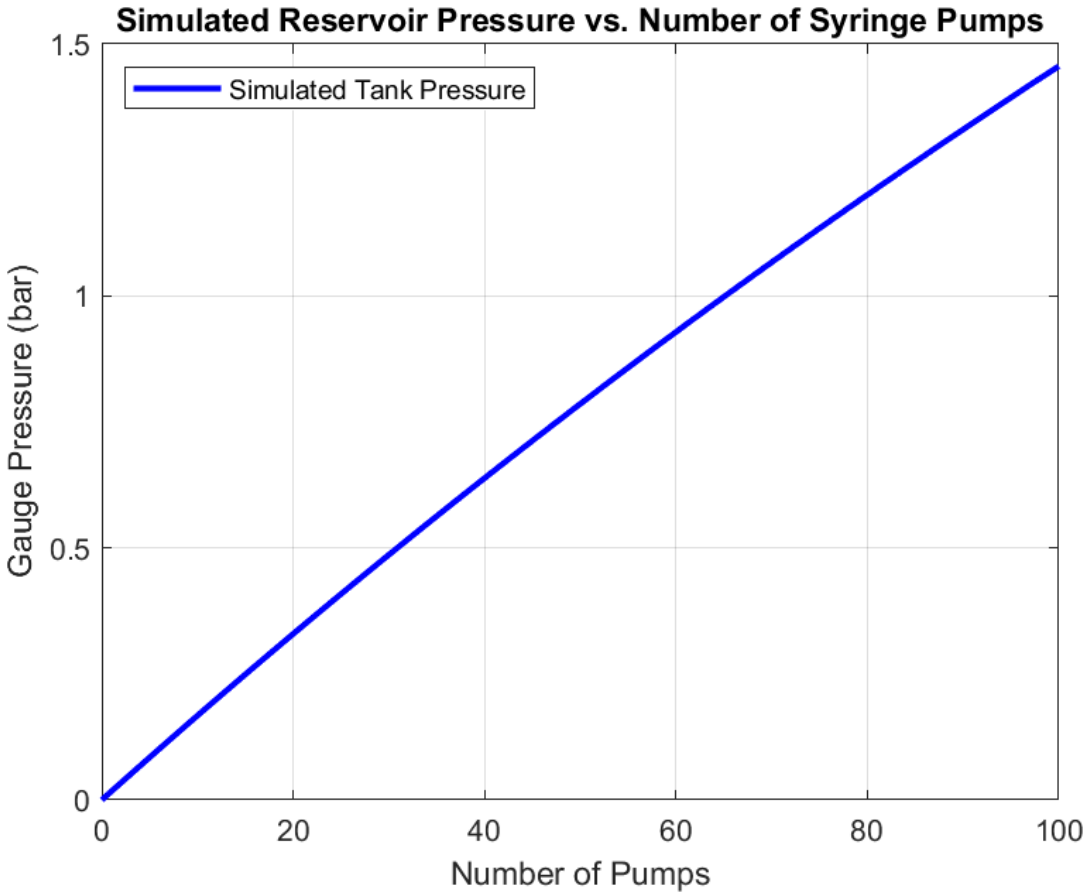


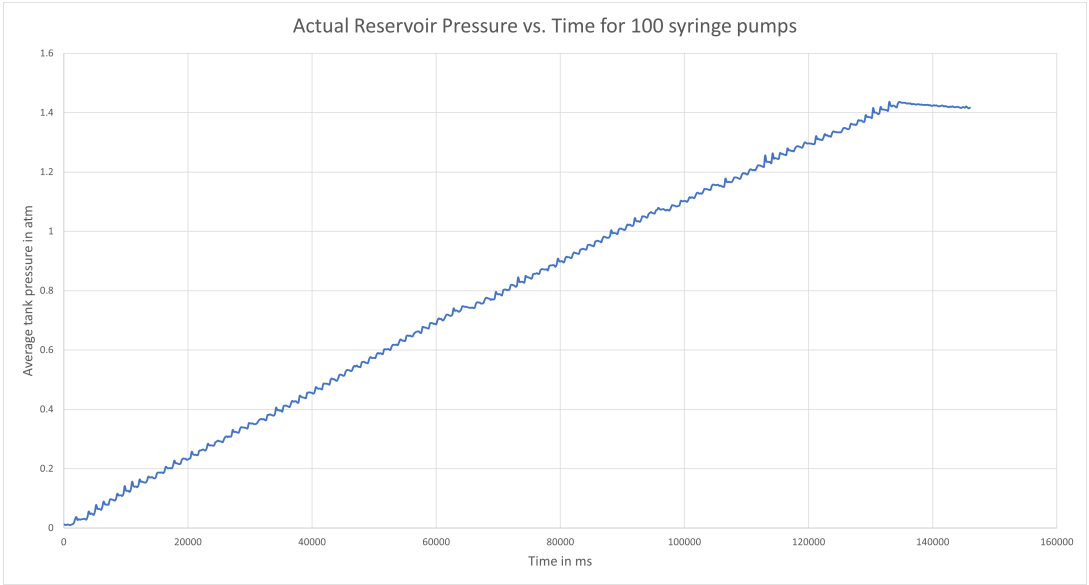
Figure 6.6: Determination of the syringe's internal clearance volume. The complex geometry of the syringe tip was modeled in CAD to accurately calculate the residual air volume when the plunger is fully depressed.

Procedure and Comparison The validation was performed in two stages. First, the analytical model was run for 100 steps, configured with the parameters of the syringe setup ($V_{pump} = 10$ mL, and the calculated total V_{cl}). Second, a physical experiment was conducted where the syringe was manually actuated for 100 full strokes, and the pressure in the 500 mL reservoir was logged after each stroke.

The results of both the simulation and the physical experiment are plotted together in Figure 6.7. The model's prediction shows very close agreement with the experimental data, accurately capturing the non-linear, diminishing rate of pressure increase. The minor divergence at higher pressures can be attributed to factors not included in the ideal model, such as microscopic air leaks in the physical setup or slight thermal effects not captured by the isothermal assumption. Overall, the strong correlation between the predicted and measured pressure curves validates the fundamental accuracy of the event-based analytical model for predicting the charging behavior of this pneumatic system.



(a) Theoretical prediction from the analytical model.



(b) Experimentally measured data from the physical test.

Figure 6.7: Direct comparison of the analytical model's prediction against the experimental results for the 100-stroke syringe test. (a) The simulation predicted a final gauge pressure of 1.46 bar. (b) The experimental test recorded a peak gauge pressure of approximately 1.42 atm (1.44 bar). The strong correlation in both the final pressure values (1.4% difference) which validates the predictive accuracy of the event-based analytical model.

Results and Conclusion The results demonstrate an exceptionally strong agreement between the theoretical model and the physical experiment. The model predicted a final pressure of **1.46 bar**, while the experiment measured a peak pressure of **1.42 atm (1.44 bar)**, a difference of only **1.4%**.

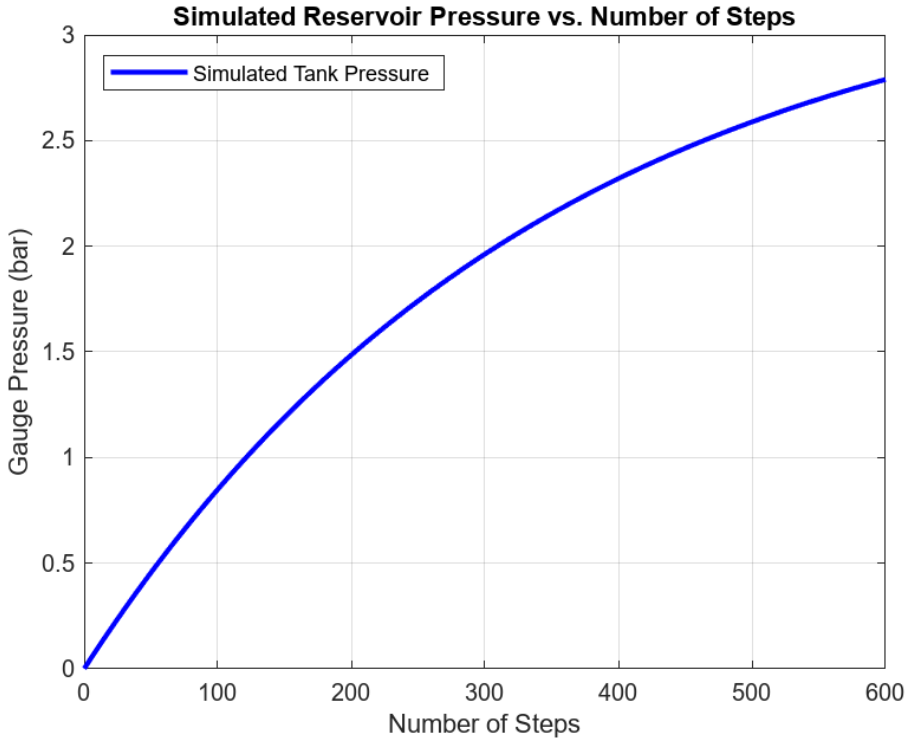
Both the simulated and experimental curves exhibit a near-linear trend, which is expected given the large ratio of tank volume to pump volume. The model accurately captures the fundamental charging dynamic of the system. This close correlation between prediction and reality provides a high degree of confidence in the validity of the analytical model developed in Chapter 3. It confirms that the model is a reliable and accurate tool for estimating the performance of this pneumatic harvesting architecture.

Dynamic Performance: Theory vs. Reality

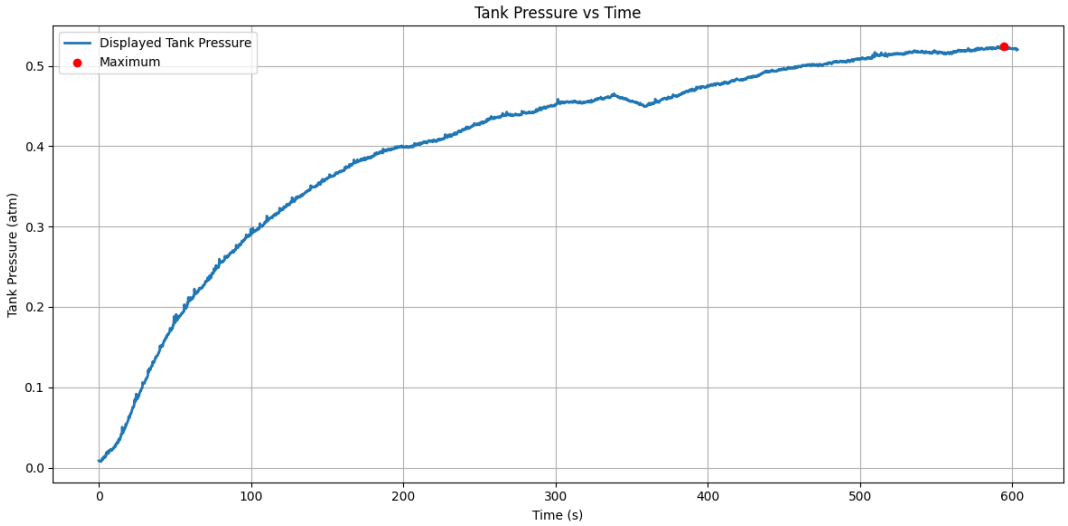
The primary performance evaluation was a direct comparison between the theoretical predictions of the analytical model and the real-world performance of the prototype.

First, the analytical model from Chapter 3 was run for 600 steps, configured with the experimentally measured parameters of the final pouch design ($V_{max} = 6.23$ mL, $c = 23.4\%$). The simulation, shown in Figure 6.8a, predicts the pressure accumulation in the tank under these specific conditions.

Next, a continuous walking test was performed to gather real-world data. A 70 kg human subject wore the full bilateral system while walking on a treadmill at a constant speed of 3 km/h. The test was concluded after exactly 600 steps, as measured by a smartwatch. The results of this 600-step test are shown in Figure 6.8b.



(a) Theoretical prediction from the analytical model for the final pouch design over 600 steps.



(b) Experimentally measured data from the 600-step treadmill test at 3 km/h.

Figure 6.8: Direct comparison of the analytical model's prediction against the real-world experimental results for a 600-step test. While the general charging behavior is similar, a significant discrepancy in the final achieved pressure is evident.

Comparison and Analysis Comparing the two plots reveals a critical finding. While the general charging behavior—a rapid initial increase followed by a plateau—is captured by both, there is a significant discrepancy in the final achieved pressure. The analytical model predicted a final gauge pressure of approximately **2.79 bar (2.75 atm)**, a value more than five times

higher than the **maximum measured gauge pressure of 0.524 atm (7.70 psi)** achieved in the physical test. This gap between theory and reality is not a failure of the model, but rather a key result that points to significant real-world inefficiencies not captured in the idealized simulation, which will be analyzed in the following section.

6.5 Synthesis and Discussion

This chapter's experimental results provide a comprehensive characterization of the system's real-world performance. The final step is to synthesize this data and compare it against the revised targets established in Chapter 4.

6.6 Data-Driven Performance Analysis and Summary

To gain a deeper insight into the system's performance, a detailed analysis was performed on the raw data from the 600-step walking test. Using the recorded tank pressure over time, the instantaneous mass flow rate ($\dot{m}$) was numerically derived. This was then used to calculate two key performance metrics: the instantaneous supply rate in Standard Liters Per Minute (SLPM) and the instantaneous power ($\dot{W} = \dot{m}RT$) based on the isothermal assumption.

This more sophisticated analysis revealed that the system's mean supply rate was not constant, but varied with the tank's back-pressure, a behavior consistent with the theoretical characteristic curve. The analysis yielded a calculated **maximum mean supply rate of 0.279 SLPM**, which occurred at a low back-pressure of 7.03 kPa. Furthermore, the analysis of the instantaneous power resulted in a calculated **average power output of 0.043 W** over the duration of the test.

These final, data-driven results are compared against the project's initial and revised goals in Table 6.2.

Table 6.2: Final comparison of project goals and experimental results.

Metric	**Initial KPI (from Ch. 1)**	**Revised Target (from Ch. 4)**	**Experimental Result (Measured)**
Max Gauge Pressure	$\geq$ 1.2 bar	$\approx$ 1.2 bar	**0.524 atm** (0.53 bar)
Insole Thickness	$\leq$ 10 mm	As wearable as possible	**22 mm** (Meets revised target)
Air Supply Rate	$\approx$ 0.36 SLPM	$\approx$ 0.36 SLPM	**0.279 SLPM** (Max Mean)
Average Power Output	Characterize	Characterize	**0.043 W** (Data-Driven Average)

Discussion

The experimental results, and particularly the significant gap between the simulated and real-world performance, provide a clear insight into the practical challenges of this technology. The analytical model assumes a perfect, idealized system. The lower performance of the physical prototype can be attributed to a combination of real-world factors, with one factor being clearly dominant.

Minor Factors Two factors contribute to the performance gap. First, **micro-leaks** in fittings and connections, while small, are inevitable under the dynamic flexing and loading of walking and would bleed off pressure over the duration of the test. Second, **inconsistent compression** due to the variability of human gait means that not every step delivers the maximum possible volume of air. This can be caused by slight variations in foot placement or by the compliant TPU housing absorbing some of the compressive force, an effect potentially amplified by the non-solid (e.g., <100%) infill used during 3D printing to facilitate rapid prototyping and cost.

The Dominant Factor: Clearance Volume The primary cause of the performance discrepancy is the **clearance ratio (c)**. As established by the analytical model, this is the single most sensitive parameter governing the maximum achievable pressure. The experimentally measured static value of **23.4%** is already very high and mathematically guarantees a low pressure ceiling. However, your analysis suggests that the *effective* dynamic clearance ratio is even higher due to several fabrication realities:

- **Inherent Dead Volume:** Even in a fully compressed state, the internal volume occupied by the fitting's nut and the anti-collapse tube segment constitutes a baseline dead volume.
- **Heat-Sealing Variability:** It is impossible to heat-seal the fabric perfectly flush against the internal components. This invariably leaves small, uncompressed air pockets.
- **Dynamic Pouch Deformation:** Under repeated cycles of inflation and compression, the fabric can deform in unpredictable ways, creating small new pockets that trap air and contribute to the effective dead volume, further increasing the clearance ratio beyond its statically measured value.

Rationale for Scope A key question arising from this analysis is why these identified issues, particularly the clearance ratio, were not fully resolved in the final prototype. The answer lies in the primary objective of this thesis. The core research goal was not to produce a perfectly optimized, high-pressure pump, but rather to **identify the core challenges and validate a viable architecture** for this technology. The successful identification of the clearance ratio as the

dominant performance-limiting factor *is* the primary scientific outcome of this experimental work. The advanced fabrication techniques and material studies required to systematically minimize this dead volume were determined to be beyond the scope of this initial investigation and are therefore presented as the most critical direction for future research in Chapter 7.

Ultimately, the prototype successfully demonstrates a functional, integrated system that validates the core harvesting concept. The direct comparison to the analytical model successfully pinpoints the key areas of inefficiency—most notably the clearance volume—providing a clear, data-driven roadmap for future optimization.

7. Conclusion and Future Work

This thesis documented the complete design, fabrication, and evaluation of a wearable, gait-powered pneumatic energy harvesting system for soft robotics. This final chapter summarizes the key findings of the work, revisits the guiding research questions to assess the project's outcomes, acknowledges the limitations of the current prototype, and proposes concrete directions for future research.

7.1 Summary of Work and Key Findings

The central challenge addressed by this thesis was the energy autonomy of wearable soft robotic devices. The core of the work was an intensive, iterative design process that led to a convergent, de-coupled mechanopneumatic architecture: a simple, high-efficiency textile pouch paired with a robust external hybrid spring. This final design was realized as a complete mechatronic system, integrating the bilateral harvesters with a custom-built electropneumatic control unit.

The key finding of this research is twofold. First, the de-coupled architecture is a viable and robust solution to the manufacturing and performance challenges that plague integrated designs. Second, the direct comparison between the analytical model and the experimental results in Chapter 6 demonstrated that the primary factor limiting the performance of the current prototype is the large effective clearance volume and other real-world inefficiencies, not a fundamental flaw in the harvesting concept itself.

7.2 Answering the Guiding Research Questions

The success of the project can be evaluated by revisiting the guiding questions posed in Chapter 1.

1. **What are the theoretical limits and practical trade-offs?** The analytical model in Chapter 3 identified the clearance ratio (c) as the primary theoretical limiter of maximum pressure. The experimental work in Chapter 6 confirmed this, showing that the measured clearance ratio of 23.4% was the key factor constraining the stall pressure.

2. **What fabrication techniques can create a durable, high-pressure seal?** Chapter 4 demonstrated that bonding FDM-printed parts to textile films was unreliable due to material porosity. The successful fabrication method, detailed in Chapter 5, relied on a single-

piece, folded pouch design made from TPU-coated fabric, which, when heat-sealed, created a monolithic and robust seam capable of withstanding over 2 bar of pressure.

3. **Can an external spring provide rebound without compromising efficiency?** Yes. The internal spring concepts (Iteration 2) failed because they created dead volume and manufacturing challenges. The final external hybrid spring provided a powerful rebound force (10,000 N/m) while leaving the compression chamber completely unobstructed, thereby maximizing volumetric efficiency as hypothesized.

4. **Can a complete bilateral system be integrated with a controller?** Yes. Chapter 5 detailed the successful integration of the two shoe-mounted harvesters with a single, belt-mounted control box. The electropneumatic system successfully regulated pressure using a feedback loop, demonstrating a complete, functional proof-of-concept.

5. **What is the real-world performance?** A data-driven analysis of the 600-step walking test quantified the system's performance: a maximum gauge pressure of **0.524 atm** and a maximum mean supply rate of **0.279 SLPM**. While the pressure did not meet the 1.2 bar KPI, the air supply rate came very close to achieving the strategic 0.36 SLPM target. The direct comparison with the analytical model in Chapter 6 proved that the performance gap was primarily due to real-world inefficiencies, most notably the high clearance ratio.

7.3 Limitations

This work represents a successful proof-of-concept, but it is important to acknowledge its limitations:

- **Performance Metrics:** The achieved pressure and flow rate are currently insufficient to power many existing soft robotic actuators, which often require >1 bar.
- **Human Factors:** All dynamic testing was conducted on a single 70 kg subject. The system's performance and comfort have not been evaluated across a diverse user population.
- **Durability:** While the pouch survived pressure testing and short-term walking, its long-term durability over thousands of gait cycles in a real-world environment (e.g., rain, dirt) has not been characterized.
- **Metabolic Cost:** The additional effort required from the user to power the system was not measured. A high metabolic cost could make the device impractical for assistive applications.

7.4 Future Work

The limitations of the current prototype, and particularly the performance gap identified in Chapter 6, provide a clear roadmap for future research.

A Pathway to High-Pressure Performance

To quantify the future potential of the de-coupled architecture, the analytical model from Chapter 3 was used to simulate a theoretically ideal pouch. This was modeled by setting the clearance ratio (c) to a near-ideal value of 1%, which corresponds to a high **compression ratio of 100:1**.

The significance of this high compression ratio is that it allows the system to theoretically approach a very high stall pressure over time. The simulation results, shown in Figure 7.1, are twofold. First, they show that on the path to this high theoretical limit, the system could achieve a gauge pressure of **7.27 bar** in just 600 steps. This represents a greater than tenfold improvement over the experimentally measured performance and far exceeds the initial 1.2 bar KPI.

Second, this 7.27 bar value is remarkably consistent with the **7.2 bar** maximum static pressure calculated for the final pouch geometry in Chapter 4. This convergence is critical: it reveals that the system's performance is governed by two distinct ceilings:

- **The Thermodynamic Ceiling:** Governed by the clearance ratio. The simulation shows that by achieving a high compression ratio (low clearance), the system is able to approach its maximum potential performance.
- **The Static Pressure Ceiling:** Governed by the fundamental relationship $P = F/A$. For the current 9.62 cm^2 pouch area and the 700 N available foot force, this ceiling is approximately 7.2 bar.

This proves that while achieving the 7 bar figure is theoretically possible by eliminating dead volume, **exceeding it would require a fundamental redesign to further decrease the pouch's cross-sectional area**.

It is also important to note that this simulation represents an idealized benchmark, as the analytical model does not account for the dead volume within the pneumatic tubing that connects the compressor to the control valves. Including this additional volume would lower the predicted pressure output. Nevertheless, this result is highly valuable. It demonstrates that the core architecture developed in this thesis is fundamentally sound and that its performance is exceptionally sensitive to both the clearance ratio and the cross-sectional area.

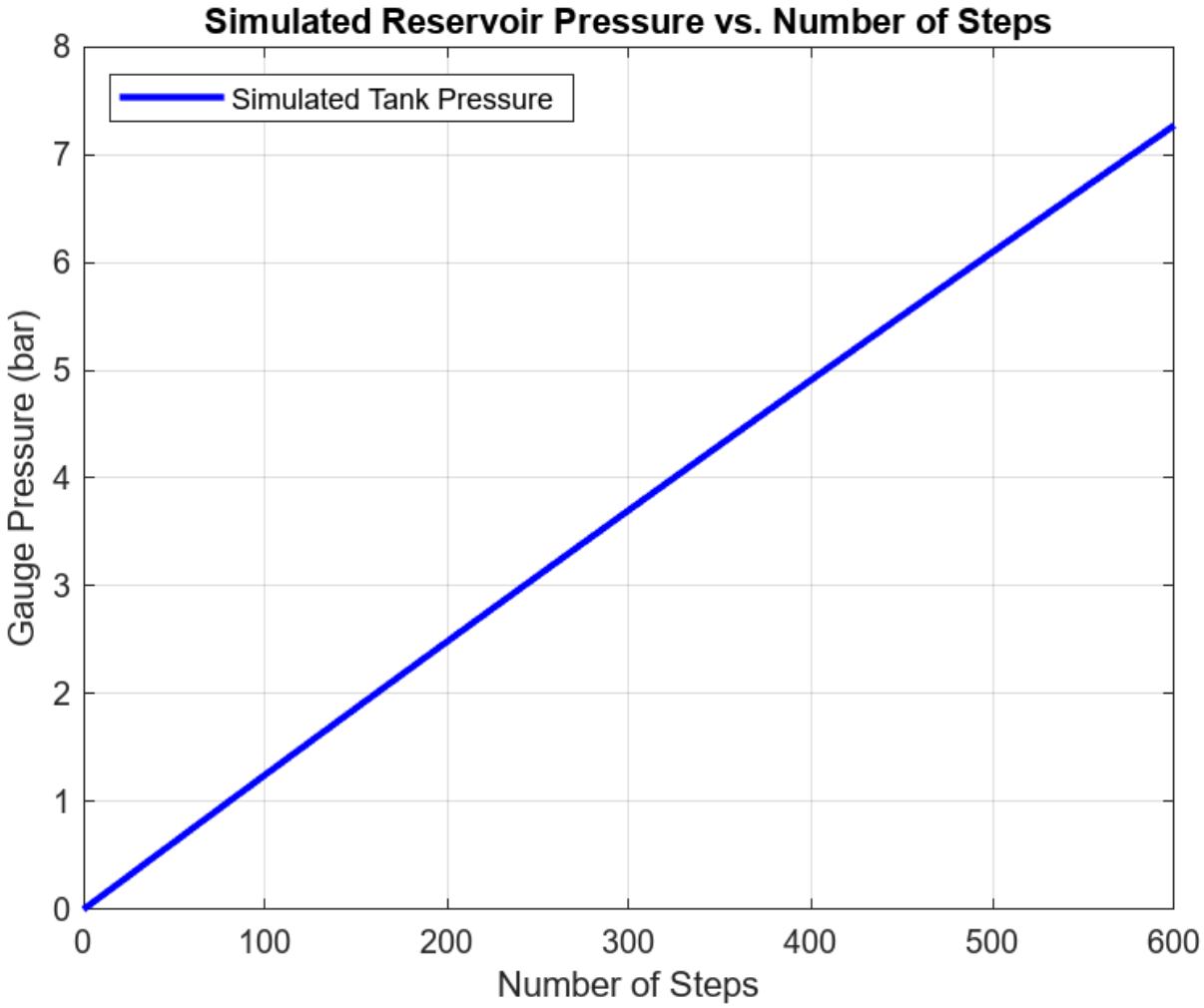


Figure 7.1: Simulated performance of a theoretically ideal pouch with a 100:1 compression ratio (1% clearance). The model predicts that the system can achieve 7.27 bar in 600 steps, a value that approaches the static pressure limit of the final pouch geometry.

Hardware Miniaturization and Integration

The current control box is a bulky prototype. Future work should focus on designing a custom Printed Circuit Board (PCB) to replace the Arduino Nano and perfboard, which would significantly reduce the size, weight, and wiring complexity of the electronics. Further integration could allow the control system to be conformally mounted on a flexible belt or integrated directly into clothing, dramatically improving user comfort and aesthetics.

Pouch Geometry Optimization

The primary performance bottleneck identified in this thesis is the clearance ratio. The most critical direction for future work is therefore to explore advanced fabrication techniques to min-

imize this dead volume, such as integrating the pneumatic fittings directly into the heat-sealed seam.

Beyond minimizing the clearance ratio, a significant avenue for optimization lies in tailoring the compressor's geometry to the user. The current design's cross-sectional area was based on a general biomechanical analysis rather than being optimized for a specific user. Future work should involve a formal optimization study to determine the ideal pouch cross-sectional area based on a user's specific mass and gait profile. This would allow the system to be tuned not just for maximum pressure, but for the maximum mass flow rate at a specific, useful target pressure, thereby maximizing the system's practical power output for a given application.

Biomechanical and Metabolic Analysis

To prove the viability of this approach for assistive technology, a formal human subjects study is required. This study should measure the metabolic cost of walking with the device, following established protocols as demonstrated by Donelan et al. [16]. Quantifying the trade-off between the energy harvested and the extra energy expended by the user is essential for determining the net benefit of the system.

Bibliography

[1] D. Rus and M. T. Tolley, "Design, fabrication and control of soft robots," *Nature*, vol. 521, pp. 467–475, 2015. DOI: 10.1038/nature14543.

[2] N. V. Divekar and R. D. Gregg, "A versatile knee exoskeleton mitigates quadriceps fatigue in lifting, lowering, and carrying tasks," *Science Robotics*, vol. 9, eadr8282, 2024. DOI: 10.1126/scirobotics.adr8282.

[3] Y. M. Zhou, C. J. Hohimer, H. T. Young, and C. J. Walsh, "A portable inflatable soft wearable robot to assist the shoulder during industrial work," *Science Robotics*, vol. 9, no. 91, eadi2377, 2024. DOI: 10.1126/scirobotics.adi2377.

[4] S. Sridar, P. H. Nguyen, M. Zhu, Q. P. Lam, and P. Polygerinos, "Development of a soft-inflatable exosuit for knee rehabilitation," in *2017 IEEE/RSJ International Conference on Intelligent Robots and Systems (IROS)*, IEEE, 2017, pp. 3722–3727. DOI: 10.1109/IROS.2017.8206220.

[5] H. Shi, Z. Liu, and X. Mei, "Overview of human walking induced energy harvesting technologies and its possibility for walking robotics," *Energies*, vol. 13, no. 1, p. 86, 2020. DOI: 10.3390/en13010086.

[6] S. Sridar, S. Poddar, Y. Tong, P. Polygerinos, and W. Zhang, "Towards untethered soft pneumatic exosuits using low-volume inflatable actuator composites and a portable pneumatic source," *IEEE Robotics and Automation Letters*, vol. 5, no. 3, pp. 4062–4069, 2020. DOI: 10.1109/LRA.2020.2986744.

[7] J. Kymissis, C. Kendall, J. Paradiso, and N. Gershenfeld, "Parasitic power harvesting in shoes," in *Second IEEE International Conference on Wearable Computing, 1998. Digest of Papers*, IEEE, 1998, pp. 132–139. DOI: 10.1109/ISWC.1998.729539.

[8] N. Haghbin, "Shoe embedded air pump type piezoelectric power harvester," M.S. thesis, Ryerson University, 2011. DOI: 10.13140/RG.2.1.3438.0649.

[9] R. A. Shveda, A. Rajappan, T. F. Yap, *et al.*, "A wearable textile-based pneumatic energy harvesting system for assistive robotics," *Science Advances*, vol. 8, no. 34, eabo2418, 2022. DOI: 10.1126/sciadv.abo2418.

[10] M. Wehner, M. T. Tolley, Y. Mengüç, *et al.*, "Pneumatic energy sources for autonomous and wearable soft robotics," *Soft Robotics*, vol. 1, no. 4, pp. 225–235, 2014. DOI: 10.1089/soro.2014.0018.

[11] R. Di Gregorio and L. Vocenas, "Identification of gait-cycle phases for prosthesis control," *Biomimetics*, vol. 6, no. 2, p. 22, 2021. DOI: 10.3390/biomimetics6020022.

[12] J. Perry and J. M. Burnfield, Eds., *Gait Analysis: Normal and Pathological Function*. Thorofare, NJ: Slack Incorporated, 2010, p. 551, ISBN: 978-1556427664. [Online]. Available: https://pmc.ncbi.nlm.nih.gov/articles/PMC3761742/.

[13] M. W. Whittle, *Gait Analysis: An Introduction*, 4th ed. Oxford: Butterworth-Heinemann, 2007, ISBN: 978-0-7506-8883-3. DOI: 10.1016/B978-0-7506-8883-3.X5001-6.

[14] N. L. W. Keijsers, "Plantar pressure analysis," *Footwear Science*, Nov. 2012. DOI: 10.1201/b13021-23.

[15] F. Horst, D. Slijepcevic, M. Simak, and W. I. Schöllhorn, "Gutenberg gait database, a ground reaction force database of level overground walking in healthy individuals," *Scientific Data*, vol. 8, no. 1, p. 232, Sep. 2021. DOI: 10.1038/s41597-021-01014-6.

[16] J. M. Donelan, Q. Li, V. Naing, J. A. Hoffer, D. J. Weber, and A. D. Kuo, "Biomechanical energy harvesting: Generating electricity during walking with minimal user effort," *Science*, vol. 319, no. 5864, pp. 807–810, 2008. DOI: 10.1126/science.1149860.

[17] I. J. Karassik, J. P. Messina, P. Cooper, and C. C. Heald, "Diaphragm pumps," in *Pump Handbook*, 4th, New York: McGraw-Hill, 2008, ch. 2.2.3, ISBN: 978-0-07-146044-6.

[18] P. R. Cavanagh, M. M. Rodgers, and A. Liboshi, "Pressure distribution under symptom-free feet during barefoot standing," *Foot & Ankle*, vol. 7, no. 5, pp. 262–278, 1987. DOI: 10.1177/107110078700700502.

[19] C.-Y. Chu and R. M. Patterson, "Soft robotic devices for hand rehabilitation and assistance: A narrative review," *Journal of NeuroEngineering and Rehabilitation*, vol. 15, no. 1, p. 9, 2018. DOI: 10.1186/s12984-018-0350-6.

[20] Y.-M. Choi, M. G. Lee, and Y. Jeon, "Wearable biomechanical energy harvesting technologies," *Energies*, vol. 10, no. 10, p. 1483, 2017. DOI: 10.3390/en10101483.

[21] R. S. Diteesawat, T. Helps, M. Taghavi, and J. Rossiter, "Electro-pneumatic pumps for soft robotics," *Science Robotics*, vol. 6, no. 51, eabc3721, 2021. DOI: 10.1126/scirobotics.abc3721.

[22] J. Y. Hayashida, "Unobtrusive integration of magnetic generator systems into common footwear," bachelorsthesis, Massachusetts Institute of Technology, Department of Mechanical Engineering, Cambridge, MA, 2000. [Online]. Available: http://hdl.handle.net/1721.1/39086.

[23] H. O. C. Houng, S. Sarah, S. Parasuraman, M. A. Khan, and I. Elamvazuthi, "Energy harvesting from human locomotion: Gait analysis, design and state of art," *Procedia Computer Science*, vol. 42, pp. 327–335, 2014. DOI: 10.1016/j.procs.2014.11.070.

[24] D. Krähenbühl, C. Zwyssig, H. Weser, and J. W. Kolar, "Theoretical and experimental results of a mesoscale electric power generation system from pressurized gas flow," *Journal of Micromechanics and Microengineering*, vol. 19, no. 9, p. 094 009, 2009. DOI: 10.1088/0960-1317/19/9/094009.

[25] P. H. Nguyen and W. Zhang, "Design and computational modeling of fabric soft pneumatic actuators for wearable assistive devices," *Scientific Reports*, vol. 10, no. 1, p. 9638, 2020. DOI: 10.1038/s41598-020-65003-2.

[26] S. Niu, X. Wang, F. Yi, Y. S. Zhou, and Z. L. Wang, "A universal self-charging system driven by random biomechanical energy for sustainable operation of mobile electronics," *Nature Communications*, vol. 6, p. 8975, 2015. DOI: 10.1038/ncomms9975.

[27] C. T. O'Neill, N. S. Phipps, L. Cappello, S. Paganoni, and C. J. Walsh, "A soft wearable robot for the shoulder: Design, characterization, and preliminary testing," in *2017 International Conference on Rehabilitation Robotics (ICORR)*, IEEE, 2017, pp. 1672–1678. DOI: 10.1109/ICORR.2017.8009488.

[28] P. Polygerinos, Z. Wang, K. C. Galloway, R. J. Wood, and C. J. Walsh, "Soft robotic glove for combined assistance and at-home rehabilitation," *Robotics and Autonomous Systems*, vol. 73, pp. 135–143, 2015. DOI: 10.1016/j.robot.2014.08.014.

[29] P. Polygerinos, N. Correll, S. A. Morin, *et al.*, "Soft robotics: Review of fluid-driven intrinsically soft devices; manufacturing, sensing, control, and applications in human-robot interaction," *Advanced Engineering Materials*, vol. 19, no. 12, p. 1 700 016, 2017. DOI: 10.1002/adem.201700016.

[30] D. J. Preston, P. Rothemund, H. J. Jiang, *et al.*, "Digital logic for soft devices," *Proceedings of the National Academy of Sciences*, vol. 116, no. 16, pp. 7750–7759, 2019. DOI: 10.1073/pnas.1820672116.

[31] V. Sanchez, C. J. Walsh, and R. J. Wood, "Textile technology for soft robotic and autonomous garments," *Advanced Functional Materials*, vol. 31, no. 31, p. 2 008 278, 2021. DOI: 10.1002/adfm.202008278.

[32] N. S. Shenck and J. A. Paradiso, "Energy scavenging with shoe-mounted piezoelectrics," *IEEE Micro*, vol. 21, no. 3, pp. 30–42, 2001. DOI: 10.1109/40.928763.

[33] T. Starner and J. A. Paradiso, "Human generated power for mobile electronics," in *Low-Power Electronics Design*, C. Piguet, Ed., CRC Press, 2003, ch. 45, ISBN: 978-0-8493-1941-9. DOI: 10.1201/9781420039559.ch45.

[34] M. Venugopal and G. Jayaramaiah, "Recent progress on bio-mechanical energy harvesting system from the human body: Comprehensive review," *(IJACSA) International Journal of Advanced Computer Science and Applications*, vol. 12, no. 7, 2021. DOI: 10.14569/IJACSA.2021.0120721.

[35] N. Wang, R. Daniels, L. Connelly, *et al.*, "All-organic flexible ferroelectret nanogenerator with fabric-based electrodes for self-powered body area networks," *Small*, vol. 17, no. 36, p. 2 103 161, 2021. DOI: 10.1002/smll.202103161.

[36] L. Xie and M. Cai, "An in-shoe harvester with motion magnification for scavenging energy from human foot strike," *IEEE/ASME Transactions on Mechatronics*, vol. 20, no. 6, pp. 3264–3272, 2015. DOI: 10.1109/TMECH.2015.2428618.

Appendix A: Source and Configuration

This appendix contains the complete Arduino firmware for the electropneumatic control subsystem. The project is managed using PlatformIO and employs a single ‘main.cpp‘ source file that is conditionally compiled into two distinct firmwares: one for the Leader (Master) controller and one for the Follower (Slave) controller. This is achieved through the use of compiler flags set in the ‘platformio.ini‘ configuration file.

PlatformIO Configuration (platformio.ini)

This configuration file defines the two build environments. The `buildflags` directive sets the `USELEFTFOOT` preprocessor macro.

```
; PlatformIO Project Configuration File
;
; This file is configured for two separate environments:
; 1. 'master_nano': For the main device that controls the display.
; 2. 'slave_nano': For the secondary device.
;
; Use the PlatformIO sidebar in VSCode to choose which environment to
; build and upload.

[platformio]
; This sets the default target for the status bar buttons (Build, Upload, etc.)
default_envs = master_nano

[env]
; This is a common section. Settings here are inherited by all environments below.
; I have copied your existing configuration here.
platform = atmelavr
board = nanoatmega328new
framework = arduino
upload_protocol = arduino
upload_speed = 115200

[env:master_nano]
; This is the environment for your MASTER (Right Foot) Nano.
; It inherits all settings from the [env] section.

; This flag tells the single main.cpp file to compile the MASTER code block.
build_flags = -D USE_LEFT_FOOT=0

; The Master is the only device that needs the display libraries.
lib_deps =
  olikraus/U8g2 @ ^2.34.22

```

```
[env:slave_nano]
; This is the environment for your SLAVE (Left Foot) Nano.
; It also inherits the common settings from [env].

; This flag tells the same main.cpp file to compile the SLAVE code block.
build_flags = -D USE_LEFT_FOOT=1

; The Slave has no extra library dependencies. It only uses the built-in
; Arduino framework (for Wire.h), so this section is intentionally blank.
lib_deps =
```

Listing 1: The `platformio.ini` file.

Shared Header File (Shared.h)

This header defines the `SystemState` enum and the `SlaveData` struct.

```
#ifndef SHARED_H
#define SHARED_H

// This enum must be identical in both firmwares. Without this, the
// compiler has no idea what 'SystemState' or 'STATE_EXHAUST' mean.
enum SystemState {
  STATE_BLOCK,
  STATE_INTAKE,
  STATE_EXHAUST
};

// This struct defines the data packet the Slave sends to the Master.
// It must contain the 'state' member for step counting to work.
struct SlaveData {
  float pumpPressure;
  float tankPressure;
  SystemState state; // Authoritative state of the slave's FSM
};

#endif
```

Listing 2: The shared header file.

Main Firmware (main.cpp)

This source file contains both Leader and Follower code. The directive `#if USELEFTFOOT == 1` selects the correct block.

```
#include <Arduino.h>
#include <Wire.h>
#include "Shared.h" // Include the shared data structure and state enum

// This flag is set in the 'platformio.ini' file by the build_flags
    directive.
// We compile the Slave code if USE_LEFT_FOOT is 1, otherwise we compile
    the Master code.
```

```
7
8  #if USE_LEFT_FOOT == 1
9  //
       ================================================================================
10 // === SLAVE FIRMWARE
       ================================================================
11 // This code is only included when compiling the 'slave_nano' environment.
12 //
       ================================================================================
13
14 // === SLAVE CONFIGURATION ===
15 #define SLAVE_ADDR 0x08
16 const float filterAlpha = 0.1f;
17 const int CALIBRATION_SAMPLES = 100, CALIBRATION_DELAY = 20;
18 const float HYSTERESIS_MARGIN = -0.05f, diffToExhaust = 0.05f;
19
20 // === PIN DEFINITIONS (Slave's wiring) ===
21 const int PumpSensor = A1, TankSensor = A0, INTAKE_PIN = 3, OUTPUT_PIN = 4;
22
23 // --- Global Variables for the Slave ---
24 float pumpPressure = 0, tankPressure = 0, atmPressure = 0;
25 float filteredPumpPressure = 0, filteredTankPressure = 0;
26 SystemState currentState = STATE_BLOCK;
27 SlaveData slaveDataToSend; // The data packet that will be sent on request
28
29 // === SLAVE-ONLY FUNCTIONS ==========================================
30 float readPumpPressureAtm()
31 {
32   int raw = analogRead(PumpSensor);
33   float psi = (raw - 188.2f) / 6.0562f;
34   return psi / 14.696f;
35 }
36 float readTankPressureAtm()
37 {
38   int raw = analogRead(TankSensor);
39   float psi = (raw - 167.71f) / 9.9562f;
40   return psi / 14.696f;
41 }
42
43 void calibrateSensors()
44 {
45   for (int i = 0; i < CALIBRATION_SAMPLES; i++)
46   {
47     float rp = readPumpPressureAtm(), rt = readTankPressureAtm();
48     if (i == 0)
49     {
50       filteredPumpPressure = rp;
51       filteredTankPressure = rt;
52     }
53     else
54     {
55       filteredPumpPressure += filterAlpha * (rp - filteredPumpPressure);
56       filteredTankPressure += filterAlpha * (rt - filteredTankPressure);
57     }
```

```
    delay(CALIBRATION_DELAY);
  }
  atmPressure = filteredPumpPressure;
}

void updateState()
{
  float diff = pumpPressure - tankPressure;
  SystemState newState = currentState;
  if (diff > diffToExhaust)
    newState = STATE_EXHAUST;
  else if (pumpPressure < atmPressure + HYSTERESIS_MARGIN)
    newState = STATE_INTAKE;
  else
    newState = STATE_BLOCK;
  if (newState != currentState)
    currentState = newState;
}

void executeState()
{
  switch (currentState)
  {
  case STATE_EXHAUST:
    digitalWrite(INTAKE_PIN, LOW);
    digitalWrite(OUTPUT_PIN, HIGH);
    break;
  case STATE_INTAKE:
    digitalWrite(INTAKE_PIN, HIGH);
    digitalWrite(OUTPUT_PIN, LOW);
    break;
  default:
    digitalWrite(INTAKE_PIN, LOW);
    digitalWrite(OUTPUT_PIN, LOW);
    break;
  }
}

// --- I2C Interrupt Service Routine ---
void onRequestEvent()
{
  slaveDataToSend.pumpPressure = pumpPressure;
  slaveDataToSend.tankPressure = tankPressure;
  slaveDataToSend.state = currentState; // Populate the packet with the
      current state
  Wire.write((uint8_t *)&slaveDataToSend, sizeof(slaveDataToSend));
}

void setup()
{
  pinMode(INTAKE_PIN, OUTPUT);
  pinMode(OUTPUT_PIN, OUTPUT);
  digitalWrite(INTAKE_PIN, LOW);
  digitalWrite(OUTPUT_PIN, LOW);
  digitalWrite(INTAKE_PIN, HIGH);
  calibrateSensors();
```

```
113   digitalWrite(INTAKE_PIN, LOW);
114   Wire.begin(SLAVE_ADDR);
115   Wire.onRequest(onRequestEvent);
116 }
117
118 void loop()
119 {
120   float rawPumpPressure = readPumpPressureAtm();
121   float rawTankPressure = readTankPressureAtm();
122   filteredPumpPressure += filterAlpha * (rawPumpPressure -
        filteredPumpPressure);
123   filteredTankPressure += filterAlpha * (rawTankPressure -
        filteredTankPressure);
124   pumpPressure = filteredPumpPressure;
125   tankPressure = filteredTankPressure;
126   updateState();
127   executeState();
128 }
129
130 #else
131 //
      ============================================================================

132 // === MASTER FIRMWARE
      ============================================================
133 // This code is only included when compiling the 'master_nano' environment.
134 //
      ============================================================================

135 #include <U8g2lib.h>
136
137 // === MASTER CONFIGURATION ===
138 #define SLAVE_ADDR 0x08
139 #define DEBUG_LEVEL 1
140 const unsigned long SLOW_TASK_INTERVAL_MS = 200;
141 const float MAX_PRESSURE_ATM = 2.0f;
142 const float filterAlpha = 0.1f, HYSTERESIS_MARGIN = -0.05f, diffToExhaust =
      0.05f;
143 const int CALIBRATION_SAMPLES = 100, CALIBRATION_DELAY = 20;
144
145 // === PIN DEFINITIONS (Master's wiring) ===
146 const int PumpSensor = A1, TankSensor = A0, INTAKE_PIN = 3, OUTPUT_PIN = 4;
147
148 // --- Global Variables for the Master ---
149 U8G2_SH1106_128X64_NONAME_F_HW_I2C u8g2(U8G2_R0, U8X8_PIN_NONE);
150 static unsigned long lastSlowTaskMillis = 0;
151 float pumpPressure = 0, tankPressure = 0, atmPressure = 0;
152 float filteredPumpPressure = 0, filteredTankPressure = 0;
153 SystemState currentState = STATE_BLOCK;
154 SlaveData receivedSlaveData; // Struct to hold data from the slave
155 unsigned long programStartTime = 0;
156 unsigned int masterStepCount = 0, slaveStepCount = 0;
157 SystemState previousMasterState = STATE_BLOCK, previousSlaveState =
      STATE_BLOCK;
158 float display_rPump = 0.0f, display_lPump = 0.0f, display_avgTank = 0.0f,
      display_spm = 0.0f;
```

```
159 const float SMOOTHING_FACTOR = 0.5f;
160
161 // === MASTER-ONLY FUNCTIONS ========================================
162 float readPumpPressureAtm()
163 {
164   int raw = analogRead(PumpSensor);
165   float psi = (raw - 184.03f) / 5.6447f;
166   return psi / 14.696f;
167 }
168 float readTankPressureAtm()
169 {
170   int raw = analogRead(TankSensor);
171   float psi = (raw - 171.03f) / 9.8774f;
172   return psi / 14.696f;
173 }
174 void calibrateSensors()
175 { /* Identical to slave's, but uses master's read... funcs */
176   for (int i = 0; i < CALIBRATION_SAMPLES; i++)
177   {
178     float rp = readPumpPressureAtm(), rt = readTankPressureAtm();
179     if (i == 0)
180     {
181       filteredPumpPressure = rp;
182       filteredTankPressure = rt;
183     }
184     else
185     {
186       filteredPumpPressure += filterAlpha * (rp - filteredPumpPressure);
187       filteredTankPressure += filterAlpha * (rt - filteredTankPressure);
188     }
189     delay(CALIBRATION_DELAY);
190   }
191   atmPressure = filteredPumpPressure;
192 }
193 void updateState()
194 { /* Identical to slave's, but uses master's vars */
195   float diff = pumpPressure - tankPressure;
196   SystemState newState = currentState;
197   if (diff > diffToExhaust)
198     newState = STATE_EXHAUST;
199   else if (pumpPressure < atmPressure + HYSTERESIS_MARGIN)
200     newState = STATE_INTAKE;
201   else
202     newState = STATE_BLOCK;
203   if (newState != currentState)
204     currentState = newState;
205 }
206 void executeState()
207 { /* Identical to slave's, but uses master's vars */
208   switch (currentState)
209   {
210   case STATE_EXHAUST:
211     digitalWrite(INTAKE_PIN, LOW);
212     digitalWrite(OUTPUT_PIN, HIGH);
213     break;
214   case STATE_INTAKE:
```

```
215     digitalWrite(INTAKE_PIN, HIGH);
216     digitalWrite(OUTPUT_PIN, LOW);
217     break;
218   default:
219     digitalWrite(INTAKE_PIN, LOW);
220     digitalWrite(OUTPUT_PIN, LOW);
221     break;
222   }
223 }
224 void checkForMasterStep()
225 {
226   if (currentState == STATE_EXHAUST && previousMasterState != STATE_EXHAUST
        )
227     masterStepCount++;
228   previousMasterState = currentState;
229 }
230 void checkForSlaveStep()
231 {
232   if (receivedSlaveData.state == STATE_EXHAUST && previousSlaveState !=
        STATE_EXHAUST)
233     slaveStepCount++;
234   previousSlaveState = receivedSlaveData.state;
235 }
236 void drawOledScreen(float rPump, float lPump, float avgTank, unsigned int
      steps, float time, float rate)
237 {
238   u8g2.clearBuffer();
239   char buffer[16];
240   const int barY = 12, barHeight = 42, textY = 62, barWidth = 28;
241   const int leftBarX = 2, tankBarX = 35, rightBarX = 68, infoX = 100;
242   u8g2.setFont(u8g2_font_6x10_tr);
243   u8g2.drawStr(leftBarX, 10, "Left");
244   u8g2.drawStr(tankBarX, 10, "Tank");
245   u8g2.drawStr(rightBarX, 10, "Right");
246   float lFill = constrain(lPump / MAX_PRESSURE_ATM, 0.0, 1.0);
247   u8g2.drawFrame(leftBarX, barY, barWidth, barHeight);
248   u8g2.drawBox(leftBarX, barY + barHeight - (lFill * barHeight), barWidth,
        lFill * barHeight);
249   dtostrf(lPump, 4, 2, buffer);
250   u8g2.drawStr(leftBarX, textY, buffer);
251   float rFill = constrain(rPump / MAX_PRESSURE_ATM, 0.0, 1.0);
252   u8g2.drawFrame(rightBarX, barY, barWidth, barHeight);
253   u8g2.drawBox(rightBarX, barY + barHeight - (rFill * barHeight), barWidth,
        rFill * barHeight);
254   dtostrf(rPump, 4, 2, buffer);
255   u8g2.drawStr(rightBarX, textY, buffer);
256   float tFill = constrain(avgTank / MAX_PRESSURE_ATM, 0.0, 1.0);
257   u8g2.drawFrame(tankBarX, barY, barWidth, barHeight);
258   u8g2.drawBox(tankBarX, barY + barHeight - (tFill * barHeight), barWidth,
        tFill * barHeight);
259   sprintf(buffer, "%d%%", (int)(tFill * 100));
260   u8g2.drawStr(tankBarX + 2, textY, buffer);
261   u8g2.setFont(u8g2_font_5x7_tr);
262   u8g2.drawStr(infoX, 10, "Time");
263   dtostrf(time, 4, 0, buffer);
264   strcat(buffer, "s");
```

```
265   u8g2.drawStr(infoX, 20, buffer);
266   u8g2.drawStr(infoX, 32, "Steps");
267   sprintf(buffer, "%d", steps);
268   u8g2.drawStr(infoX, 42, buffer);
269   u8g2.drawStr(infoX, 54, "SPM");
270   dtostrf(rate, 3, 0, buffer);
271   u8g2.drawStr(infoX, 64, buffer);
272   u8g2.sendBuffer();
273 }
274
275 void setup()
276 {
277   Serial.begin(9600);
278   pinMode(INTAKE_PIN, OUTPUT);
279   pinMode(OUTPUT_PIN, OUTPUT);
280   digitalWrite(INTAKE_PIN, LOW);
281   digitalWrite(OUTPUT_PIN, LOW);
282   if (DEBUG_LEVEL >= 1)
283     Serial.begin(9600);
284   Wire.begin();
285   u8g2.begin();
286   programStartTime = millis();
287   digitalWrite(INTAKE_PIN, HIGH);
288   calibrateSensors();
289   digitalWrite(INTAKE_PIN, LOW);
290 }
291
292 void loop()
293 {
294   // --- MASTER'S CRITICAL PATH ---
295   float rawPumpPressure = readPumpPressureAtm();
296   float rawTankPressure = readTankPressureAtm();
297   filteredPumpPressure += filterAlpha * (rawPumpPressure -
        filteredPumpPressure);
298   filteredTankPressure += filterAlpha * (rawTankPressure -
        filteredTankPressure);
299   pumpPressure = filteredPumpPressure;
300   tankPressure = filteredTankPressure;
301   updateState();
302   executeState();
303   checkForMasterStep();
304
305   // --- NON-CRITICAL I/O & DISPLAY LOOP ---
306   unsigned long now = millis();
307   if (now - lastSlowTaskMillis >= SLOW_TASK_INTERVAL_MS)
308   {
309     lastSlowTaskMillis = now;
310     Wire.requestFrom((uint8_t)SLAVE_ADDR, sizeof(receivedSlaveData));
311     if (Wire.available() == sizeof(receivedSlaveData))
312     {
313       Wire.readBytes((uint8_t *)&receivedSlaveData, sizeof(
            receivedSlaveData));
314     }
315     checkForSlaveStep();
316     unsigned int totalSteps = masterStepCount + slaveStepCount;
317     float elapsedTimeSec = (now - programStartTime) / 1000.0f;
```

```
318     float stepsPerMinute = (elapsedTimeSec > 1) ? (totalSteps / (
            elapsedTimeSec / 60.0f)) : 0;
319     float avgTankPressure = (tankPressure + receivedSlaveData.tankPressure)
             / 2.0f;
320     display_rPump += (pumpPressure - display_rPump) * SMOOTHING_FACTOR;
321     display_lPump += (receivedSlaveData.pumpPressure - display_lPump) *
            SMOOTHING_FACTOR;
322     display_avgTank += (avgTankPressure - display_avgTank) *
            SMOOTHING_FACTOR;
323     display_spm += (stepsPerMinute - display_spm) * SMOOTHING_FACTOR;
324     drawOledScreen(display_rPump, display_lPump, display_avgTank,
            totalSteps, elapsedTimeSec, display_spm);
325     // === TIERED DEBUGGING BLOCK (Replaces the old debug print) ===
326     if (DEBUG_LEVEL == 1)
327     {
328       // Level 1: CSV format for data logging and plotting.
329       // Format: time,master_pump,master_tank,slave_pump,slave_tank
330       Serial.print(now);
331       Serial.print(",");
332       Serial.print(pumpPressure, 4); // Using 4 decimal places for better
              resolution in logs
333       Serial.print(",");
334       Serial.print(tankPressure, 4);
335       Serial.print(",");
336       Serial.print(receivedSlaveData.pumpPressure, 4);
337       Serial.print(",");
338       Serial.println(receivedSlaveData.tankPressure, 4);
339     }
340     else if (DEBUG_LEVEL >= 2)
341     {
342       // Level 2: Verbose, human-readable format for "everything".
343       Serial.print("Time: ");
344       Serial.print(now);
345       Serial.print(" | M(P/T): ");
346       Serial.print(pumpPressure, 2);
347       Serial.print("/");
348       Serial.print(tankPressure, 2);
349       Serial.print(" | S(P/T): ");
350       Serial.print(receivedSlaveData.pumpPressure, 2);
351       Serial.print("/");
352       Serial.print(receivedSlaveData.tankPressure, 2);
353       Serial.print(" | Steps(M/S): ");
354       Serial.print(masterStepCount);
355       Serial.print("/");
356       Serial.print(slaveStepCount);
357       Serial.print(" | SPM: ");
358       Serial.println((int)stepsPerMinute);
359     }
360     // If DEBUG_LEVEL is 0, neither of these blocks will execute.  }
361   }
362 }
363
364 #endif // End of #if USE_LEFT_FOOT
```

Listing 3: The complete firmware.

Appendix B: Key CAD Designs

This appendix contains key 2D technical drawings for the custom-fabricated components developed and discussed in this thesis. All dimensions are in millimeters unless otherwise noted.

Iterative Prototype Designs (Chapter 4)

Iteration 2: Internal Spring Concept

These drawings detail the components for the second major design iteration, which featured an integrated, 3D-printed spring.

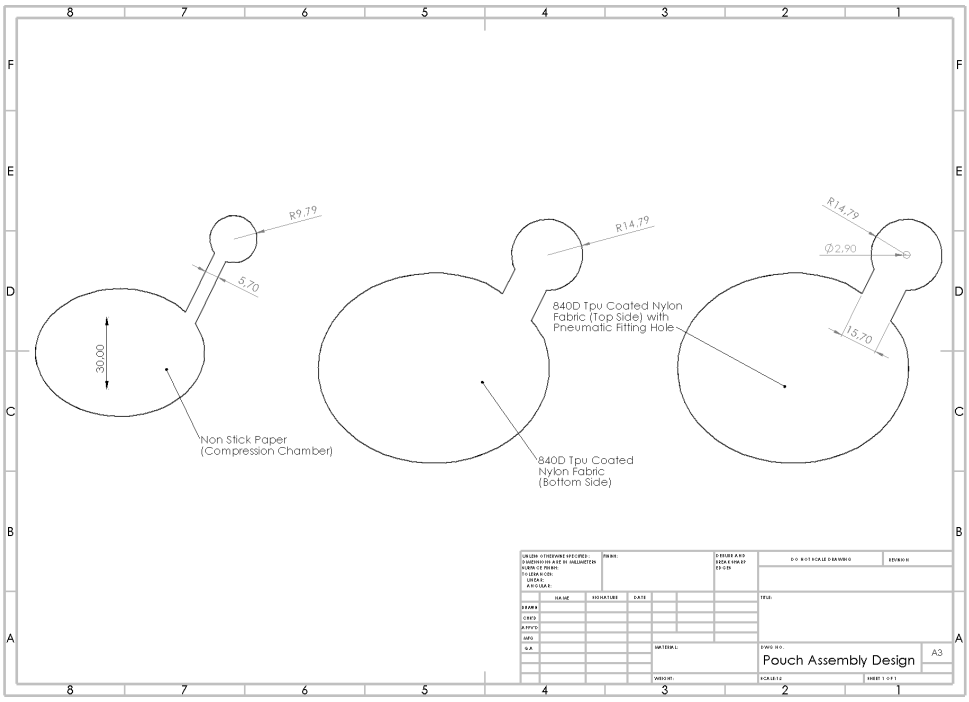


Figure 1: Technical drawing of the pouch assembly pattern for the Iteration 2 prototype.

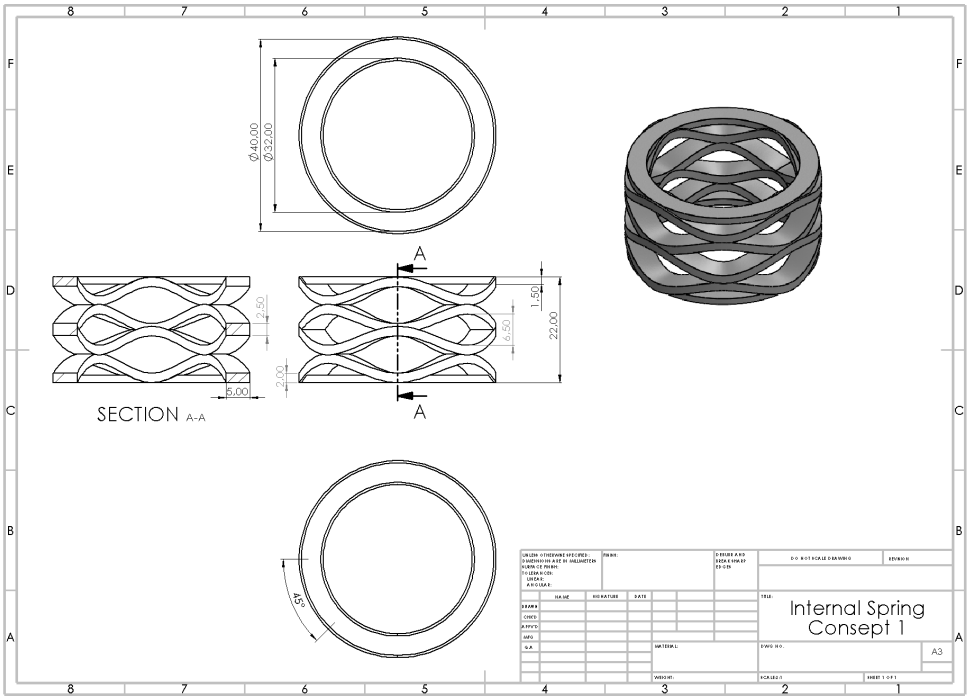


Figure 2: Technical drawing of the internal spring concept, variant 1.

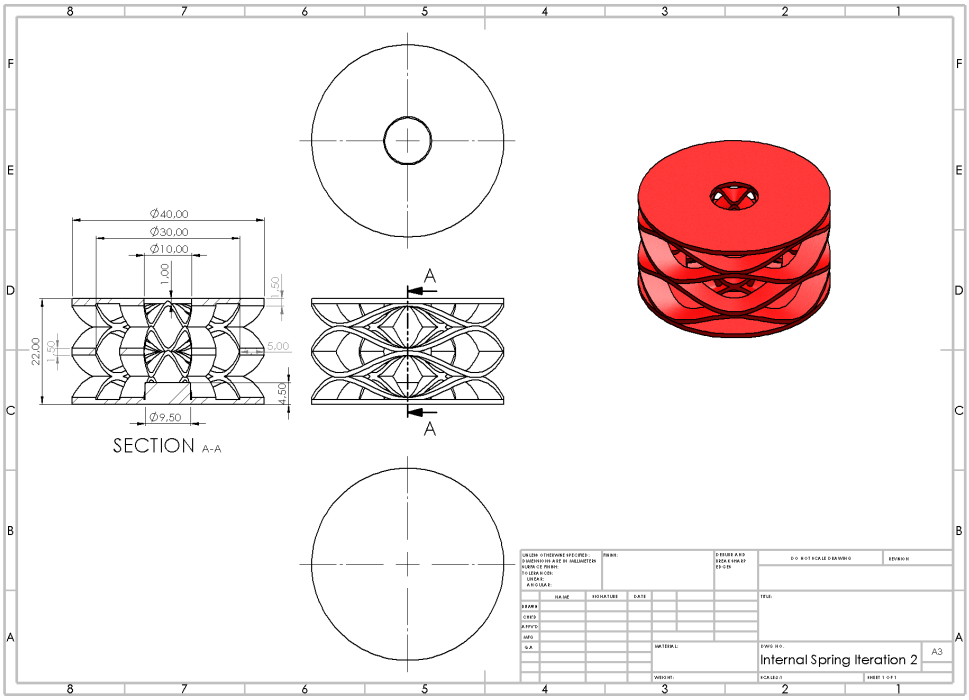


Figure 3: Technical drawing of the internal spring concept, variant 2.

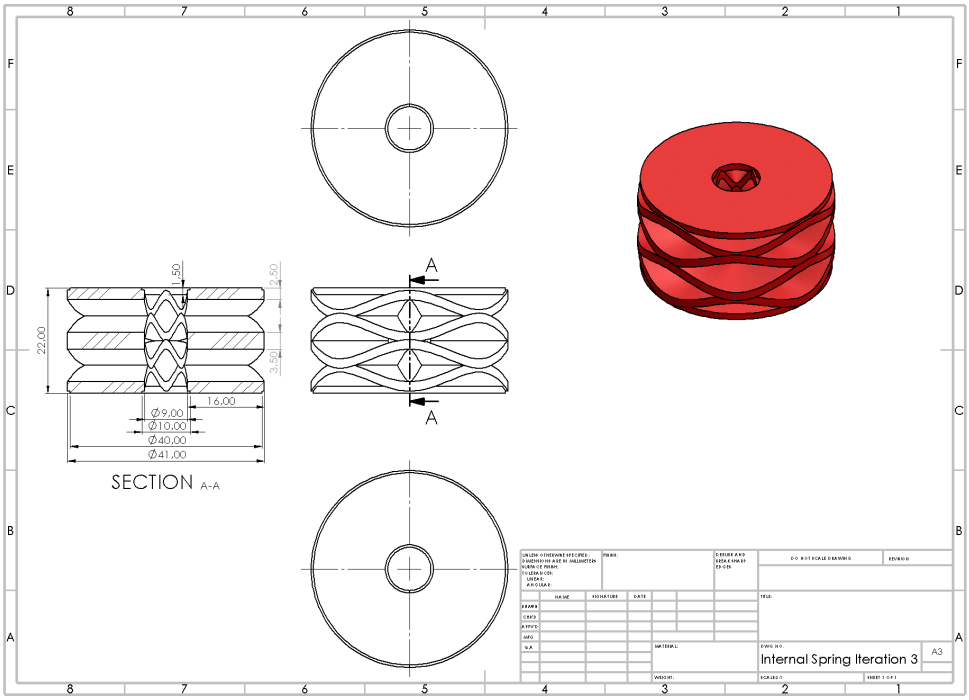


Figure 4: Technical drawing of the internal spring concept, variant 3.

Iteration 3: Structured Pouch Concept

These drawings detail the components for the third major design iteration, which featured a 3D-printed structural frame.

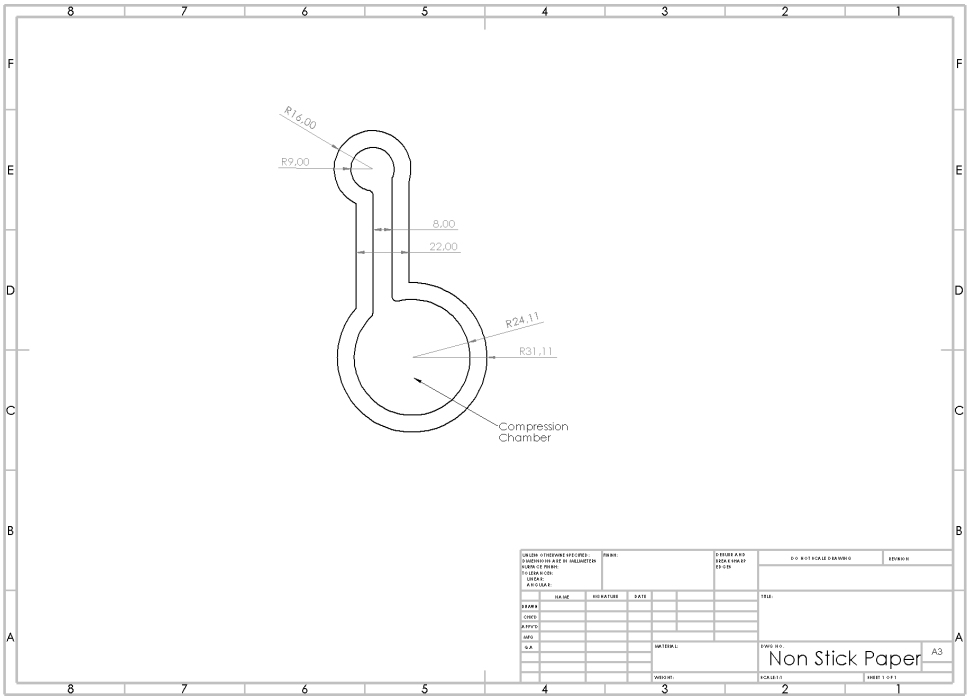


Figure 5: Technical drawing of the pouch pattern for the Iteration 3 prototype.

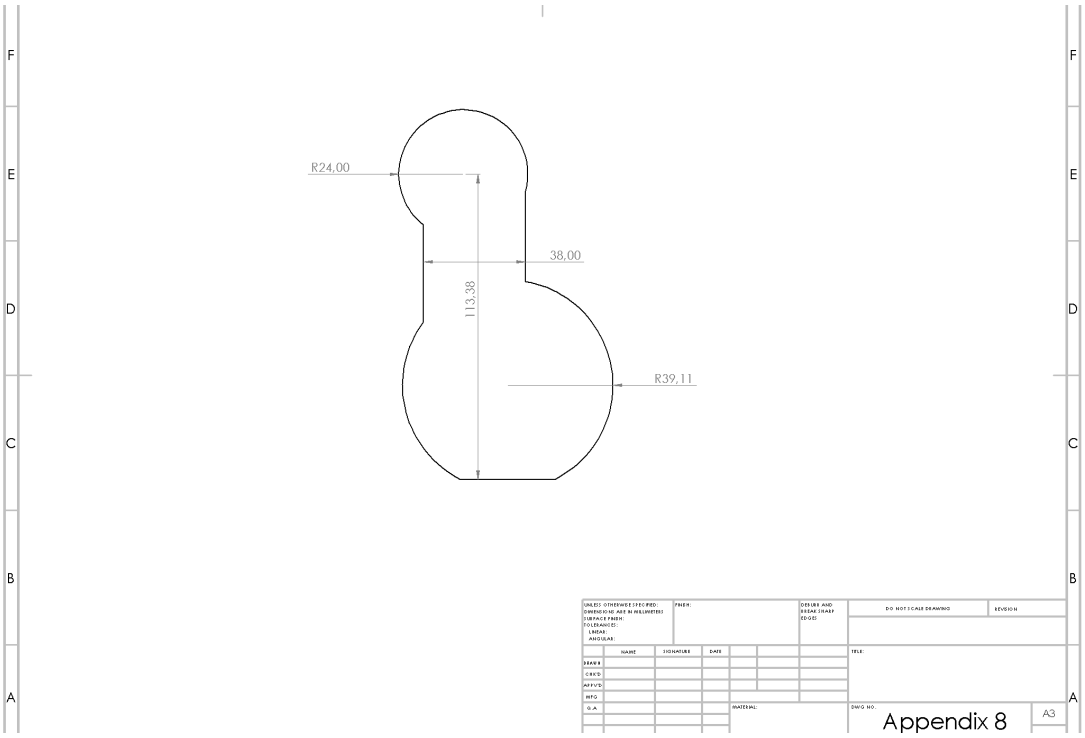


Figure 6: Technical drawing of the TPU Fabric for Iteration 3.

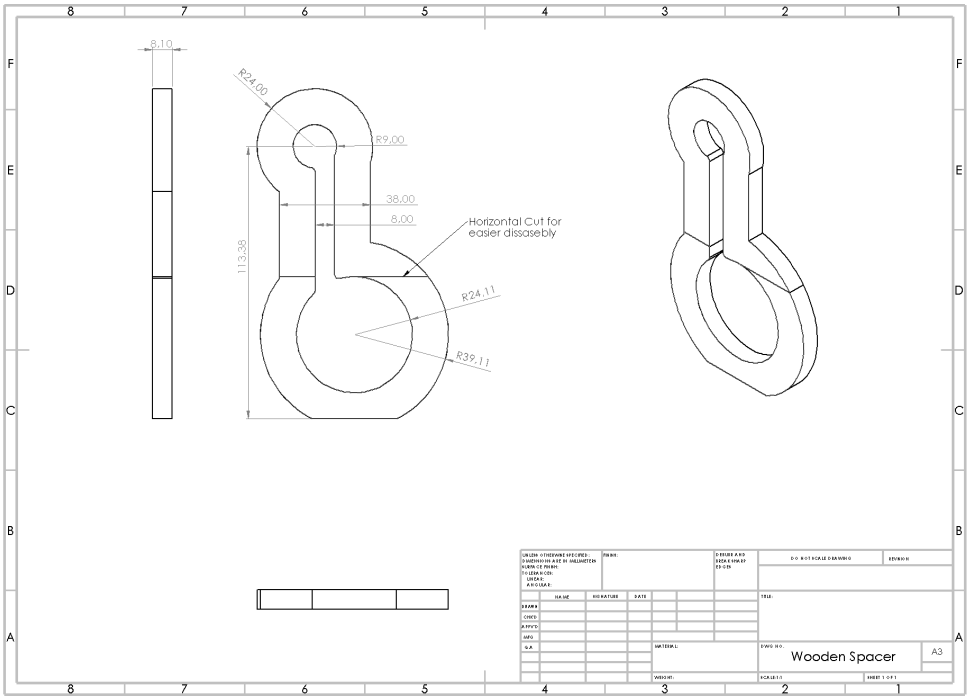


Figure 7: Technical drawing of the wooden jig used for fabrication in Iteration 3.

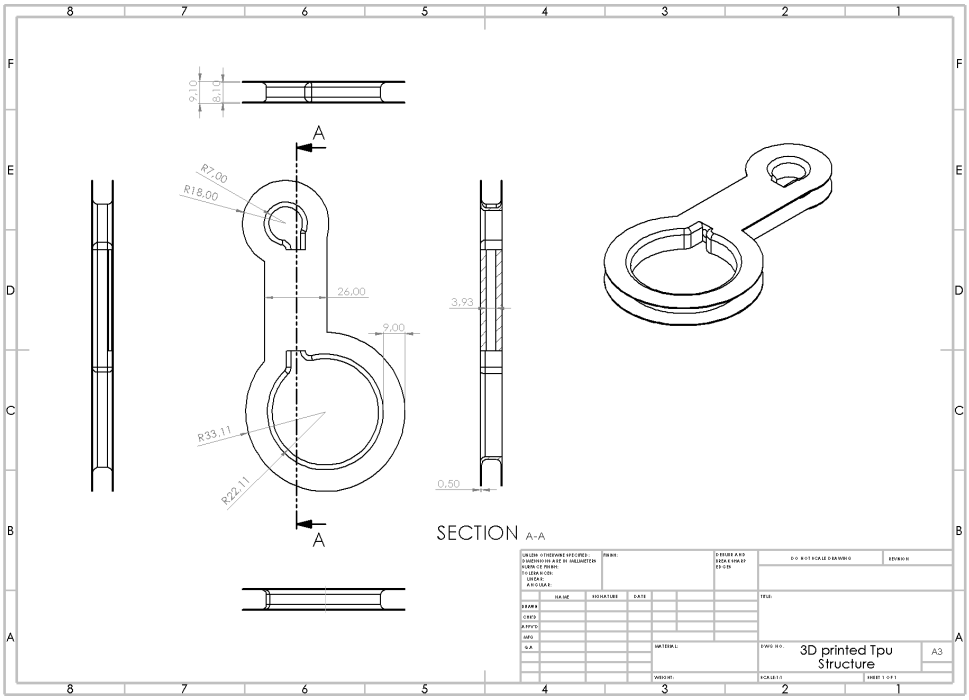


Figure 8: Technical drawing of the 3D-printed TPU structural frame for Iteration 3.

Final Convergent Design (Chapter 5)

Mechanopneumatic Subsystem

These drawings detail the final, successful components of the mechanopneumatic harvester.

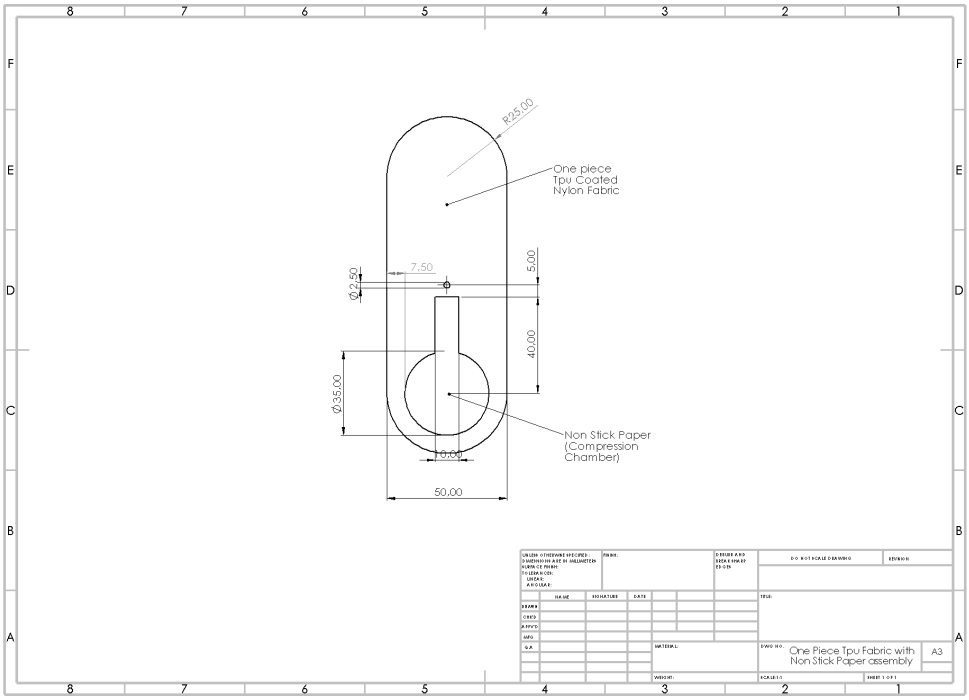


Figure 9: Technical drawing of the one-piece folded pattern for the final compressor pouch.

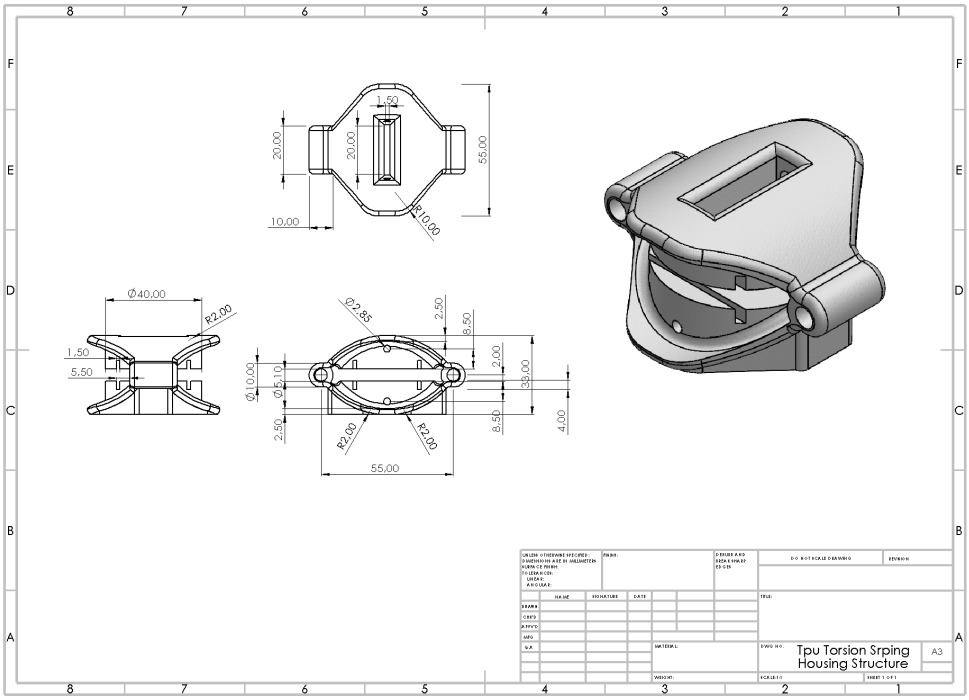


Figure 10: Technical drawing of the 3D-printed TPU housing for the de-coupled hybrid spring mechanism.

Enclosures and Assembly

These drawings detail the custom enclosures and the final assembly of the electropneumatic control box.

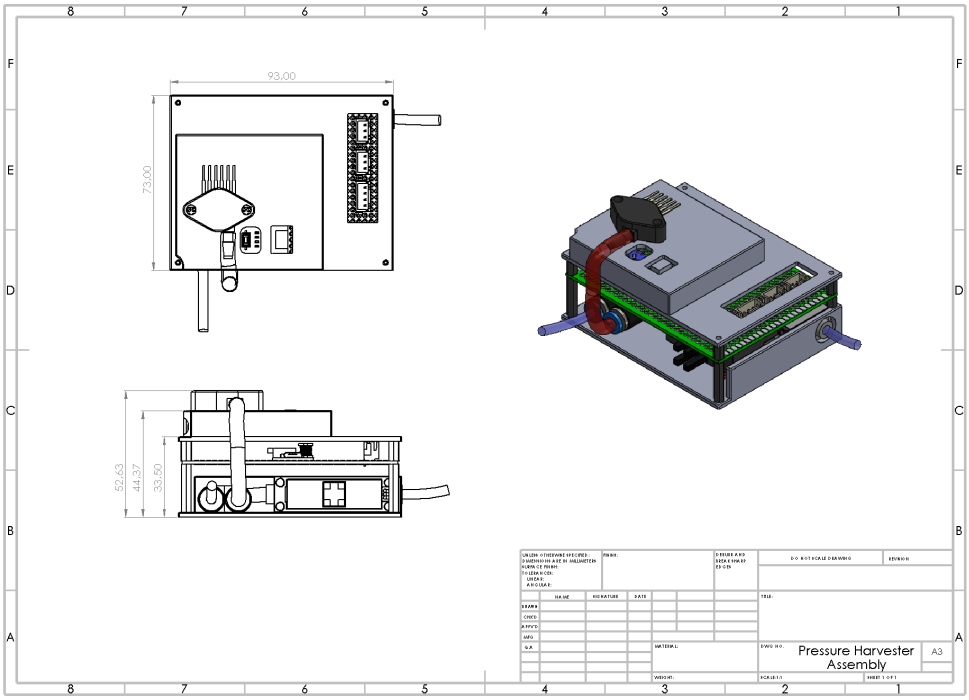


Figure 11: Technical drawing of the complete electropneumatic control box assembly.

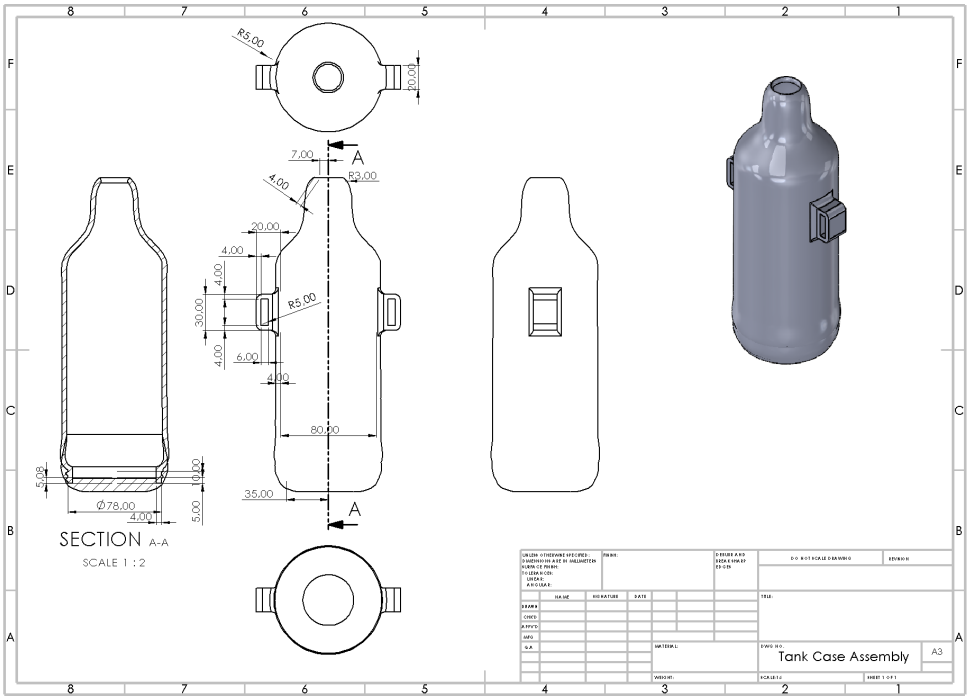


Figure 12: Technical drawing of the 3D-printed case for the PET bottle reservoir.

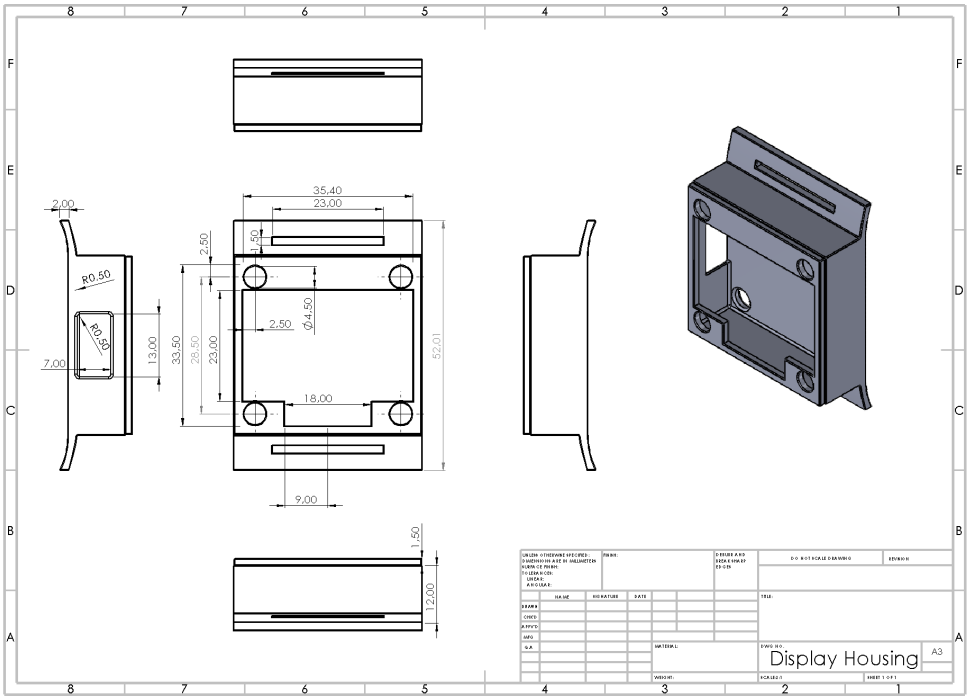


Figure 13: Technical drawing of the enclosure for the OLED display module.